The Environments of High Redshift Active Galactic Nuclei

James Thomas Falder

Submitted to the University of Hertfordshire in partial fulfilment of the requirements of the degree of Doctor of Philosophy.

July 2012

Abstract

In this thesis I study the links between Active Galactic Nuclei (AGN) and their surrounding large scale environments mainly at high redshift. I firstly use *Spitzer* space telescope data for one of the largest and most uniformly selected samples of radio-loud and radio-quiet AGN at high redshift. It consists of 173 AGN of both type-1 Sloan Digital Sky Survey (SDSS) Quasi-Stellar-Objects (QSOs) and type-2 radio-galaxies at the single cosmic epoch of $z \sim 1$. I find significant (8 σ) over-densities of galaxies in the AGNs' environments when compared to an offset field. Further to this I address the question of whether radio-loud AGN are found, on average, in denser environments than their radio-quiet counterparts. I show that there is a link between the environment and radio luminosity of the most powerful radio-loud QSOs and RGs in the sample, and also reconcile the conflicting results in the literature by suggesting that there is only a link to the environment at the highest radio powers.

I extend this work to higher redshift with data from the *Spitzer* extra-galactic Representative Volume Survey (SERVS) and type-1 SDSS QSOs in the regions covered by SERVS. This deep data allowed me to study the environments of QSOs in the redshift range $1 < z < 4$. Again I find significant (4 σ) over-densities of galaxies around the QSOs in this sample, this time making use of the 3.6-4.5 μm colour to select galaxies more likely to reside at the redshifts of interest.

I show that the environments of these QSOs are comparable to those predicted for similarly large black holes in the Durham semi-analytic galaxy formation model (GALFORM).

Finally I use data from the *Herschel*-Astrophysical Terahertz Large Area Survey with the recently launched *Herschel* space observatory to study the environments of type-1 QSOs in the far-infrared (FIR). I find a small excess of galaxies around the QSOs for which I find that the star-formation rate increases with increasing redshift. The star-formation rates are estimated by modelling the FIR spectral energy distribution of the galaxies with a modified black-body spectrum. This follows the general increase in star-formation rate with redshift observed in the Universe as a whole. I also compare these findings with those made by the Submillimeter Common-User Bolometer Array (SCUBA) of higher redshift QSOs.

Supervisors

Jason A. Stevens & Matt J. Jarvis

Centre for Astrophysics Research

University of Hertfordshire

Acknowledgements

In this thesis I use observations made with the Spitzer Space Telescope, which is operated by the Jet Propulsion Laboratory, California Institute of Technology under a contract with NASA. Support for these observations was provided by NASA through an award issued by JPL/Caltech. I also use data from the Herschel space telescope, Herschel is an ESA space observatory with science instruments provided by European-led Principal Investigator consortia and with important participation from NASA. This research has also made use of the NASA/IPAC extragalactic Database (NED) which is operated by the Jet Propulsion Laboratory, California Institute of Technology, under contract with the NASA. I also thank the PIs and members of the SERVS and H-ATLAS teams for allowing me to work on data from these two world leading surveys during my PhD.

I thank the Science and Technology Facilities Council for a research studentship which supported me during this work. I would also like to thank the University of Hertfordshire and especially the Centre for Astrophysics Research for providing me with a suitable environment and facilitates with which to conduct my research, as well as funding my attendance at several conferences and on two observing trips during my PhD.

I would very much like to thank my supervisors Dr. Jason Stevens and Dr. Matt Jarvis whose combined qualities make, I feel, a very useful set of skills to have in a supervisory team.

I am grateful to Matt for his seemingly endless number of new ideas and for letting me work with such good data in the $z \sim 1$ AGN sample. I especially thank Jason firstly for convincing me to do a PhD in the first place and secondly for allowing me to work independently at times whilst at others finding the time for lengthy discussions when required. Throughout he has shared with me his general enthusiasm for Astronomy. Special thanks go to the guys in the office and department who have made my time here very enjoyable and with whom I have made some good friends.

Finally I would like to thank my family for supporting me, especially by, but not exclusively for, providing me with a place to live during my PhD studies. I am also indebted to Sam whose understanding, support and love during the last year has been an enormous benefit and something that I am very grateful for.

Contents

Chapter 1

Introduction

1.1 Active Galactic Nuclei

1.1.1 The History of AGN Observations

The first hint of the phenomenon we now call Active Galactic Nuclei (AGN) was reported in 1908 by Edward A. Fath (Fath, 1909) who observed that the spectrum of NGC 1068 instead of having the usual absorption-line features, that were common to most 'spiral nebulae' (now known to be spiral galaxies), had six bright emission lines. It was not until 1943 that Carl Seyfert (Seyfert, 1943) showed that these broad emission lines, that are found in a small percentage of galaxies, were emanating from a small central and very bright nucleus which appeared almost stellar. The objects in question are now known to be low luminosity AGN and are called Seyferts.

The next important step in the discovery of AGN was the construction of the first generation of radio telescopes in the 1940s and 50s. These led

to the realisation that some of the strongest radio sources in the sky were emanating from outside of the Milky Way, many of these were identified with other galaxies. The first of these was Cygnus A which was linked with a cD galaxy at redshift 0.05 in 1954 by Baade & Minkowski (1954); the term radio galaxy (RG) was used to describe these objects which are now known to also harbour obscured AGN (see Moffet 1966 for a review of the early works on these objects).

In addition to RGs a large population of especially compact radio sources were identified which had no obvious optical companion. In 1959 hundreds of these objects were published as part of the Third Cambridge Catalogue of Radio Sources (3C, Edge et al. 1959). After many attempts to pin down optical counterparts this was finally achieved for 3C 48 in 1960 when Matthews & Sandage (1963) showed that the radio emission appeared to be coming from what looked like a very faint blue star. The term 'radio star' was used for a while but the spectrum was found to be completely inexplicable with many unknown broad emission lines. John Bolton offered the explanation of cosmological redshift as an explanation, implying this was an extragalactic source at great distance, but this idea was not widely accepted, at least not until the optical counterpart of 3C 273 was identified using a novel technique of occultation by the moon (Hazard et al., 1963); its spectrum was also obtained (Bolton et al., 1963) and it had the same strange features as 3C 48. These features were identified by Schmidt (1963) as being the hydrogen emission lines redshifted by a factor of 0.158, following which the spectrum of 3C 48 was found to have an even greater redshift of 0.367 (Greenstein & Matthews 1963; Schmidt 1964).

Together these findings suggested that if the redshift was indeed cosmological and if Hubble's law was valid that these objects were at exceedingly great distances. In fact, 3C 48 was one of the most distant objects yet known and as more radio sources were identified objects were found that had even greater redshifts. This would mean if true that they must be extremely luminous objects, brighter than entire galaxies, but also very compact. This led some astronomers to resist the cosmological interpretation of their redshift for many decades. The term Quasar standing for Quasi-Stellar-Radio-Source was coined and used to describe these extragalactic radio sources which appeared stellar in optical images.

As more of these radio sources were studied in detail it was found that a small number were highly variable on very short time scales (Smith & Hoffeit, 1965), these are known now as Blazars (see Angel & Stockman 1980 for a review). In extreme cases the variation can happen over periods of days which implies the origin of the emission must be a very compact ($\lesssim$ 1 pc) region. It was not known at the time what physical process could produce the enormous energy output observed in such a small, solar-system sized, region.

It was suggested in the 1960s and 70s that the accretion of matter onto a rotating massive black hole would be able to generate the required level of radiation (Hoyle & Fowler 1963; Salpeter 1964; Zel'Dovich & Novikov 1965 Lynden-Bell 1978). However, as black holes were at the time still hypothetical these suggestions remained contentious. If the energy source was indeed gravitational then this would require in some cases compact objects with a billion times the mass of the Sun. There was no observational proof of

such objects and it was hard to imagine how such a large mass could be accreted by a single object. Indeed it was not until the 1980s and 90s when the evidence for the existence of massive black holes really began to become conclusive. This largely resulted from studies that found high central velocity dispersions in nearby galaxies (e.g. Sargent et al. 1978; Dressler & Richstone 1988; Kormendy 1988). It has since become widely accepted that the origin of the nuclear emission observed in the centres of certain galaxies is indeed linked to the presence of super-massive-black holes (SMBHs; e.g. Rees 1984; also see Richstone et al. 1998 for a review of this field).

Further study of the optical counterparts to Quasars led to the realisation that objects existed that appeared identical optically but had no detectable radio emission. It was soon realised that there was indeed a population of non-radio detected AGN; as larger samples of these objects were studied it turned out that in fact radio detected AGN are rare and occur in only about 10 per cent of luminous AGN (Sramek & Weedman, 1980). The term Quasi-Stellar-Object (QSO) was created to encompass both the radio detected and non-detected forms of the stellar looking optical AGN. What process and cause is responsible for some AGN having high radio luminosities was not clear and is still not really understood today. The terms QSO and Quasar are often used interchangeably these days with the distinction and original meaning of the word Quasar slowly being lost to the archives. In fact many of the various naming conventions and classifications associated with AGN are often used differently by different parts of the astronomical community or in older works, which can be, to say the least, confusing. I will use the term QSO almost exclusively to avoid confusion. As with many astronomical

topics as our understanding increases often the names or classification we use become redundant. In this thesis for clarity I have tried to use the terms most applicable for my work and our current understanding of the physics behind AGN, hence I have not always explained the full range classifications that some astronomers use.

1.1.2 Unification

Resolving the structure of AGN is not yet possible, except in part for the nearest of objects, due to their extremely compact size and so the radiation from the nuclei can only be studied as a whole. This leaves many unanswered questions about this collection of highly energetic extragalactic objects, not least being the amazing variety of properties they are observed to have. A potential explanation for at least some of the observational differences has been found in the form of so called unified theories (see Antonucci 1993 for a review). These mostly suggest a view where the SMBH has a thin hot accretion disk surrounded by a torus of colder dusty material which has not yet found its way into the accretion disk.

In these models the accretion disk provides most of the underlying continuum emission of the in AGN through the near-infrared, optical, ultra-violet (UV) and soft X-ray parts of the spectrum (Kembhavi & Narlikar 1999; Osterbrock 1991). The continuum of an AGN in this wavelength range, although complex, is usually fairly well approximated as a power-law, such that $S_\nu \propto \nu^{-\alpha}$, with a spectral index in the region of $\alpha \sim 0.5$. The continuum emission over these wavelengths is in most cases produced largely due to

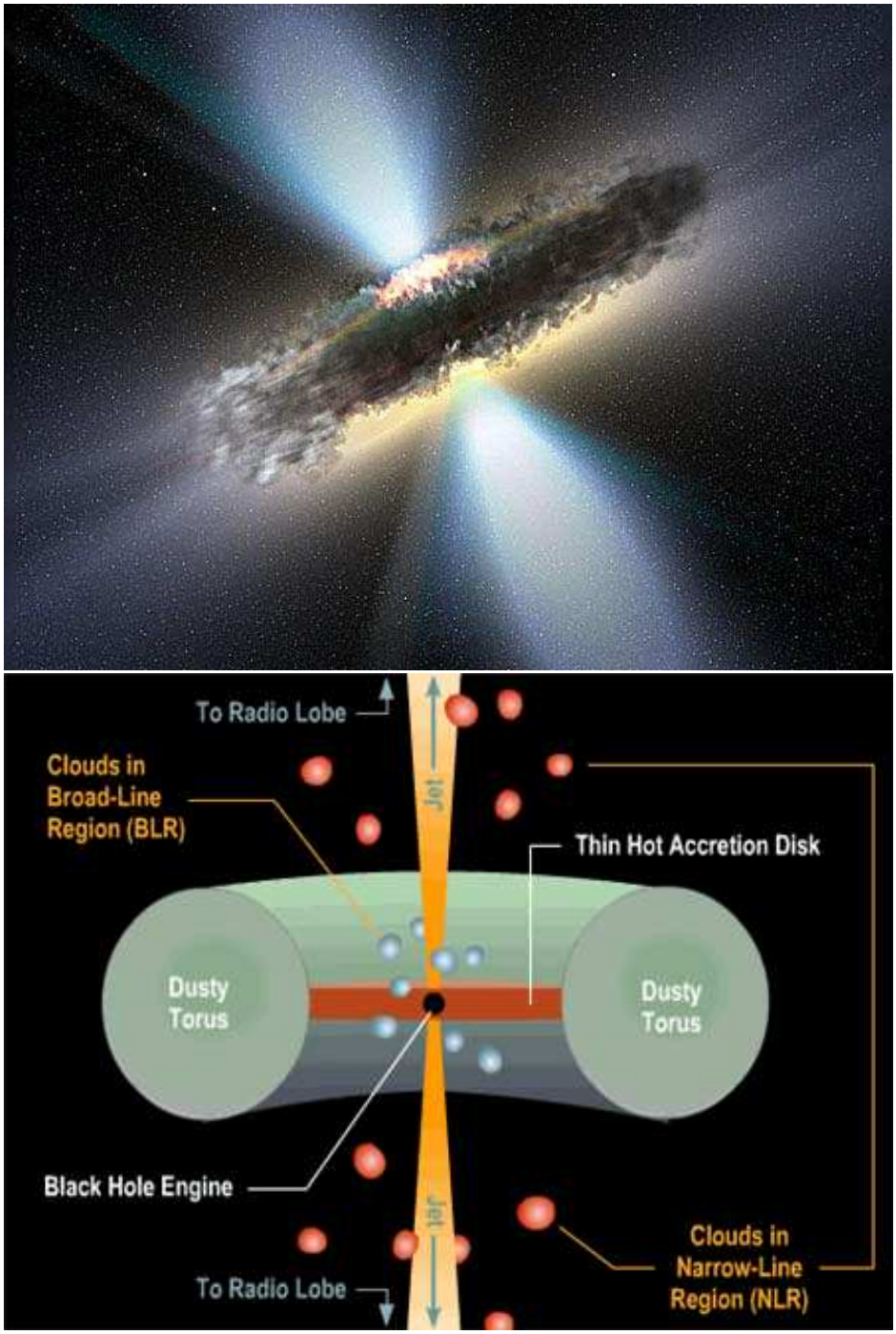

Figure 1.1: The top panel shows an artists impression of an AGN (Image credit: ESA/NASA, the AVO project and Paolo Padovani). The bottom panel is a schematic showing the main features of an AGN as outlined in the unified theories (Image credit: Brooks/Cole Thomson Learning).

thermal emission but may have some contribution from other processes such as inverse Compton scattering boosting lower energy photons. The exception to this is Blazars which can be entirely dominated by synchrotron emission.

The material in the torus acts by obscuring this continuum for certain lines-of-sights, see Fig. 1.1. This absorbed radiation is reprocessed and emitted in the mid and far-infrared part of the spectrum, producing the mid-infrared excess that appears to be a common feature to all AGN. Cases in which our line-of-sight sees the accretion disk are described as type-1 AGN, this explains QSOs and Seyfert-1s, whereas those where the line of sight is obscured by the torus are known as type-2 AGN, this explains RGs and Seyferts-2s. The different spectra of a type-1 and type-2 AGN are shown in Fig. 1.2 which shows the absorption of light in the optical and UV part of the spectrum in the type-2 spectra.

There is of course a luminosity effect as well and this explains the difference between Seyferts and the more luminous AGN we observe at higher redshift. As with most things in astronomy, luminous AGN are rare and so at low z the volume surveyed is not sufficient to observe large numbers of the brightest AGN. In contrast, at high z, the flux limits of current surveys means only the brighter AGN such as QSOs and RGs can be detected. In the unified schemes the difference in luminosity is naturally explained by Seyferts having intrinsically lower mass black holes.

Unification also offers an explanation for the different types of emission lines seen in the spectra of AGN. Highly ionised narrow emission lines are seen in the spectra of all AGN, however, in addition type-1 AGN (QSOs and Seyfert-Is) are also observed to have broadened emission lines. This

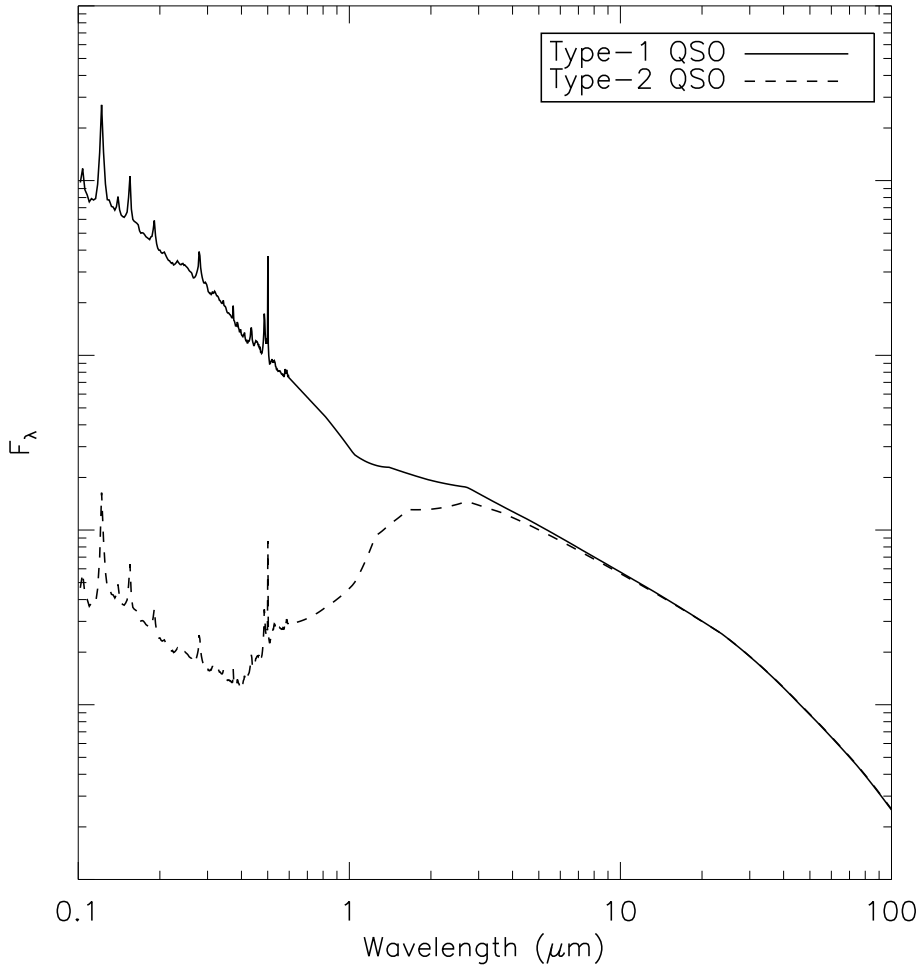

Figure 1.2: Comparison between the SEDs of type-1 and type-2 QSOs from the SWIRE Template Library, see Polletta et al. (2007) for full details. The type-1 SED is derived by combining the SDSS quasar composite spectrum and rest-frame infrared data of a sample of 35 SDSS/SWIRE SEDs. The type-2 SED corresponds to the model used to fit the SED of a heavily obscured type-2 QSO, $SWIREJ104409.95 + 585224.8$. The fluxes are normalised at 24 μm and the flux scale is arbitrary.

is explained by assuming that the emission lines come from clouds of dust and gas orbiting the black hole at various radii and ionised by the continuum from the accretion disk. The clouds closest to the black hole will have orbital velocities higher than those further away and this causes them to be Doppler broadened by a larger degree. The broad-line region (BLR) is closer to the black-hole and hence, in most type-2 AGN is, like the accretion disk, obscured by the torus. In some intermediate orientations the line-of-sight allows for some of the broad line region to be observed whilst still obscuring the accretion disk, this explains why some RGs are also observed to have broad lines. Clouds orbiting further away have lower velocities and hence do not experience the same degree of broadening, this region is known as the narrow-line region (NLR). The NLR will also be less likely to be obscured by the torus; hence why the observation of narrow lines is not observed to be orientation dependant.

The ratios of emission lines can be used to estimate the temperature of the gas in the NLR and this is likely to be in the region of $\sim$ 15000 K (Osterbrock, 1991). Making assumptions about the geometry, composition and density it can be shown using the luminosity of the Hβ line that NLRs are probably of the order of 100 pc ($\sim$ 328 light years) from the central SMBH whilst BLRs are likely at a radius closer than $\sim$ 0.07 pc (0.2 light years). The NLRs have been resolved in a handful of the closest Seyfert galaxies and appear to agree with these predictions; as for BLRs these have not been resolved in any source (Osterbrock, 1991).

Together these ideas can, broadly speaking, explain the observed properties of most AGN from the soft X-ray to the infrared parts of the spectrum.

1.1.3 Black Hole Masses and Accretion Rates

As the power source of AGN is now accepted as being gravitational (Rees, 1984), it makes sense therefore that the energy output should, in part at least, be governed by the mass of the black hole at its centre. Hence the lower luminosity types of AGN such as Seyferts are most likely different from QSOs and RGs because they harbour lower mass SMBHs. An idea for the mass required to provide the incredible luminosities that AGN are observed to have can be obtained using the Eddington limit. This is the maximum luminosity that can be produced by an object of a certain mass before the radiation pressure will be too great for gravity to prevent the object being blown apart. This luminosity is called the Eddington Luminosity and is given by

$$\mathrm{L_{edd}} = 4\pi \mathrm{cGm_H M}/\sigma_\mathrm{T} = 1.3 \times 10^{38} (\mathrm{M}/\,\mathrm{M_\odot})\ \mathrm{erg/s} \tag{1.1}$$

where σ_T is the Thomson electron scattering cross section and m_H the mass of hydrogen. Making the assumption of spherical geometry and a mainly hydrogen composition for the accreating material it is possible to show that for a typical QSO bolometric luminosity of 10^{46} erg/s the minimum mass it can have is $\sim 10^8\,\mathrm{M_\odot}$ (Osterbrock, 1991); this is known as the Eddington mass. In a Seyfert where typical bolometric luminosities are of the order 10^{44} erg/s this gives a mass of $\sim 10^6\,\mathrm{M_\odot}$. Efficiency arguments suggest that a spherical accretion model is unlikely in high luminosity AGN as in that case far less energy is likely to be radiated making it difficult to generate the required luminosity, a disk model is therefore favoured (Rees, 1984). A disk model for the accretion will permit a lower Eddington mass, as some

radiation escapes at the poles, but it has been shown this is a reasonable order of magnitude estimate none the less (Kembhavi & Narlikar, 1999).

Another physical parameter it might be interesting to estimate is the accretion rate, i.e. the rate at which the black hole acquires mass. This can be estimated by considering the maximum energy released by a mass ($E \sim mc^2$) some of which will be lost into the black hole. The luminosity produced by an accreting black hole can then be given by $L = \eta \Delta M c^2$ where ΔM is the accretion rate and η is the amount of the available mass that is radiated by the accretion disk. General relativity gives efficiencies of between 6 and 40 per cent depending on the spin state of the black hole with higher efficiencies for the higher spin rates (Rees, 1984). Assuming an efficiency of $\eta = 0.1$ this gives accretion rates of $\Delta M \sim 0.02\,M_{\odot} yr^{-1}$ and $\Delta M \sim 2\,M_{\odot} yr^{-1}$ for typical Seyfert and QSO luminosities respectively.

Once the existence of SMBHs became widely accepted, attempts were made to determine the mass of these invisible objects observationally and to see if they really did have the masses that their luminosities suggested. In nearby AGN this is possible by using reverberation mapping which looks for the time lag between variations in an AGNs continuum luminosity and the strength of the Hβ emission line (see reviews by Peterson 1993 and Netzer & Peterson 1997). This work is based on making the assumption that the Hβ emission comes from clouds orbiting the black hole in the BLR and are ionised by the accretion disk. It is then possible to calculate the distance from the source of ionising radiation that the Hβ emitting clouds are found. Knowing the radius at which the clouds are at and assuming that the broadening of the Hβ line is due to the velocity with which the emitting clouds are orbiting

the black hole allows for the mass to be calculated using the laws of Keplerian motion. Thus the black hole mass is given by

$$M_{bh} = \frac{R_{BLR} V_{BLR}^2}{G} \tag{1.2}$$

where V_{BLR} is obtained by assuming it is proportional to the FWHM of the Hβ emission line such that $V_{BLR} = f \times FWHM_{H\beta}$ and f is a factor which takes into account the geometry of the emitting region.

Reverberation mapping is unfortunately an observationally time consuming process and requires years of monitoring for each source. It is however, fortuitous that from the current data collected in this way a relation has been observed between the the AGN continuum luminosity at 510 nm and the radius of the BLR (Kaspi et al., 2000). It is therefore possible using this relation to obtain the black hole mass using a spectrum which contains the Hβ emission line.

This method is fine for low redshift AGN, where the Hβ line can be observed using optical spectrographs. At redshifts greater than $z \sim 0.8$ however, the Hβ line is shifted to the infrared, making observations less straightforward. However, a new method for making virial black hole mass measurements at high redshift was presented by McLure & Jarvis (2002). This method uses the continuum luminosity at 310 nm and the FWHM of the MgII emission line, which is found in the rest frame UV therefore remaining accessible to optical spectrographs until $z \sim 2.5$. This method has been calibrated against the reverberation mapping data and was also compared to measurements of the black hole mass made using the Hβ line, both of which

suggest this is a useful tracer of black hole mass at higher redshift.

Several authors have used these techniques to study how an AGN's black hole mass is linked to properties of the host galaxy and radio luminosity of the AGN (e.g. Laor 2001; McLure & Dunlop 2001a; McLure & Dunlop 2002; Dunlop et al. 2003; McLure & Jarvis 2004). Some of the main conclusions are that radio luminous AGN are found to have black holes that are on average 45 per cent more massive than AGN which are not radio luminous (McLure & Jarvis, 2004). At low redshift where the host galaxy can be studied with high resolution data, such as that from the *Hubble* Space Telescope, it has been found that there is a correlation between the host galaxies' bulge luminosity and black hole mass. This correlation follows the same relationship observed in inactive galaxies and is indicative of a relationship between the bulge mass and black hole mass of the form $M_{BH} \approx 0.0012\ M_{Bulge}$ (McLure & Dunlop, 2002).

1.1.4 Radio Properties

The orientation based unification models while explaining many of the observed features, do not help to explain differences in the properties of AGN in the radio regime. Radio-detected and non-detected AGN are hence unified separately as distinct populations. The radio emission from AGN is attributed to the accreting SMBH having relativistic jets of accelerated particles. These jets are emitted at right angles to the plane of the accretion disk, and are similar albeit on much larger scales and energies to those seen in young-stellar-objects or X-ray binaries. The jets emit synchrotron radiation

as charged particles spiral outwards, accelerated by the SMBH's magnetic field.

In some cases the radio luminosity is dominated by emission from the core these are classified as Fanaroff-Riley class-I (FRIs, Fanaroff & Riley 1974). In others jets are dominated by emission in lobes at great distance from the cores (FRIIs). The underlying difference is though to lie in the jet power and the jets in FRIIs remaining relativistic beyond the host galaxy and in doing so smashing into the inter-galactic-medium (IGM) producing bright radio-lobes which are more luminous than the core emission.

In general, powerful radio-loud AGN have FRII morphology and are observed to have a spectrum with $S_\nu \propto \nu^{-\alpha}$ with a spectral index in the region of $\alpha \sim 0.7$. Synchrotron radiation if optically thin produces this observed power-law spectrum and at radio wavelengths it becomes the dominant source of emission from radio-loud active galaxies. The more compact FRIs on the other hand often have a flat radio spectrum which is expected from optically thick synchrotron radiation due to the higher densities closer to the base of the jet (Kembhavi & Narlikar 1999; Osterbrock 1991).

The highly variable radio-loud AGN (Blazars) are explained as being a special case where we are observing them looking directly down or close to the jet axis (Kembhavi & Narlikar 1999; Osterbrock 1991). This explains their high variability and high observed luminosity due to the relativistic effect of beaming from Doppler boosting (Blandford & Rees, 1978). These objects spectra are in some cases entirely dominated by synchrotron emission from the jets at all wavelengths.

In order to classify the non-detection of radio emission from most AGN

the terms radio-loud and radio-quiet were invented. The choice of terms was partly made because the sensitivity of radio telescopes places the lower limit on how much radio emission could be detected and so those not detected could potentially lie just below the limit of current surveys. Such extreme objects would be unlikely to be entirely radio-silent, and indeed as radio telescopes have become more sensitive, radio-quiet AGN have begun to be detected (for example Kukula et al. 1998). With the next generation of more sensitive radio telescopes like the Square Kilometre Array (SKA) and the LOw Frequency ARray (LOFAR) many more radio-quiet AGN should have their radio emission detected.

The definition of radio-loudness can thus take two forms. One is to define a radio luminosity at which an AGN is considered radio-loud. This has a major drawback in that it takes no account of the size of the black hole powering the AGN hence using this measure comparisons may be biased for the following reason. It is observed that of those with black hole mass estimates virtually all radio-loud QSOs (RLQs) have black hole masses greater than 10^8 $M_\odot$ (McLure & Jarvis, 2004). In contrast radio-quiet QSOs (RQQs), whilst observed with black holes masses that can be equally as large as RLQs, can have masses at least as low as 10^7 $M_\odot$ (McLure & Jarvis, 2004). Indeed at any given black hole mass the range of radio luminosities spans several orders of magnitude.

To address this possible source of degeneracy between radio-luminosity and black hole mass a radio-loudness parameter was invented which involves taking the ratio of optical flux to radio flux received from an object. One such measure is defined by Ivezić et al. (2002) in which QSOs with $R_\mathrm{i} > 1$

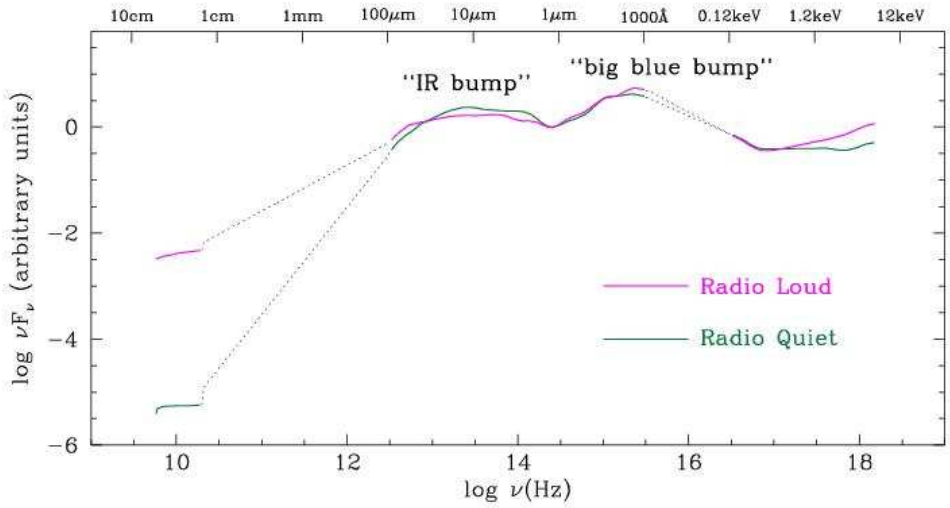

Figure 1.3: SEDs of a typical radio-loud and radio-quiet QSO, showing the several orders of magnitude difference between the level of radio emission despite almost identical SEDs at other wavelengths (Image credit: Elvis 1994).

are considered radio-loud where

$$R_{\rm i} = \log(F_{\rm radio}/F_{\rm i}) \tag{1.3}$$

$F_{\rm radio}$ and $F_{\rm i}$ are flux densities measured at 1.4 GHz and in the i-band respectively.

It is still not clear exactly what causes the radio emission we see in radio-loud AGN, and why we do not see similar emission in otherwise comparable radio-quiet AGN (see Fig. 1.3). As discussed radio-loud AGN are known to be confined to those with the highest mass black holes (McLure & Jarvis, 2004), however radio-quiet AGN are observed to have equally massive black holes and some of these have radio emission consistent with inactive galaxies (McLure & Dunlop, 2002). It appears therefore that one requirement for an

AGN to be radio-loud is an especially massive black hole, however, there is clearly not simply a black hole mass where AGN become radio-loud. Other potential causes of radio-loudness are the large scale environment, which will be discussed later in Section 1.2.3, or the spin of the black hole which might be higher in radio-loud AGN (e.g. Wilson & Colbert 1995, Moderski et al. 1998, Volonteri et al. 2007 and Sikora et al. 2007).

It is also still not fully understood whether there is a true AGN radio power dichotomy (e.g. Ivezić et al. 2002; Lacy et al. 2001; and more recently White et al. 2007; Zamfir et al. 2008), *i.e.* the radio luminosity of AGN is not a spectrum, rather two distinct populations, loud and quiet. This also raises the question of whether radio-loud and quiet AGN are intrinsically different or whether we just happen to be observing some whilst they are going through a period of radio-loudness. If the analogues between AGN and X-ray binaries (e.g. Markowitz & Uttley 2005) are physically accurate then this would favour AGN having cycles of radio-loud and quiet phases but as the timescales would be orders of magnitude longer we cannot observe this process directly.

The discovery of radio-quiet AGN and the proposed unified theories leads to the suggestion that there should also be a large population of radio-quiet forms of RGs, which we are missing due to not being able to select them in broad-band optical filters or using radio data. These objects have started to be discovered in recent years by looking for a mid-infrared excess from the warm torus using telescopes such as the *Spitzer* Space Telescope, or by looking for the narrow emission lines known to be associated with RGs. These objects are usually referred to as type-2 QSOs (Zakamska, 2005).

1.1.5 High Energy Properties

AGN are observed to radiate significantly across virtually all of the electromagnetic spectrum. It was clear early on therefore that multiwavelength observations would be important to fully understand them. It was with great anticipation then that the first X-ray satellites in the 1970s made the first high energy observations of these extreme objects. If indeed they were powered by the accretion of material onto a SMBH then they should be luminous at X-ray wavelengths. Indeed AGN were found to be some of the most luminous X-ray emitting sources in the sky and X-ray emission was found to be a common feature in almost all AGN (Elvis et al., 1978). They were also found to be highly variable at these wavelengths (Turner & Pounds, 1988) which meant the source of the emission must lie close to the central black hole. As larger samples of X-ray spectra were obtained the emission was found to be well approximated with a power law, such that the number of photons of energy E is $N_E \propto E^{-\Gamma}$ where Γ is the photon index which was found to be in the range $\sim$ 1.9-2.0 (Nandra & Pounds, 1994).

The thermal like emission process that can explain the optical, UV and softest X-rays cannot produce the higher energy X-rays observed and so a different mechanism is required. The emission process is most likely inverse Compton scattering of lower energy photons from the accretion disk by relativistic electrons either at the base of a jet in radio-loud AGN or in a magnetic corona above the accretion disk (Balbus & Hawley 1991; Mattson 2008). Other prominent X-ray features are emission lines caused by the fluorescence of Iron by X-ray continuum photons, predominately the Fe Kα line

Table 1.1: Table showing a very simplified picture of how some of the many different names attributed to AGN fit together. Showing distinctions in mass of their black hole, radio luminosity and orientation.

	Low mass	High mass	
	Radio-quiet		Radio-loud
Un-obscured (Type-1)	Seyfert-1	Radio-quiet QSO	Radio-loud QSO or Blazar
Obscured (Type-2)	Seyfert-2	Type-2 QSO	RG

at 6.4 keV. Lower energy X-ray photons can also be absorbed by the torus or other material in the same way that UV and optical photons are and so type-2 AGN can be identified by looking for absorption in the X-ray spectrum. X-ray selection is potentially one of the most uniform ways to select AGN as it can be used to select both type-1, type2, radio-loud and radio-quiet AGN; although there may be some bias associated with radio-loud AGN where relativistic jets will increase the inverse Compton scattering.

1.1.6 Summary

To summarise, observationally AGN are very luminous non-stellar objects that are seen in the centre of certain galaxies. Observationally they are also labelled with many different names and categories depending on their properties (see table 1.1), but it is accepted that the basic picture in all cases is a rotating SMBH surrounded by a hot thin accretion disk of in-falling material. This is then surrounded by a dusty torus which creates orientation dependent obscuration of the near-infrared to soft X-ray continuum from the accretion disk and broad line emission from the broad-line-region. The mass

of the black hole determines the absolute luminosity that the accretion disk can produce. However, the accretion rate is also important and found to vary significantly, but in general smaller black holes will generate the lower luminosity categories of AGN such as Seyferts, whereas larger black holes will produce higher luminosity AGN such as QSOs or Radio Galaxies. At high-z, observing low luminosity AGN is not yet technically possible and so studies of high-z AGN focus on QSOs and Radio Galaxies. Conversely the local universe does not contain the volume required to find large numbers of high luminosity AGN, as these are rare, and so to study these objects we must go to high-z.

1.2 AGN and Galaxy Formation

Evidence is mounting that AGN activity in galaxies is playing an important role in their formation and subsequent evolution. It is now thought that most if not all massive galaxies contain at their centres a SMBH (Magorrian et al., 1998); so why is it that not all galaxies are observed to be active? Is it simply because an AGN is a short lived phenomenon which is quickly over and so we only observe a small portion of galaxies in this phase at any time? Alternatively, is there something different going on in some galaxies which is triggering this activity?

In the local universe it is known that the mass of a galaxy's SMBH is tightly related to both the stellar mass and the mass of galaxy itself (Gebhardt et al. 2000; Ferrarese & Merritt 2000). Therefore as we see equally massive galaxies as being both active and non-active the activity cannot be

due solely to the black hole mass. It follows then that the accretion rate must be higher in active galaxies than non-active ones. The tight correlation between the black hole's mass, which is an object confined to a region << pc in size, and the mass of the galaxy which can cover several hundred kpc, is to say the least perplexing. How can these two objects know about the mass of each other despite having such vastly different scales? One potential suggestion is that the stellar and black hole mass are built up by the same process, this is a sensible connection as both star formation and black hole accretion would require a supply of relatively cold gas. This suggests that the formation of galaxies and their SMBHs must be intimately linked.

1.2.1 Host Galaxy Studies

It had been thought based on early samples that powerful radio-loud AGN were hosted by spheroid type galaxies (ellipticals) and radio-quiet AGN were found in disk type galaxies (spirals; e.g. Yee & Green 1984) and this of course provided an obvious suggestion for the reason for their difference. However, as sample sizes have increased they have became more evenly selected and the biases between radio and optical selection have become better understood it now appears that this may not actually be the case. The confusion on this issue had been somewhat affected by the difficulty in studying the host galaxies of luminous QSOs which out-shine their hosts by several magnitudes in some cases.

Several studies using the high-resolution of the *Hubble* Space Telescope have been able to separate the emission from each component and allowed

the study of the host galaxies as a result, albeit at relatively low redshift ($z \lesssim 0.5$; e.g. Hooper et al. 1997; Bahcall et al. 1997; Boyce et al. 1998; Schade et al. 2000; McLure et al. 1999; Dunlop et al. 2003). The host galaxy studies of McLure et al. (1999) and Dunlop et al. (2003) go as far as to show that QSOs brighter than $M_v = -23.5$ (i.e. not Seyferts) are virtually all hosted by spheroidal galaxies. This means that the difference between disk and spheroid hosts is likely related to the mass of the central black hole and not linked directly to the radio power. The apparent link was down to powerful radio-loud AGN being hosted exclusively by the most massive AGN whereas radio-quiet AGN span a much wider range in black hole mass and hence host type. If samples of radio-loud and radio-quiet AGN are selected at random the likelihood is the radio-loud AGN will contain more massive black holes and thus be hosted exclusively in spheroids whereas the sample of RQQs will be dominated by the more common lower mass QSOs hosted in spirals.

The relationship between QSOs' optical luminosities and their host galaxy luminosity has also been studied by these works. It might be expected that due to the *Magorrian* relation the bulge and black hole masses would be closely linked at least at these low redshifts. However, while this might be the case the QSO luminosity as discussed depends also on the accretion rate which has been found to vary significantly. As such although earlier works found some evidence for a correlation between the optical luminosity and the galaxies' brightness the larger and more robust studies of McLure et al. (1999), Dunlop et al. (2003) and Letawe et al. (2010) find at best only a weak relationship.

1.2.2 Feedback

In recent years the potential importance of AGN activity for the formation of galaxies and their link to star-formation has been realised from a theoretical point-of-view. This view largely came about due to the difficulty in reproducing the observed luminosity density of galaxies with semi-analytic and numerical models (Bower et al. 2006; Croton et al. 2006). It seems that these require some kind of feedback from AGN in order to halt the production of stars at the bright end of the luminosity function. This feedback has been split into two types by the modellers for their purpose, labelled for the time being somewhat confusingly Radio and Quasar mode feedback (Croton et al., 2006). Quasar mode is considered to have the form of a wind created by the luminous accretion disk, which could be responsible for removing gas from its host galaxy. This goes some distance to explaining the observed correlation between SMBH mass and the stellar mass as blowing out the gas would regulate star-formation.

Radio mode on the other hand is modelled as the feedback that would be created by powerful kpc-scale radio jets which punch their way out of the host galaxy and into the surrounding IGM. This gives them the ability to affect the surrounding environment while having little influence on the galaxy itself as the volume they have to work on inside the galaxy is minimal. Obviously in reality all powerful AGN are likely to have the Quasar mode type of feedback, whereas perhaps only the powerful radio-loud AGN would be capable of radio mode feedback. The exact effect that radio jets have on the larger scale environment is still unclear but there are suggestions of both

a truncation (Rawlings & Jarvis, 2004) or a triggering (Wiita 2004; Elbaz et al. 2009) of star formation in the proto-cluster environment.

1.2.3 Links between AGN and their Environments

There are many reasons for studying and understanding the large scale environments in which we find Active Galactic Nuclei (AGN). As discussed in Section 1.2.2 it is now thought AGN activity is important for both the evolution of their host galaxy and potentially their surrounding environments. It is important therefore, to study the environment to understand the effect that these feedback processes may be having on large scales.

In addition what triggers AGN activity in the first place is still poorly understood. Is it purely part of an evolutionary sequence that all galaxies undergo, or is it something that only happens to certain galaxies and if so, why? If all galaxies contain SMBHs (Magorrian et al., 1998) did these all grow through AGN activity? A plausible suggestion for the trigger of AGN is mergers as these could supply/disturb a large reservoir of gas which finds its way to the central SMBH/s . This mechanism has been suggested as the cause of the intense bursts of star formation observed in ULIRGS (Sanders & Mirabel, 1996) and indeed many authors have linked the two phenomena both with mergers (e.g. Clements & Baker 1996; Ishida 2004; Kartaltepe et al. 2010) and also with QSOs (e.g. Sanders et al. 1988; Dasyra et al. 2006; Hopkins et al. 2006; Page et al. 2001; Page et al. 2004; Stevens et al. 2005; Kawakatu et al. 2006). The generally suggested idea is that a merger supplies cold gas to the nucleus of the galaxy triggering both an intense burst

of star formation and growth of the black hole, after which winds from either process clears the dust and reveals the active galactic nucleus. If mergers are important for some or all aspects of AGN activity then the large scale environment clearly will be too. Mergers are likely to be more common in dense but not yet virialised environments, as velocities dispersions are lower than in fully formed clusters (Ostriker 1980, but see Mihos 2004 for a slightly different view), so finding out if AGN are preferentially found in dense environments and if so how dense are key pieces of the puzzle.

It is also possible that the large scale environment is responsible for some of the properties AGN are observed to have. An example is the radio-loudness of AGN which could be affected by the environment through processes such as jet confinement, whereby radio jets could appear more luminous where the inter-galactic-medium (IGM) is denser, (e.g. Barthel & Arnaud 1996).

Environmental Studies

Many of the first statistical studies of the environments in which AGN are located were conducted in the late 1970s and 80s as samples of AGN started to become significant in numbers. These studies were largely a result of the realisation by the astronomical community that QSOs really were at the incredibly large distances that their redshifts suggested, which meant that they were indeed extremely luminous objects. At this time there was no accepted idea for what could be powering such a release of energy in what appeared to be a very compact region. It therefore made sense to try to figure out what was causing this activity and so several authors looked for relationships between activity and the environment in which galaxies were found. Some

of the main results of these studies were that more luminous AGN (QSOs and RGs) occupied environments on average denser than field galaxies (e.g. Roberts et al. 1977; Longair & Seldner 1979). Whereas Seyfert galaxies were generally found in environments typical of field galaxies (e.g. Gisler 1978; De Robertis et al. 1998. However, statistically most types of AGN also seemed to avoid the richest cluster environments and instead favoured low density clusters or groups; these included QSOs, Seyferts and luminous RGs.

Several authors argued, that the local environment was of much more importance in triggering activity in galaxies than membership of a group or cluster; this was linked to mergers as many local radio-galaxies showed signs of a recent merger (see Schweizer 1980 for Fornax A (NGC 1316) and Tubbs 1980 for Cen A). A galaxy is evidently more likely to experience a merger if it has more local companion galaxies and many studies found an enhanced probability for there to be a radio source in interacting systems (e.g. Dressel 1981; Hummel 1980; Adams et al. 1980; see Balick & Heckman 1982 for a review of these early works). If indeed mergers are responsible for triggering AGN then it makes sense that these would occur less in virialised cluster environments where the interaction rate of galaxies would be lower than in un-virialised groups. This may explain the apparent absence of powerful AGN in the richest of environments. Whether the merger hypothesis can extend down to explain the activity in Seyfert galaxies is unclear as most show no signs of recent major mergers but minor mergers with satellite galaxies may be a possibility (De Robertis et al., 1998).

As samples of AGN increased in numbers it was possible to make more statistically sound studies and to start looking for any differences between the

environments in which different types of AGN were found. An interesting question to ask is whether there is any difference in the environments of AGN which are radio-loud and those which are radio-quiet. This was first looked at for QSOs by Yee & Green (1984), in which a marginally larger over-density was detected around the RLQs in their sample of objects at $0.05 < z < 0.55$. However, a later improved study with more data and refined techniques removed the significance of this result (Yee & Green 1987). More work on the sample was conducted by Ellingson et al. (1991) who added more faint RQQs. As a result they reported a significant difference in the environments preferred by RLQs and RQQs, with RQQs in general preferring poorer environments at the 99 per cent confidence level. This was also found by Smith & Heckman (1990) at $z > 0.3$ who found powerful RGs and RLQs had roughly twice the number of companion galaxies than RQQs. As well as by Hutchings et al. (1999) who found that RLQs occupied more dense environments in the near-infrared than RQQs with $0.9 < z < 4.2$.

In contrast, Fisher et al. (1996) and more recently both Wold et al. (2001) and McLure & Dunlop (2001b) found the environments of RLQs and RQQs to be indistinguishable at $z \sim 0.2$ and at $0.5 < z < 0.8$ respectively. However, Kauffmann et al. (2008) found more evidence for a difference in that radio-loud AGN were found to reside in environments a factor of $2-3$ more dense than radio-quiet AGN in a large matched sample of SDSS emission-line AGN in the local universe. These results clearly present us with a very mixed picture but understanding the conflicting results is not that difficult because AGN samples are notorious for their selection effects.

Comparing samples of AGN at different epochs in flux limited data leads

to the inherent sampling of more luminous objects, hence a different population, at higher redshift. In addition, comparing radio-loud AGN selected in radio surveys to radio-quiet AGN identified optically may lead to significant biases in the intrinsic luminosity of the samples. It is probable therefore that many of the conflicting results suffer in some way significant selection effects or are simply sampling AGN of different intrinsic luminosities. If anything, what the mixed results are telling us is that the link between AGN and their environments is not straight-forward, is likely to be just one of several factors affecting the observed properties of AGN and may vary for AGN of different types or of different intrinsic luminosities.

FIR Environments

In the Far-Infrared (FIR) which detects the dust reprocessed UV light associated with on-going star formation, the environments of AGN are less well studied. This is primarily down to a lack of suitable data due to the increased difficulty of observing at these wavelengths. The major issue is simply that the area of sky surveyed in the FIR has until recently been incredibly small, for example the Submillimeter Common User Bolometer (SCUBA) (Holland et al., 1999) on the James Clark Maxwell Telescope surveyed just 0.6 sq degrees to the confusion limit during its nine year lifespan. This means that it is lucky if even a handful of luminous AGN exist in the area surveyed just by chance.

This of course did not preclude the targeted study of such objects and indeed many authors made observations of the fields of luminous high-z AGN to look for proto-clusters in formation (Ivison et al. 2000; Stevens et al. 2003;

Smail et al. 2003; De Breuck et al. 2004; Greve et al. 2007; Priddey et al. 2008 and Stevens et al. 2010). All of these studies found that known high-z AGN could be used to target regions that were likely to contain significant numbers of the recently discovered extremely luminous Submillimeter galaxies (SMGs; Blain et al. 2002). While most of these works targeted extreme objects in terms of their redshifts and/or luminosities, Stevens et al. (2010) targeted typical QSOs near the break in the X-ray luminosity function at lower redshift ($1.7 < z < 2.8$). In line with studies of the more extreme objects an excess of SMGs was found in the QSO environment projected to be within $\sim$ 400 kpc. However, the SMGs found in Stevens et al. (2010) appear to have a lower 850 μm flux, hence Star Formation Rate (SFR), than the SMGs found around higher z AGN, possibly showing that SFRs in AGN environments have started to decline even by $z \sim 2$. All these studies however suffer from inherently small sample numbers (at most seven objects and eighteen in total) as well as various selection effects.

With the launch of the *Herschel* Space Telescope (Pilbratt et al., 2010) and commissioning of SCUBA2 (Holland et al., 2006) on the *James Clark Maxwell* Telescope this situation has changed. Surveys such as *Herschel* Astrophysical Terahertz Large Area Survey (H-ATLAS; Eales et al. 2010), which will cover 550 sq. degrees down to a 5-sigma depth of $\sim$ 33.5 mJy/beam at 250 μm, will allow large samples of AGN to be studied and many of the findings from instruments such as SCUBA to be tested on larger samples and extended to lower redshift.

1.2.4 Signposts

Finding large scale structure at high-redshift is a non-trivial activity as high density peaks in the universe are rare and looking back gigayears in cosmic time means that foreground fluctuations will easily wash out any obvious over-densities of distant galaxies. Traditional cluster finding methods require large area deep surveys; for example Papovich et al. (2010) required all of *Spitzer*'s SWIRE survey (49 sq degrees) to locate the current highest spectroscopically confirmed cluster at $z = 1.62$. However, AGN on the other hand are extremely luminous and therefore detectable out to $z > 6$ with shallow wide area optical surveys or by their radio emission in large area radio surveys. Many authors have therefore used these signposts for high-density regions in the high-z universe for follow-up and have located high-redshift clusters and proto-clusters in observationally efficient ways (e.g., Kurk et al. 2000; Pentericci et al. 2000; Ivison et al. 2000; Stevens et al. 2003; Stern et al. 2003; Venemans et al. 2007; Kim et al. 2009; Doherty et al. 2010; Galametz et al. 2010). Additionally many of the highest redshift objects found have until recently been QSOs (e.g. Fan et al. 2003). In this way AGN can be used to locate the regions of interest for the study of the formation of galaxies and large scale structure in the early Universe.

1.3 The Sloan Digital Sky Survey

One survey which has revolutionised the study of AGN and especially QSOs is the Sloan Digital Sky Survey (SDSS; Adelman-McCarthy et al. 2006). SDSS has currently imaged over a quarter of the sky in five bands (8400

sq. degrees) and taken over 1.5 million spectra using its dedicated 2.5 m telescope at the Apache Point Observatory, New Mexico. In the process it has identified $\sim$ 120000 broad-line QSOs up to the highest redshifts yet explored (*i.e.* $z = 6.4$, Fan et al. 2003). The SDSS Quasar Survey (Schneider et al., 2005) used optical colour selection, in their u, g, r, i, and z bands to identify potential QSOs for follow up spectroscopy, giving the largest and most reliable sample of QSOs reaching to high-z to date.

One feature that is very useful is the ability to identify both radio-loud and radio-quiet QSOs in identical ways; avoiding the selection biases of radio selection. The SDSS combined with the evidence that AGN can be used as signposts for structure at high redshift makes for a powerful tool in the study of galaxy evolution at these epochs. SDSS QSOs form the basis for most of the AGN samples used in this thesis and without it our knowledge of high redshift AGN would be dramatically different.

1.4 Infrared Astronomy

In the last three decades the ability to place observatories in space has allowed observations to be made at wavelengths that are inaccessible to ground based facilities; this advance has revolutionised astronomy. An area of the spectrum little explored before the age of the space telescope is the infrared which is largely absorbed by water molecules in the Earth's atmosphere. In this thesis I make use of data from two of the most recent infrared space telescopes.

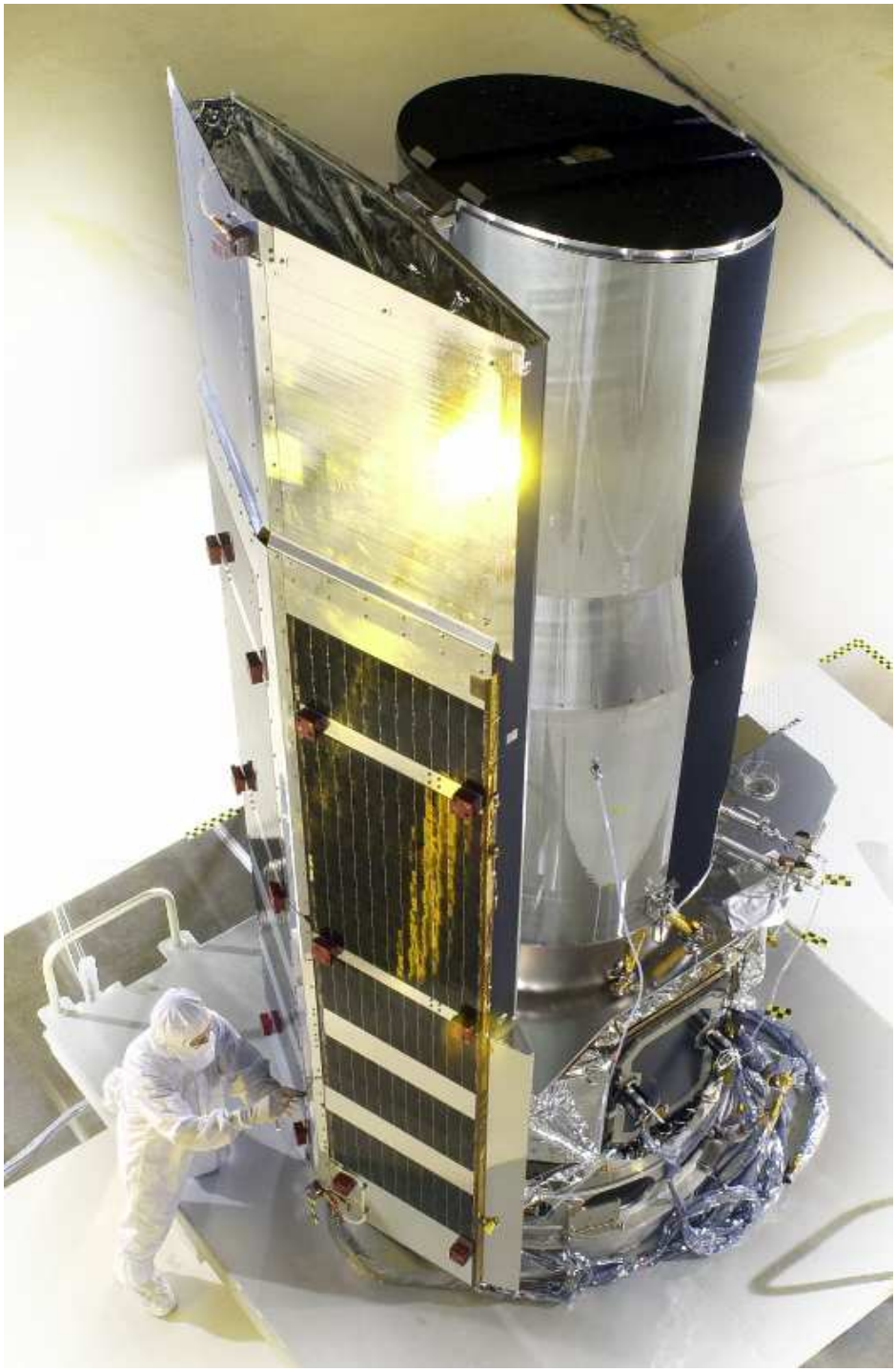

Figure 1.4: The *Spitzer* Space Telescope (Image credit: Courtesy NASA/JPL-Caltech)

1.4.1 The *Spitzer* Space Telescope

The *Spitzer* Space telescope (Werner et al. 2004; Fig. 1.4) is the fourth and final member of NASA's great observatories program. *Spitzer* was launched in 2003 and has a 0.85 m mirror which during its cold mission was cryogenically cooled to 5.5 K by slowly boiling off liquid helium into space. It was placed into an Earth trailing orbit where it is far enough away that it is not affected by heat from the Earth and would not experience eclipses which cause undesirable temperature changes to the spacecraft. It has on board three science instruments working at wavelengths between 3.6 and 160 μm. The shorter near-infrared wavelengths are covered by the Infrared Array Camera (IRAC, Fazio et al. 2004) which has four channels operating at 3.6, 4.5, 5.8 and 8.0 μm respectively. Its field of view is $5.4' \times 5.4'$ and the detectors work in pairs such that while one is imaging a target the other is imaging an adjacent field, making a useful local background measure for environmental studies.

IRAC's three shortest wavelength channels (3.6, 4.5, and 5.8 μm) are sensitive to stellar emission from main sequence stars. These wavelengths are dominated by the emission from smaller stars that live longer and out number their massive counterparts and therefore in passive or evolved galaxies the peak of the emission is found in the near-infrared ~ 1.6 μm (see Fig. 1.5). In systems with intense star formation, like star-burst galaxies, massive (OB) stars, which have higher temperature photospheres, can dominate the energy produced shifting the peak to the UV-optical but their short lives mean that this would not last much longer than the duration of the star burst event

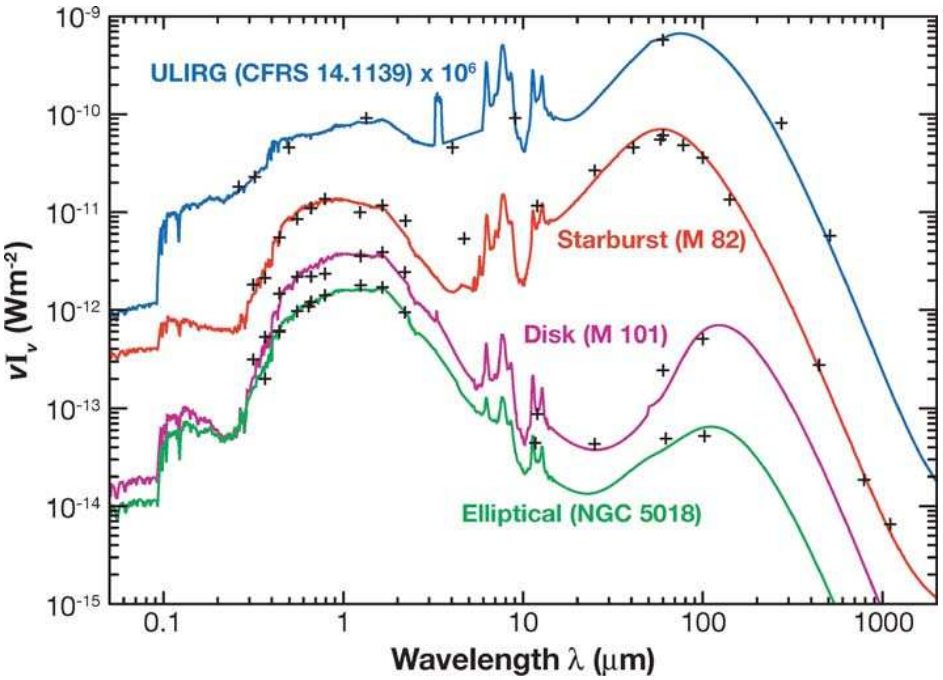

Figure 1.5: Spectral energy distributions of four different types of galaxy with increasing specific star-formation rates, from a passive evolved elliptical (NGC 5018) to a ultra-luminous-infrared-galaxy (ULIRG, CFRS 14.1139). Figure from Lagache et al. (2005).

itself. As redshift increases these three bands, and eventually the 8.0 μm band as well, will sample light emitted closer to the near-infrared peak of stellar emission. At $z \sim 3$ the 3.6 μm channel will be sampling light emitted at the peak of an evolved galaxy's stellar spectrum, thus creating a strong negative K-correction and hence these will be the most efficient bands in which to detect older stellar mass at these redshifts.

In May 2009 the last of *Spitzer*'s liquid helium boiled off after over 5 years of cooled operations. However this did not signal the end for *Spitzer*; its unique design meant that although the optics have warmed up they have remained at a temperature of $\sim$ 35 K, allowing observations in IRAC's two

shortest wavelength channels to continue with virtually no loss in sensitivity. This started the warm mission with observations at 3.6 and 4.5 μm, set to continue potentially until late 2013 when *Spitzer* will have drifted too far from Earth to communicate effectively. *Spitzer*'s IRAC instrument during both the cold and warm missions is used to look for galaxies in the environments of QSOs and RGs in Chapters 2 and 3.

1.4.2 The *Herschel* Space Telescope

While *Spitzer* has provided the highest sensitivity to date for observations in the near and mid-infrared for wavelengths between 3.6 and 24 μm its sensitivity and mirror size mean in the far-infrared (FIR) part of the spectrum (24-1000 μm) it was only really able to touch the surface and glimpse at the potential yield of observations at these wavelengths. The FIR emission from galaxies is dominated by the reprocessed UV-optical stellar light from dust enshrouded stars, which makes it a very useful tracer of star formation (Kennicutt, 1998) as during their early life stars are embedded inside clouds of gas and dust. Young massive stars dominate the energy output in the UV and this in turn dominates the reprocessed radiation that is emitted in the FIR from galaxies. Since massive stars have short life spans (a few Myr) their presence indicates recent star formation and hence, if you can measure the number of massive stars present this correlates with the star-formation rate (SFR) of the galaxy. It has been shown therefore that measuring the total FIR luminosity (L_{FIR}) between (8-1000 μm) can be used to determine a SFR (Kennicutt, 1998). This conversion has been shown to be a good measure of

Figure 1.6: The *Herschel* Space Telescope (Image credit: ESA (Image by AOES Medialab); background: Hubble Space Telescope, NASA/ ESA/ STScI)

the star formation in dusty star-burst galaxies where almost all the UV light from massive stars will be reprocessed and emitted in the mid to far-infrared. This tracer of star formation is very useful for dusty galaxies unlike many of the shorter wavelength tracers that are often used which are not accurate in dusty systems.

The mid and far-infrared with the exception of small windows in the atmospheric absorption, for example at 450 and 850 μm which have been observed by facilities such as the *James Clark Maxwell* Telescope on Mauna Kea, are almost impossible to observe from the ground. In the context of observing the history of the universe the importance of observations at these wavelengths is summed up by Dwek et al. (1998), Fixsen et al. (1998) and Driver et al. (2008). They show that roughly half of the energy emitted since the big bang by all objects has been absorbed by dust and then re-radiated between 60 and 500 μm. Indeed, galaxies with intense SFRs can in fact be dominated by emission in the FIR. Populations of luminous and ultra-luminous infrared galaxies (LIRGs and ULIRGs; see Fig. 1.5) were discovered in large numbers (Soifer et al., 1987) by The Infrared Astronomical Satellite (IRAS, Neugebauer et al. 1984) in the early 1980s. In extreme cases these galaxies can emit as much as 95 per cent of their energy in the far-infrared (Soifer et al. 1987; Sanders & Mirabel 1996). This highlights the importance of making observations at these wavelengths to understand the evolution of galaxies.

To make some of the first observations at wavelengths between 250-500 μm ESA launched The *Herschel* space telescope (Pilbratt et al. 2010; Fig. 1.6) in 2009. It boasts the biggest single mirror ever flown on a space

telescope of 3.5 m and three science instruments cooled to 0.3 K. It has been placed in an orbit around the Earth's L2 point for the same reasons as *Spitzer* was placed in an Earth trailing orbit. The two mapping cameras on *Herschel* are The Photodetector Array Camera and Spectrometer (PACS, Poglitsch et al. 2010) which observes at 70, 100 and 160 μm and The Spectral and Photometric Imaging REceiver (SPIRE, Griffin et al. 2010) observing at 250, 350 and 500 μm.

The *Herschel* Astrophysical Terahertz Large Area Survey (H-ATLAS, Eales et al. 2010) is the largest extragalactic open time key project to be given time on *Herschel*. When finished it will have surveyed 550 square degrees of the sky with both PACS and SPIRE down to depths of 33.5 mJy per beam at 250 μm. SPIRE data from the phase 1 release of the H-ATLAS survey is used to look for star formation in the environments of QSOs in Chapter 4.

1.5 In this Thesis

In this thesis I present the work I have conducted over the last 3.5 years studying the environments of a large number of high redshift AGN, mostly type-1 QSOs but also some RGs in Chapter 2. I have looked specifically for evidence of how the large scale environment influences AGN activity and vice versa by looking for relations between the observable properties of the AGN and their environmental density. I have aimed to extend the previous studies of AGN environments firstly to higher redshift than has been studied before, secondly to larger and more uniformly selected samples and thirdly to new

wavelengths using previously unavailable data or telescopes.

In Chapter 2 I utilise *Spitzer* space telescope data of one of the most uniformly selected samples of both radio-loud and quiet QSOs at high redshift. I address the question posed by the conflicting evidence in the literature about whether radio-loud AGN occupy, on average, denser environments than those which are radio-quiet. In Chapter 3 I use deep *Spitzer* data from the SERVS survey to look at QSO environments at $1.3 < z < 4.0$ and compare these with expectations from semi-analytic models, and also to the environments of the AGN studied in Chapter 2. In Chapter 4 I use data from the recently launched *Herschel* Space Telescope to look for star-formation in the environments of QSOs using FIR observations. Finally I summarise my findings and suggest potential for future work in Chapter 5.

Throughout this thesis a flat Universe is assumed with cosmology as follows $H_0 = 72$ km s^{-1} Mpc^{-1}, $\Omega_m = 0.3$ and $\Omega_\Lambda = 0.7$ and all magnitudes are quoted in the AB system unless explicitly stated otherwise.

Chapter 2

The Environments of $z \sim 1$ Active Galactic Nuclei

This Chapter is mostly based on work published in Monthly Notices of the Royal Astronomical Society (Falder et al., 2010).

2.1 Introduction

In this Chapter a large sample of AGN is used to study the environments that AGN are found in at $z \sim 1$, the sample was constructed with the aim of breaking the degeneracy found in most AGN samples between luminosity (i.e black hole mass) and redshift. This is an inherent problem with AGN samples selected from flux or volume limited surveys and can be seen in Fig. 2.1 which shows that at high redshift the flux limited SDSS does not have the sensitivity to detect the kinds of low luminosity AGN that it can detect at low redshift. Conversely the volume effect means that at low redshift the

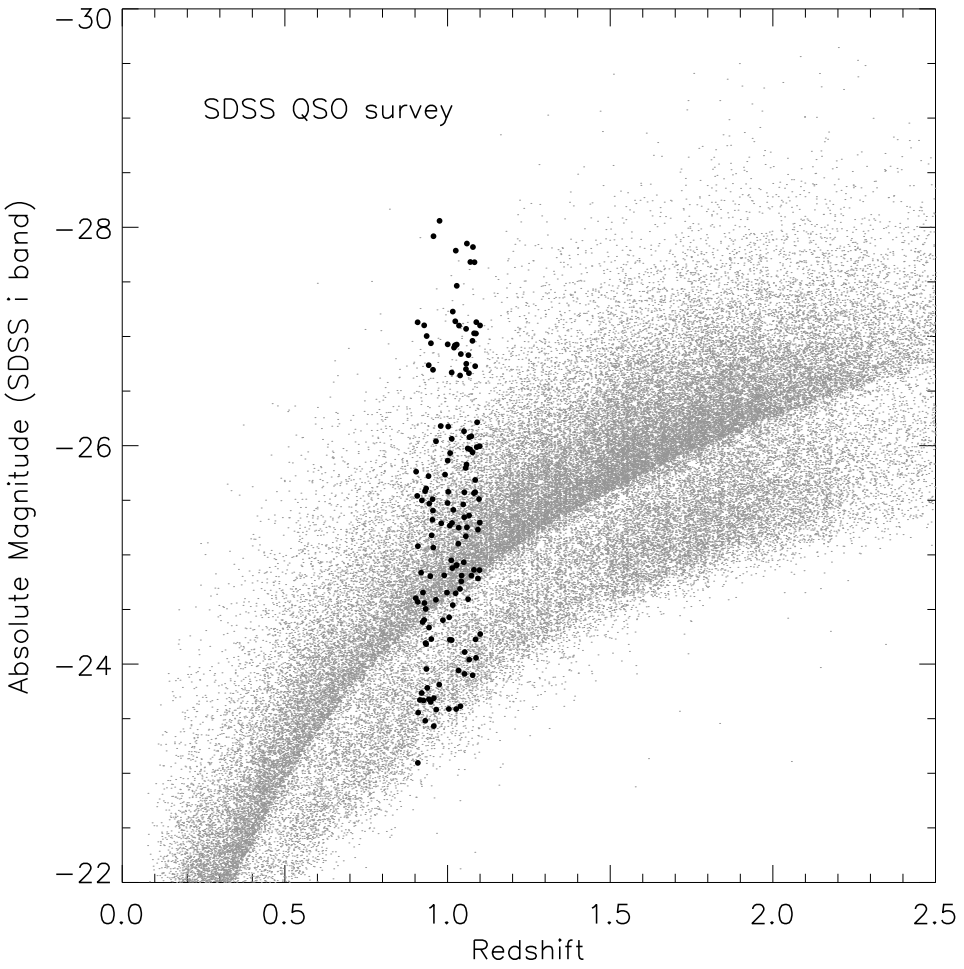

Figure 2.1: Redshift versus optical absolute magnitude (SDSS i band) for quasars from the fifth data release of the SDSS quasar survey (Schneider et al. 2005). The quasars in bold are those used in the $z \sim 1$ AGN sample, clearly showing that the sample spans the five magnitude range in optical luminosity that SDSS samples at $z \sim 1$. The different bands are due to the difference in depth between the main SDSS spectroscopic follow up and the deeper QSO spectroscopic follow up.

SDSS does not sample enough volume to observe the high luminosity types of AGN it finds at high redshift. To address this issue a sample of SDSS QSOs at a single cosmic epoch, $z \sim 1$, spanning a range of 5 magnitudes in their optical luminosity was devised. The sample of QSOs contains approximately equal numbers of radio-loud QSOs (RLQs) and radio-quiet QSOs (RQQs), selected in identical ways and matched in terms of their optical luminosities, and hence by proxy their black hole mass. In total 173 AGN environments are studied by supplementing the sample of SDSS QSOs with the known RGs at this epoch.

The AGN are studied by being split into their classical types (RLQs, RQQs and RGs), as well as looking for trends between their environments and their radio luminosities or black hole masses. Observations at 3.6 μm from *Spitzer* are used which samples light emitted near the peak of the rest-frame stellar spectrum at this epoch thus maximising the sensitivity to stellar mass. This work presents an analysis of the environments of the largest, most uniformly selected sample of luminous AGN yet assembled at high redshift. In so doing it forms an extension to previous studies of the environments of AGN with lower radio luminosities and at lower redshifts ($z < 0.3$) performed with SDSS data (e.g. Best et al. 2005; Kauffmann et al. 2008).

One of the key questions that can be addressed with this sample is the mixed view of the link between AGN radio-loudness and their environments. Many authors have found that radio-loud AGN generally inhabit denser environments (Yee & Green 1984; Ellingson et al. 1991; Hutchings et al. 1999 and more recently Kauffmann et al. 2008). However, there are equally convincing works that find there to be no difference in the environments (Yee

& Green 1987; Fisher et al. 1996; Wold et al. 2001 and McLure & Dunlop 2001b). Especially relevant to the sample presented here is the sample used by McLure & Dunlop (2001b), as this was also an AGN sample made up of RGs, RLQs and RQQs with the QSOs matched carefully in optical colours and luminosities following the same selection technique albeit at much lower redshift ($z < 0.3$), hence intrinsically less luminous AGN. The smaller sample size of only 44 AGN may also have precluded a significant difference from being observed in their sample if indeed there is one due to small number statistics.

In this Chapter first a number density analysis is conducted then the environments are studied using the spatial clustering amplitude (B_{gq}). In Section 2.2 details are given of the data used, in Section 2.3 the source extraction is discussed, in Section 2.4 the number density analysis is presented with the spatial clustering amplitude analysis presented in Section 2.5. This is followed by a discussion in Section 2.6 and a summary of the main conclusions in Section 2.7.

2.2 Data

The sample selection, observations and reduction for this work were completed prior to the start of my PhD by Matt Jarvis (Jarvis et al. in prep), a description of these are given here as the sample paper is not currently published or available anywhere else and the details of the sample are necessary to understand the analysis conducted in this Chapter.

2.2.1 Sample Selection

This sample referred to as the $z \sim 1$ AGN sample was designed to address the degeneracy between luminosity and redshift that is an inherent problem in AGN samples selected from flux or volume limited surveys. The idea was to construct an AGN sample at a single cosmic epoch, $z \sim 1$ was chosen for this as it allows QSOs spanning five magnitudes of optical luminosity (see Fig. 2.1) to be sampled. It is the lowest epoch where a large enough number of the highest luminosity QSOs can be sampled to compare with the QSOs found at the highest redshifts.

The sample is split into three sub-samples, all at the single cosmic epoch of $0.9 < z < 1.1$: 75 RLQs, 71 RQQs and 27 RGs. Observing both un-obscured (type-1) AGN, in the form of QSOs, and obscured (type-2) AGN, the RGs, also allows for tests of AGN unification schemes (e.g. Antonucci 1993).

The QSOs were selected by their optical colours in the fifth data release of the SDSS Quasar Survey (Schneider et al. 2005). Using the SDSS to select the QSOs allowed for a large enough initial sample that the RLQ and RQQ samples were chosen in identical ways. The initial sample that met the SDSS colour criteria for quasars was then cross referenced with the NRAO VLA Sky Survey (NVSS; Condon et al. 1998), the VLA FIRST survey (Becker et al. 1995) and the Westerbork Northern Sky Survey (WENSS; Rengelink et al. 1997) to pick out the RLQs and RQQs, full details of this process will be given in (Jarvis et al., in prep).

RLQs were chosen to have a low frequency WENSS 325 MHz flux density

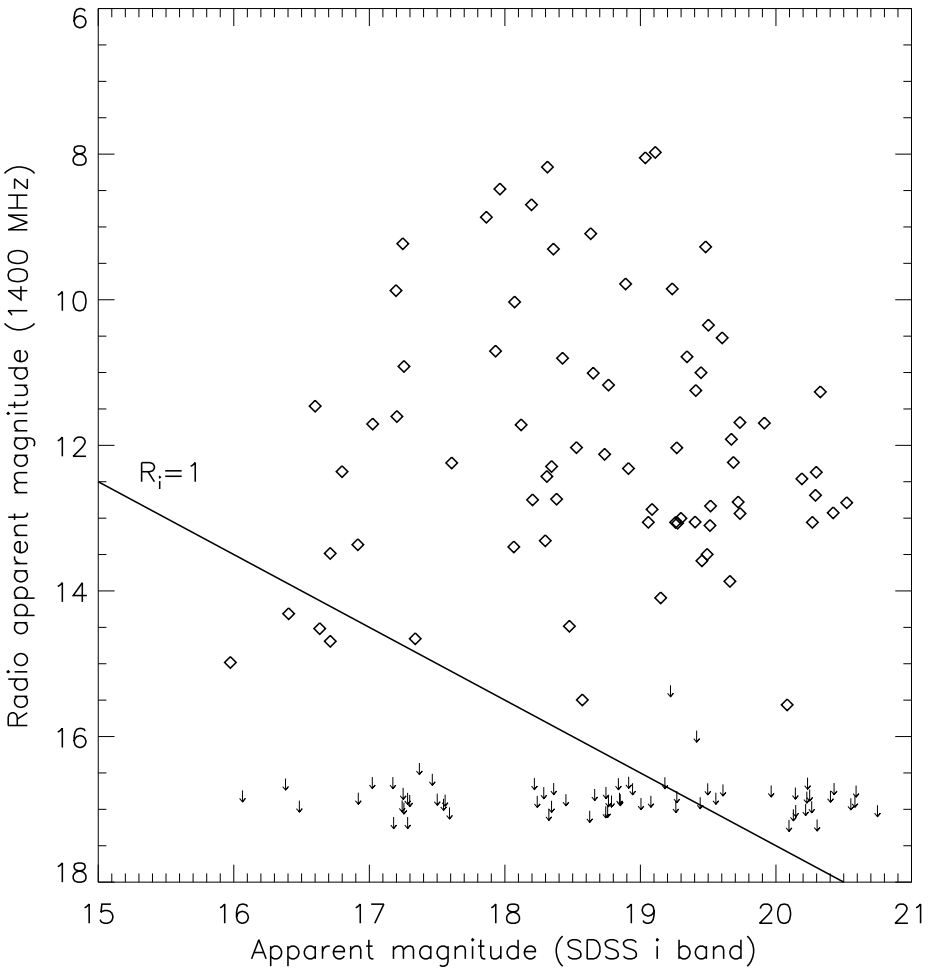

Figure 2.2: Optical apparent magnitude (SDSS i band) versus radio apparent magnitude (NVSS/FIRST 1400 MHz) for the QSO samples. RLQs radio data is from NVSS and are plotted as diamonds while RQQs upper limits are from FIRST. In the small number of cases where neither FIRST or NVSS data are available an extrapolation is made from the WENSS survey at 325 MHz (assuming $\alpha = 0.7$). The line shows the location where the parameter $R_{\rm i} = 1$ (Ivezić et al. 2002; explained in text) which is used to determine radio-loudness, *i.e.* objects falling above the line are classified as radio-loud while objects falling below the line are classified as radio-quiet. The plot shows that, by this definition, all but four of the RLQs would be classified as radio-loud and that at least two thirds and likely more of the RQQs would be classified as radio-quiet.

of greater than 18 mJy which is the 5 σ limit of the survey. In the small regions where the there was no coverage of the SDSS by WENSS the 325 MHz flux was extrapolated from the NVSS 1400 MHz flux using a spectral index of $\alpha = 0.7$. At $z \sim 1$ this flux level corresponds to a radio luminosity almost entirely within the radio-loud domain. Fig. 2.2 compares the sample to an alternative definition of radio-loudness used by Ivezić et al. (2002). Here radio-loud objects are defined to have a radio loudness parameter of $R_{\rm i} > 1$ where $R_{\rm i} = \log(F_{\rm radio}/F_{\rm i})$ and $F_{\rm radio}$ and $F_{\rm i}$ are flux densities measured at 1.4 GHz and in the i band respectively (K-corrections are not applied). With the exception of four objects, all of the RLQs would also be considered radio-loud using this definition. It is worth noting that these four objects have only one flux density measurement at radio wavelengths, and hence may in fact fall above the line if their spectral indices differ from the assumed value of 0.7 which is the mean value of the measured spectral indices. Using a low frequency radio flux to define the RLQs allows them to be compared more easily to the RGs without a severe orientation bias due to beaming.

The RQQs were defined as being undetected by the 1400 MHz FIRST survey at the 5 σ level. FIRST was used for this definition because it provides a more sensitive flux density limit than WENSS. Hence the RQQs are not selected as radio-quiet objects as defined by the radio-loudness parameter but instead as having at least an order of magnitude lower radio luminosity than the RLQs. In order to get an estimate for the average radio power of the RQQs in the sample the FIRST radio images of non-detections were stacked to reveal the average value of the radio power (following the procedure of White et al. 2007). In essence the technique involves stacking

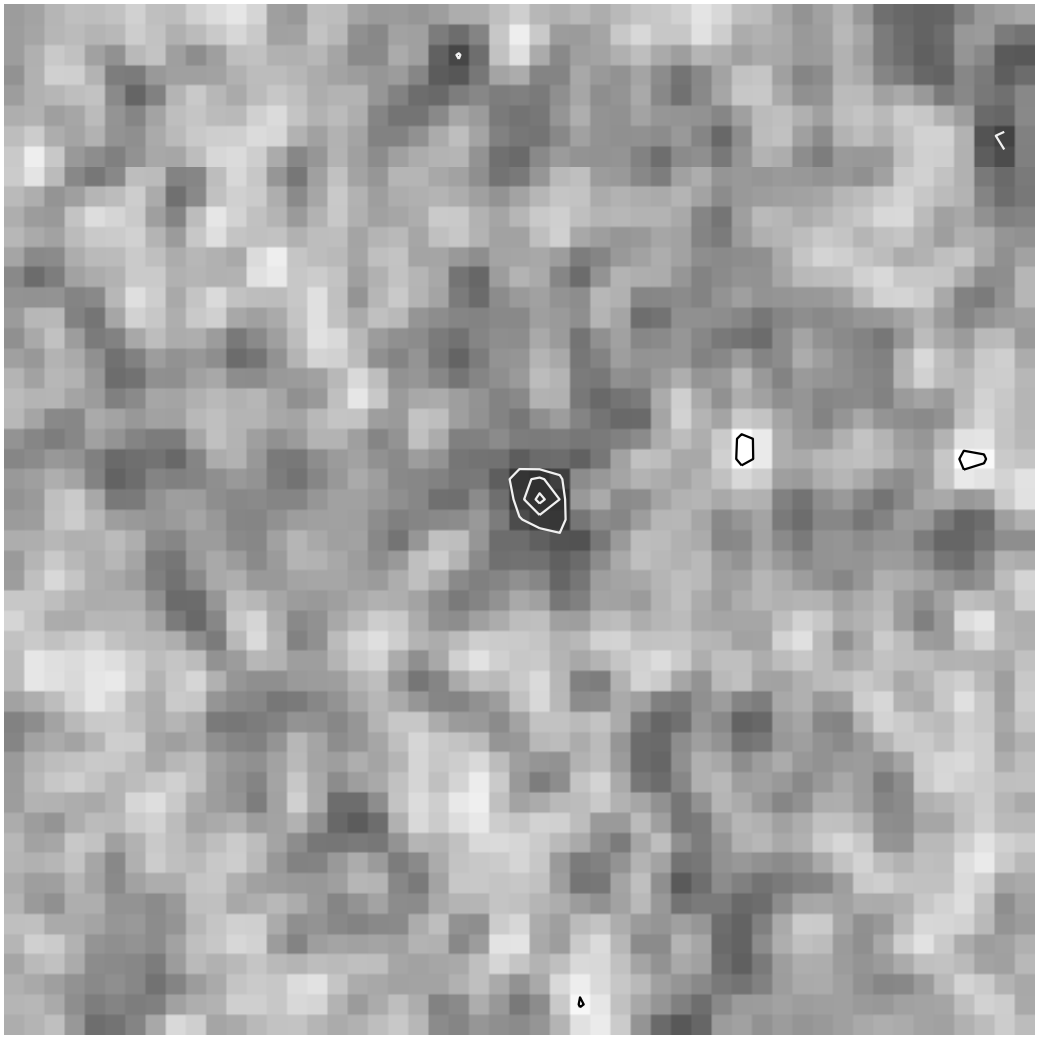

Figure 2.3: Stacked and averaged radio image of the positions of the RQQs in the sample using data from the FIRST survey on the VLA at 1400 MHz. The contours show the 3, 4 and 5 σ levels. Black contours are negative and white positive. The image dimensions are $1.5' \times 1.5'$.

the radio images at the known positions of the RQQs, weighting each image by its standard deviation (noise) and then computing the average radio emission or obtaining a sensitive upper limit. The stacked image is shown in Fig. 2.3. Using this technique an average flux density for the RQQs at 1400 MHz of 0.10 ± 0.02 mJy is found (*i.e.* a 5 σ detection). Assuming a spectral index of 0.7 allows this to be extrapolated to a 325 MHz flux density of 0.30 ± 0.06 mJy which at $z \sim 1$ corresponds to a 325 MHz luminosity, $\log_{10}(\mathrm{L}_{325}/\mathrm{W\ Hz^{-1}\ sr^{-1}}) = 23.02$.

Lists of ~ 75 RLQs and RQQs (after observation this resulted in 75 and 71 usable targets respectively) were chosen for observation that were matched in optical luminosity and span the full five optical magnitudes available. In addition, the targets were chosen to have redshifts optimised, within the chosen range for follow-up CO surveys with interferometers such as the Atacama Large Millimetre Array (ALMA). The selected sources are shown in bold in Fig. 2.1, and the distribution of optical magnitudes within the selected redshift range is shown in Fig. 2.4. They were specifically selected to be well matched in terms of the QSOs optical luminosity and a two sample Kolmogorov-Smirnov (K-S) test does not allow the rejection of the null hypothesis that they are indeed drawn from the same parent population giving d = 0.13 and a probability of 0.52 for the null hypothesis.

The RGs were selected from the low frequency, (178 or 151 MHz; hence orientation independent) radio samples 3CRR (Laing et al. 1983), 6CE (Eales 1985), 7CRS (Willott & et al. 1998) and TOOT surveys (Hill & Rawlings 2003). Together, these surveys give 27 RGs in the same $0.9 < z < 1.1$ redshift range as the QSOs. The reason therefore for the substantially smaller RG

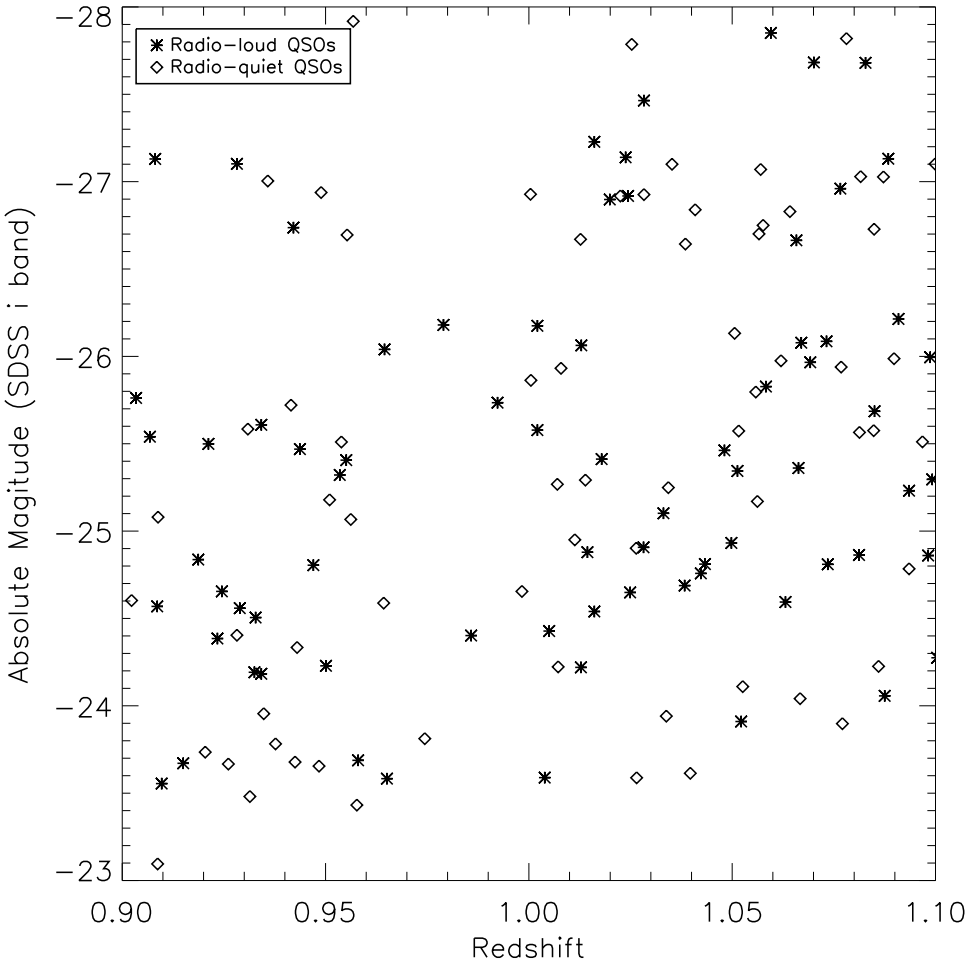

Figure 2.4: Optical absolute magnitude (SDSS i band) versus redshift for the QSOs in the sample. RLQs are shown with asterisks and RQQs with diamonds.

sample is purely due to the limit of the known RG population at $z \sim 1$. Analysis of the RGs' *Spitzer* data is presented in Fernandes et al. (2011).

The radio luminosity distribution of the full sample is shown in Fig. 2.5 which shows that, on average, the RGs are more radio-luminous than the RLQs, albeit with a significant overlap. Again using the FIRST radio images upper limits on the radio emission of each RQQ were measured; see Fig. 2.2 and Fig. 2.5, which shows that at least two thirds of the RQQs and most likely more would be classified as radio-quiet using the definition from Ivezić et al. (2002). In comparison to these limits the least radio-loud RLQ has a 325 MHz luminosity of $\log_{10}(\mathrm{L}_{325}/\mathrm{W\ Hz^{-1}\ sr^{-1}}) = 24.5$, showing that there is at least an order of magnitude difference (several between the means) in the radio emission of our RQQs and RLQs. The reason for the gap between the RLQs and RQQs in radio luminosity seen in Fig. 2.5 is due to the difference in the survey depths of WENSS and FIRST from which they were selected. The 5 σ limits used for the RLQ lower limit and the RQQs upper limit are not the same, as shown by the dashed and dotted lines in Fig. 2.5. This leaves a region on the radio luminosity axis uncovered by this sample, it is important to note this is due to the selection rather than evidence for or against a radio power dichotomy. This gap should enhance any differences between RLQs and RQQs environments the sample is not simply a continuum of radio powers split in half.

A full list and details of the objects that make up the $z \sim 1$ AGN sample are given in Appendix A.

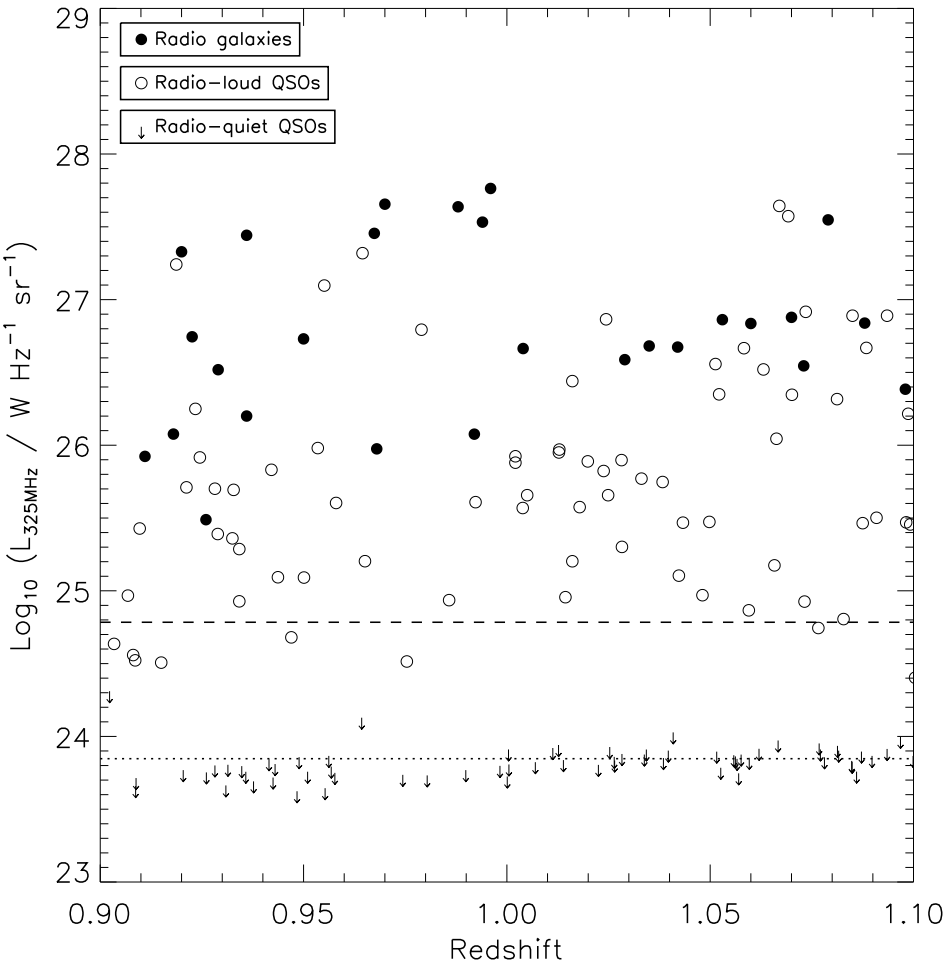

Figure 2.5: Low frequency radio luminosity versus redshift for the sample. RLQs are shown with open circles and RGs with filled circles (data are rest-frame 325 MHz from WENSS). For the RQQs, 5σ upper limits (extrapolated to rest-frame 325 MHz) from the FIRST survey are shown. Where WENSS data were unavailable for the RLQs due to sky coverage (about 10 objects) the rest frame 325 MHz flux density was extrapolated from the NVSS survey at 1400 MHz assuming a spectral index of $\alpha = 0.7$. The dashed line shows the average 5σ limit of the WENSS survey, converted to a luminosity at $z = 1$ by assuming $\alpha = 0.7$; the RLQs were selected to have radio luminosities falling above this line. The dotted line shows the average 5σ limit of the FIRST survey, extrapolated to 325 MHz and again converted to a luminosity; the RQQs were selected to have a radio luminosity falling below this line. The assumed spectral indices for some conversions explains why some objects fall between the lines on this plot.

2.2.2 Observations and Data Reduction

The data used in this Chapter consist of near-infrared images of the 173 AGN that make up the $z \sim 1$ AGN sample taken at 3.6 μm with the IRAC camera on-board the *Spitzer Space Telescope*.

All targets which were within the regions of the *Spitzer* Wide-Area Infrared Extragalactic Legacy Survey (SWIRE; Lonsdale et al. 2003) and the Extragalactic First Look Survey (XFLS; Lacy et al. 2005) were omitted from the *Spitzer* observations. As the data in the archive for these objects was deeper than was required (Richards et al., 2006b); there are two RLQs and fifteen are RQQs. It was also found that two of the 3C RGs had adequate data in the archive: 3C 356 (ID3329; PI Stern) and 3C 184 (ID17; PI Fazio). These data were downloaded from the *Spitzer* archive and added to the new observations which are described below.

The new IRAC observations were carried out in all four bands along with MIPS at 24 μm between 2006 August and 2007 August in program ID30344 (PI Jarvis). They consisted of 5pt Gaussian dithers with the medium cycling pattern and 12 sec frame-time to ensure good scattered light rejection and good photometry. The data were reduced with the standard pipeline version S15.0.5 giving final maps with a pixel scale of 1.2″. In this Chapter the 3.6 μm data are used to study the environments of the AGN since it samples light emitted at 1.8 μm at $z \sim 1$ which is the closest of these bands to the peak of the stellar emission from galaxies, therefore maximising our sensitivity to evolved stellar mass in galaxies at $z\sim1$. An aperture correction of 1.48 was applied to the 3.6 μm flux densities, as determined by the *Spitzer* First Look

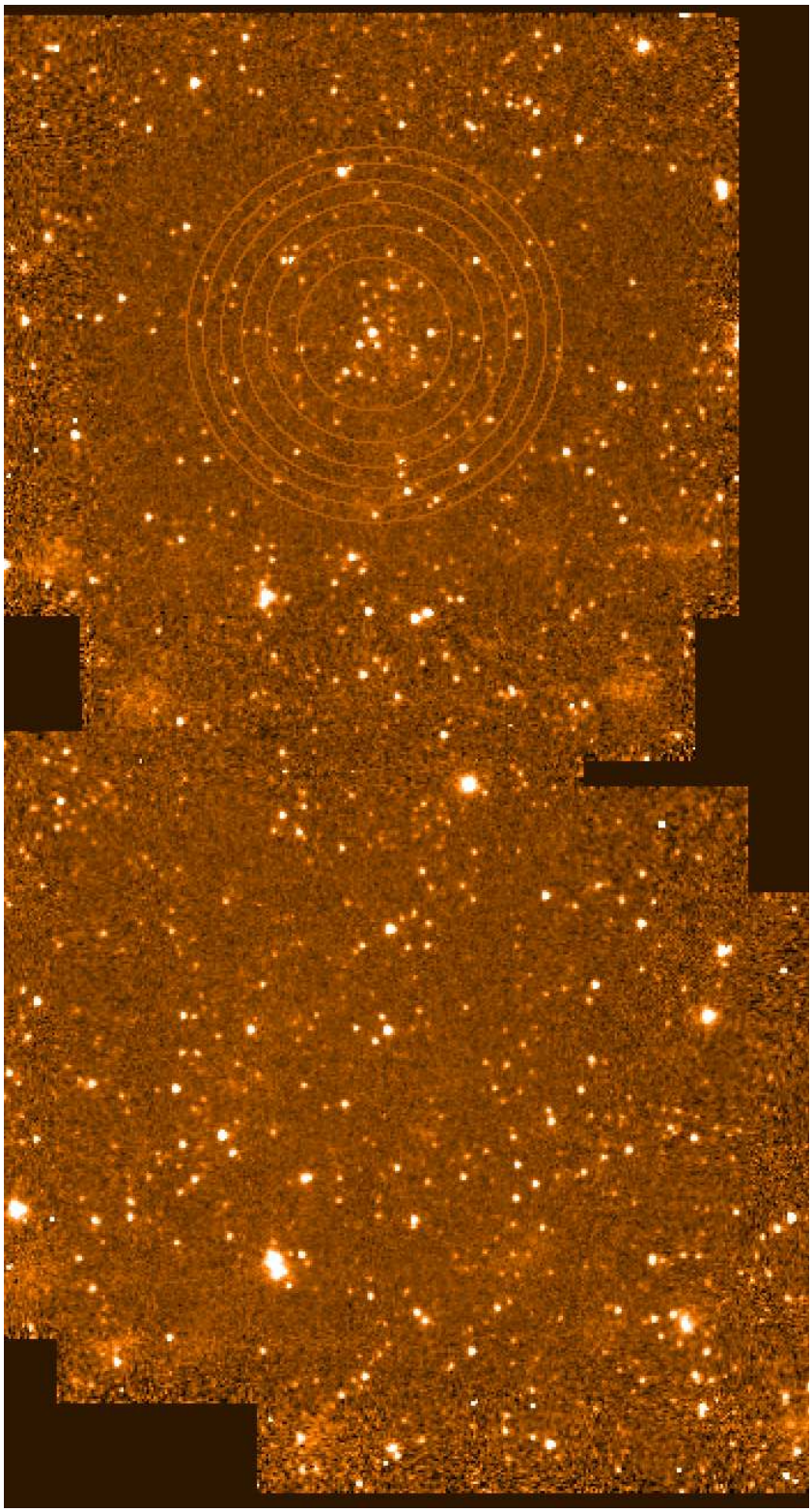

Figure 2.6: An example of one of the IRAC 3.6 μm images (radio-quiet QSO SDSS151520.56+0004739.3) showing the annuli used for the analysis and the adjacent field that is used as a measure of the local background source density. The QSO is in the centre of the annuli and the furthest annulus from the QSO measures 90″ in radius.

Survey (Lacy et al. 2005). Full details of the observations, data reduction and analysis of the QSO's *Spitzer* data will be given by Jarvis et al. in prep. An example of one of the 3.6 μm images is shown in Fig. 2.6.

2.3 Source Extraction

The images were cut down in size using IRAF tasks to leave $\sim 4' \times 4'$ square images centred on the position of the AGN. This process removes any edge effects and underexposed edges caused by the dither pattern, but leaves enough area to sample the AGN environment out to a radius of 700 kpc at $z \sim 1$. The SExtractor software package (Bertin & Arnouts, 1996) was used to create catalogues of the sources in the images. The default set up with a detection threshold of 3 adjacent pixels each at 1.5σ above the RMS background level was used. The SEEING_FWHM was set to 1.67 arcsec which is the measured resolution of the images. On inspection of a sample of the output catalogues it was found that the default value for the deblending parameter (0.005) resulted in the non-detection of faint sources close to bright AGN and stars, see Fig. 2.7. Therefore the value used by Lacy et al. (2005) of 0.0001 was adopted which gave a significant improvement, although in a small number of cases it led to the inclusion of spurious sources identified with diffraction spikes.

To check for spurious sources the maps were inverted and the same source extraction configuration was run on these, see Fig. 2.8. The results showed that 96 per cent of the fields had no spurious 5σ sources. However, the remaining 4 per cent had spurious sources associated with the diffraction

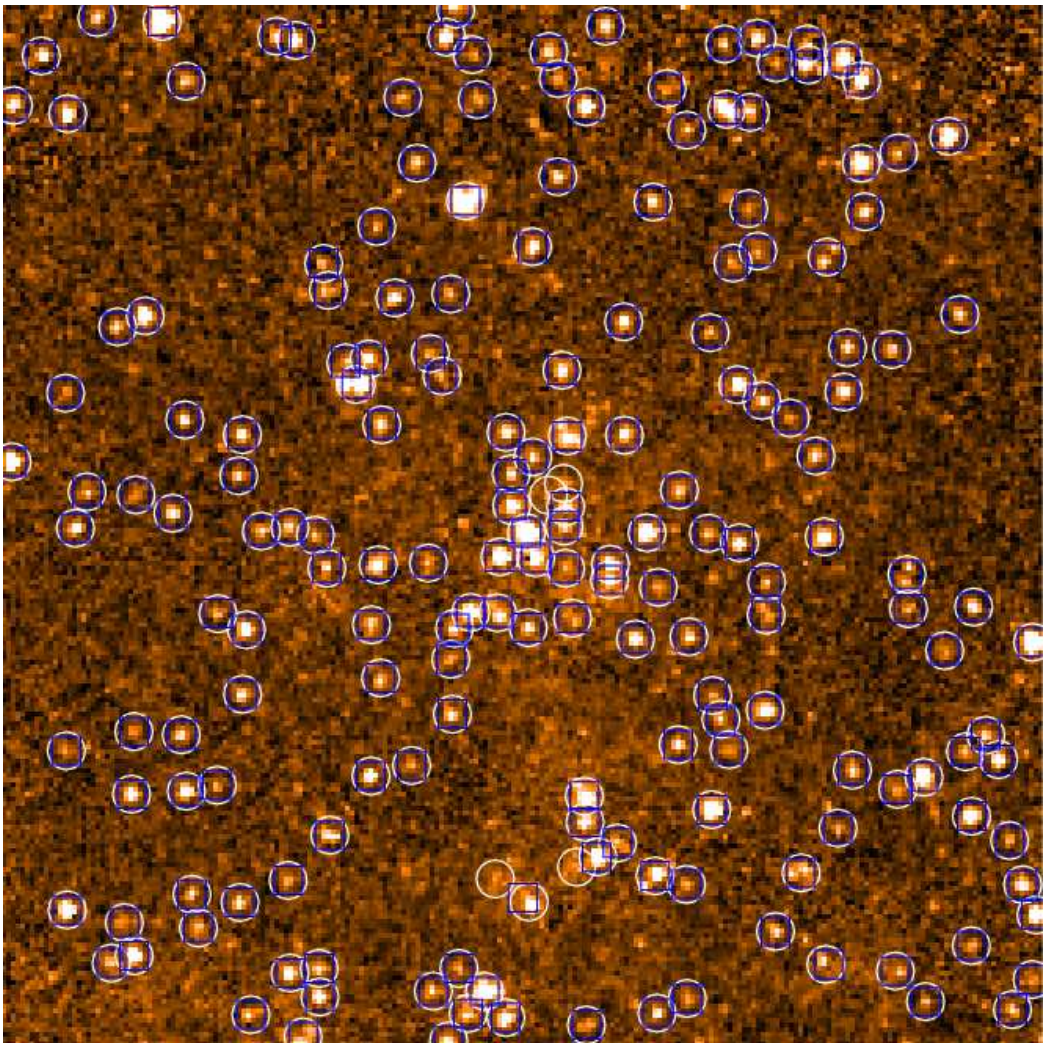

Figure 2.7: An example of the SExtractor source extraction on an AGN field (radio-quiet QSO SDSS151520.56+0004739.3). The QSO's location is in the very centre of the image. Over-plotted are the 5σ (> 13.183 μJy) sources extracted with the default value of the deblending parameter (0.005) in blue squares and that used by Lacy et al. (2005) of 0.0001 in white circles. The adopted value of deblending (0.0001) results in an additional 4 sources in this map, however importantly two of these are very close to the central QSO hence exactly the sources that are potentially in the QSO's environment. The image measures $\sim 4' \times 4'$.

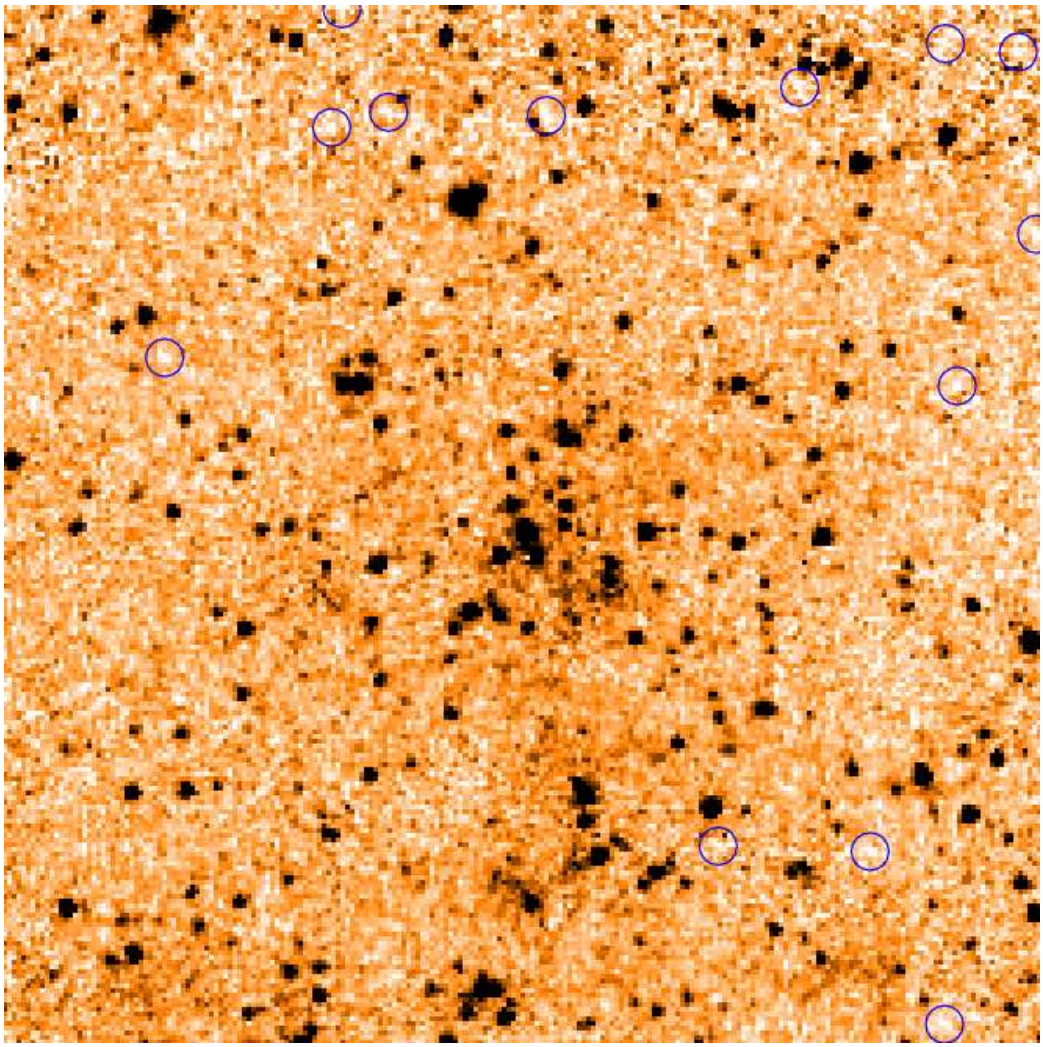

Figure 2.8: The same map as shown in Fig. 2.7 but inverted to check for spurious sources over-plotted are 13 extracted sources; however none of these are 5σ (> 13.183 μJy) and so would not be used in the analysis. The image measures $\sim 4' \times 4'$.

spikes of bright stars (which produce pronounced negative artefacts). This method was thus used to identify those images affected by diffraction spikes and then their non-inverted catalogues were checked for sources that were obviously spurious, these were then manually removed from the catalogues.

The source extraction was also checked using the three northern fields of the SWIRE survey by extracting catalogues with SExtractor of these fields and comparing with the SWIRE team's own catalogues. The SExtractor catalogues recover 96 per cent of the sources in the SWIRE catalogues and of those the fluxes also agree at the 98 per cent level. The SExtractor catalogues contain around 16 per cent more sources that are not found in the SWIRE catalogues but these are low signal to noise in the SExtractor catalogues and are thus not likely to be included in the more conservative SWIRE catalogue due to the higher signal to noise cut and the SWIRE catalogue's requirement for a detection at both 3.6 and 4.5 μm.

2.3.1 Catalogue Filtering

The catalogues were filtered to reduce the noise produced by spurious sources or foreground stars, hence to enhance the number of galaxies potentially associated with the AGN over other sources in the catalogues allowing for a stronger signal.

In order to ensure that all images were of the same sensitivity a cut was made of source detections below a conservative 5 σ level (see Fig. 2.9). This level is defined as the 5 σ level of the shallowest image in the sample thus ensuring that any sources used could be detected in any image. The cut is

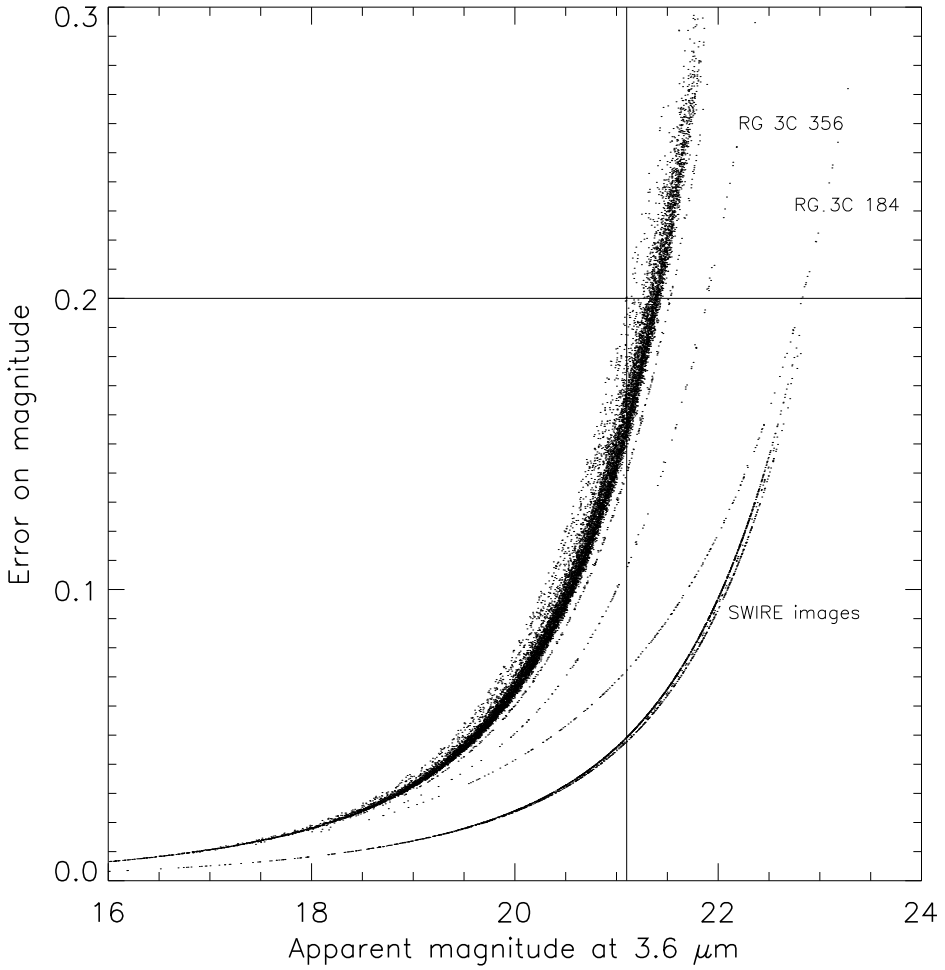

Figure 2.9: The apparent magnitudes of all sources at 3.6 μm versus the error on that magnitude. The deeper SWIRE images are labelled, and the lines show the 0.2 magnitude error (5σ) level and the corresponding magnitude for the shallowest image, *i.e.* 21.1 mag. The two other smaller bands shown and labelled are from the two RGs which had already been imaged by other programs; see the text for details.

especially necessary because of the use of images from SWIRE and the other archive data which are deeper than the rest of the observations. Using this method, all sources in our fields with apparent magnitudes fainter than 21.1 (13.1 μJy) were excluded from the analysis. To put this limit into context, the absolute magnitude of the break in the K-band galaxy luminosity function at $z \sim 1$ is $K^* = -23.0$ (Cirasuolo et al. 2010). An elliptical galaxy at $z \sim 1$ has $K - 3.6 = 0.27$ (Bruzual & Charlot 2003) giving an equivalent break in the 3.6 μm luminosity function of -23.3 or an apparent magnitude of $m^*_{3.6} \sim 20.8$. Thus at the 5 σ depth the data are sensitive to galaxies with 3.6 μm luminosities of $\sim 0.3L*$ or greater, *i.e.* galaxies representing the bulk of the stellar mass at this epoch. This wavelength is sampling star-light emitted long-wards of the Balmer break at $z \sim 1$ so any companions to the AGN are likely to be galaxies with a substantial old stellar population.

In order to remove foreground stars the SExtractor CLASS_STAR output parameter was used. This returns a value between 1 and 0 where 1 is a perfectly star-like object and 0 is very non-star-like. All sources that have a CLASS_STAR parameter greater than 0.8, as used by Best et al. (2003) and Smith et al. (2000) were excluded from the analysis. The same analysis was conducted using a CLASS_STAR value of 0.95, another commonly adopted value, and found almost identical results, suggesting that most objects cut at the 0.8 level had values greater than 0.95. These values may also remove QSOs from the catalogues, but given the space density of luminous QSOs in SDSS at this epoch they are unlikely to form a substantial part of each others local environments.

2.4 Number Density Analysis

2.4.1 Radial Search

The catalogues were searched for sources in annuli working out from the target AGN. The annuli were kept to a fixed area, rather than fixed width; this keeps the signal-to-noise and Poisson errors of similar size from bin to bin and also allows for a larger number of annuli. The target AGN is excluded from the counts by excluding any source within 1 $''$ of the AGNs' coordinates (SDSS for the QSOs, K-band for the radio galaxies), as this would bias the results towards there being an over-density in the first bin.

To get an estimate for the average number of counts in the field to compare with the AGN fields the extra adjacent field that comes with *Spitzer* images was used. This extra field is a result of the way *Spitzer* works, IRAC which has four detectors can only point two at the target at any one time so the telescope has to offset slightly to allow the other two detectors to image the target. While this happens the un-targeted detectors image a region of an adjacent field to the same depth as the target fields. As these fields are not targeted at the AGN they can be used as blank or control fields, and were thus treated in exactly the same way as the AGN fields. Hence the region with the same exposure time as the main fields was source extracted in the same manner as the AGN fields and the average source density was computed. Fig. 2.6 shows an example 3.6 μm image showing the annuli used in the analysis and the adjacent field used as the background measure.

It is also possible to use the blank fields to get a measure of the local foreground and background in each region and subtract the mean source

density in each blank field from its AGN field. In this case, the source over-density is measured rather than just the source density, which better allows stacking of the results. One possible pitfall of this approach is that the blank fields might be close enough to the AGN that any over-density will extend into them. The proximity of blank fields to the target fields is therefore a trade-off between the desire to subtract a local foreground whilst not wanting to be so close that any over-density is also subtracted.

The blank fields should be sufficiently far from the AGN as there is evidence in the literature that over-densities for the most powerful radio galaxies (at $z \sim 1.6$) extend out to, at most, 1.6 Mpc (Best et al. 2003) whereas the blank fields are at their closest point $\sim$2.8 Mpc (at z $\sim$1) from the AGN. In addition if the blank fields are broken into strips there is no increase in source density towards the AGN.

The calculated average source density in the blank fields is 8.04 ± 0.07 arc min^{-2}, where the error is the Poisson error on the number of sources counted. The average source density from the three northern fields of the SWIRE survey (covering ~ 25 deg^2) is 8.13 ± 0.01 arc min^{-2}, hence the two measurements are consistent with each other. There will also be a cosmic variance associated with the smaller size of the combined blank fields ($\sim$ 0.5 deg^2) in comparison to the SWIRE fields.

Cosmic variance errors are caused by the clustering of sources on different scales in the sky. They are a function of the size of the area used to work out the source density and will decrease to zero when the field is so large that variations in structure are on a much smaller scale than its size. To estimate the cosmic variance on a field the size of the 173 blank fields, 173

regions were extracted from the SWIRE images each having an equal area to one of the blank fields. This gives a mock survey of equivalent area to that of the real survey. This procedure was repeated as many times as possible without using the same region twice which allowed 43 sets of 173 regions to be extracted. The mean value of the source density was calculated for each of the 43 sets of regions and the standard deviation of these 43 measurements was considered the combined cosmic variance and Poisson error on an area the size of the blank fields; removing in quadrature the known Poisson error gives a value of ± 0.48 arc min^{-2} for the cosmic variance.

2.4.2 Completeness

In order to measure and correct for the completeness of the data extensive simulations to add and recover artificial sources were conducted. These involved adding 1000 sources into each of the AGN fields at 30 flux levels (*i.e.* 30000 sources per image) and proportionally less for the blank fields as they are of a smaller area. The added sources were Gaussian with a FWHM of 2 $''$, and were normalised to have the required flux. They were added across each image in a grid pattern in batches of 100 at a time for the AGN fields, with proportionally less for the blank fields, this is to avoid increasing the confusion of the image by adding too many sources at once. The sources were allowed to randomly move around within the grid as far as possible without two sources ever being placed close enough as to become blended. An example of the added artificial sources is shown for RG 3C175.1 in Fig. 2.10. Sources were considered to be recovered if they were found in the SExtrac-

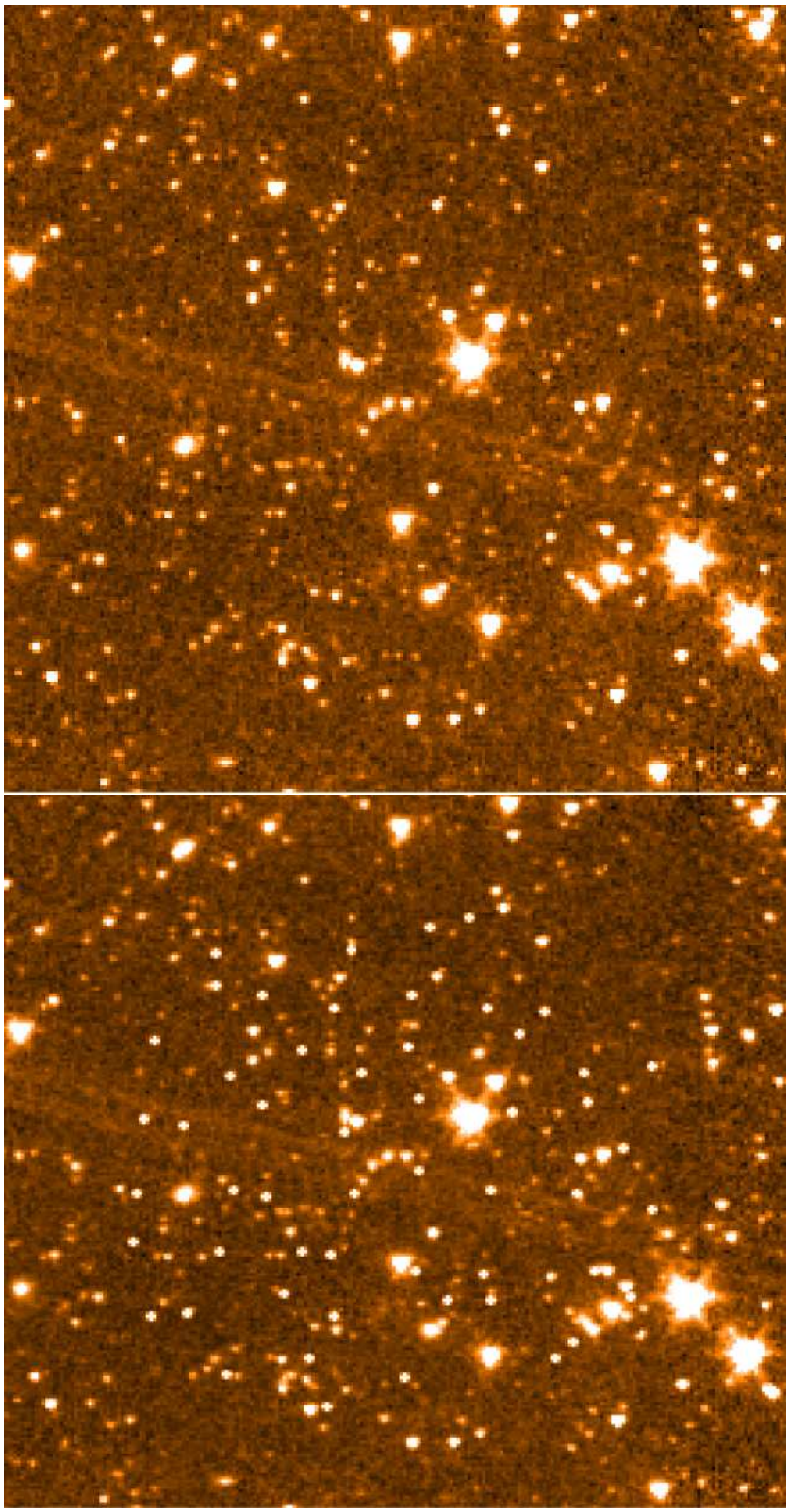

Figure 2.10: Example of IRAC 3.6 μm images of RG 3C175.1 with inserted artificial sources for the completeness simulation added to the region covered by the annuli used in radial search. Both panels have 100 artificial sources added, in the top panel these are at the images' flux limit of 13.1 μJy and in the bottom panel these are of 100 μJy. The images measure $\sim 4' \times 4'$.

TOR catalogues within 1.5 pixels (1.8 arcsec) of their input position and had an extracted flux within a factor of 2 of the input value. In the AGN fields the completeness was computed for each annulus individually which allows a correction to be made specific for that annulus which helps to correct for bright objects that are masking regions of certain annuli. In the blank fields the average completeness was used because from the blank fields only one value of the source density is needed per field.

To eliminate the scatter in the measured completeness they were fitted with an empirical model of the form $completeness = (S^a)/(b+cS^a)$ (Coppin et al. 2006) where S is the 3.6 μm flux density and a, b and c are constants that are fitted. An example of one of these fits with the overlaid data points is shown in Fig. 2.11 along with the mean completeness of all the observations obtained for this work. In both cases the catalogues are shown to be more than 80 per cent complete at the flux limit adopted for the analysis. Measuring the completeness for each annulus allowed different completeness corrections to be applied to each annulus in each image as a function of flux.

As might be expected, the completeness is found to be lower than average in the first annulus of the QSO fields which is due to the bright QSOs hindering the detection of faint sources. This effect was also noted by Yee & Green (1984). Indeed, there is a significant correlation between the optical luminosity of the QSOs and the completeness of the first annuli at the 99.7 per cent level (see Fig. 2.12), using correlation analysis (Spearman rank and Kendall tau). Hence applying the completeness corrections was found to boost the source density in the first annulus relative to the others (although the significance is not changed as the error is also scaled by the completeness). This

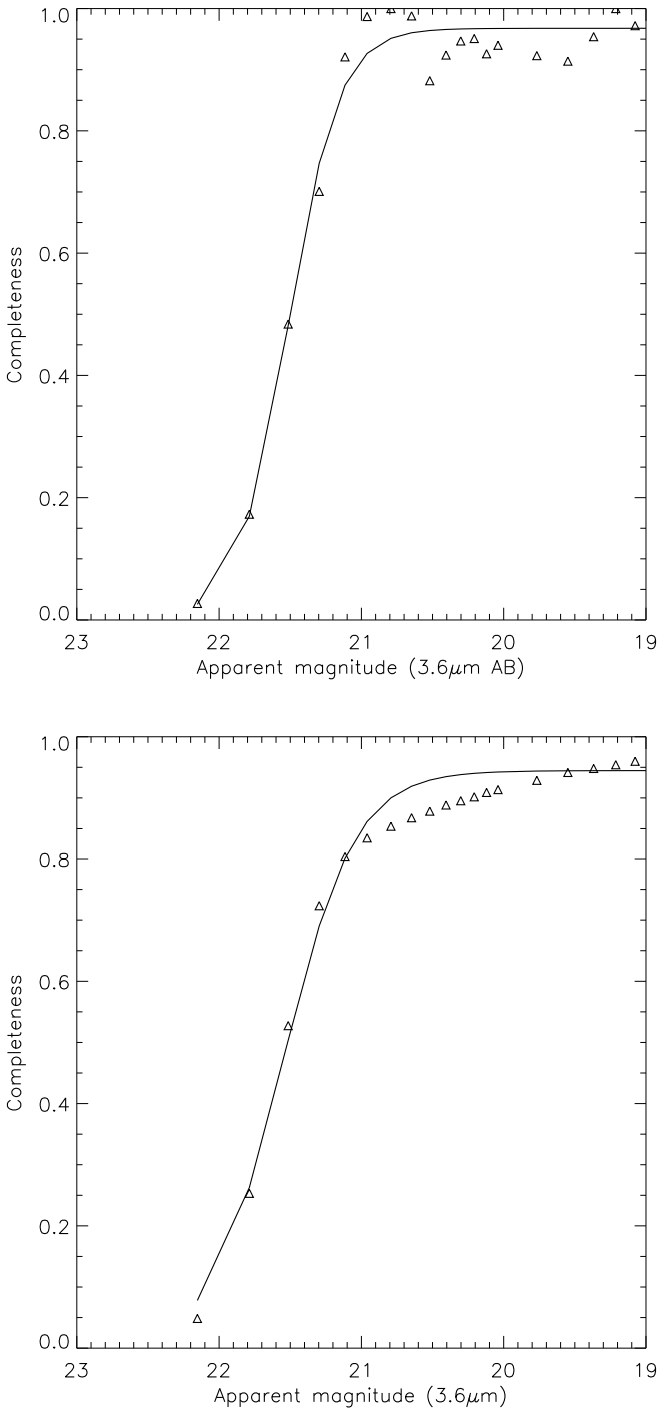

Figure 2.11: The top panel shows an example of a completeness curve for one annulus of an AGN field and the bottom panel shows the mean completeness of all the observations obtained for this work (*i.e.* excluding deeper data from the archive which is more complete). In both cases the fit is an empirical model described fully in the text. The flux limit used in the analysis is 13.1 μJy (21.1 mag) which is therefore the lowest flux at which a completeness correction is made, both panels show that at the conservative flux limit used the catalogues are more than 80 per cent complete.

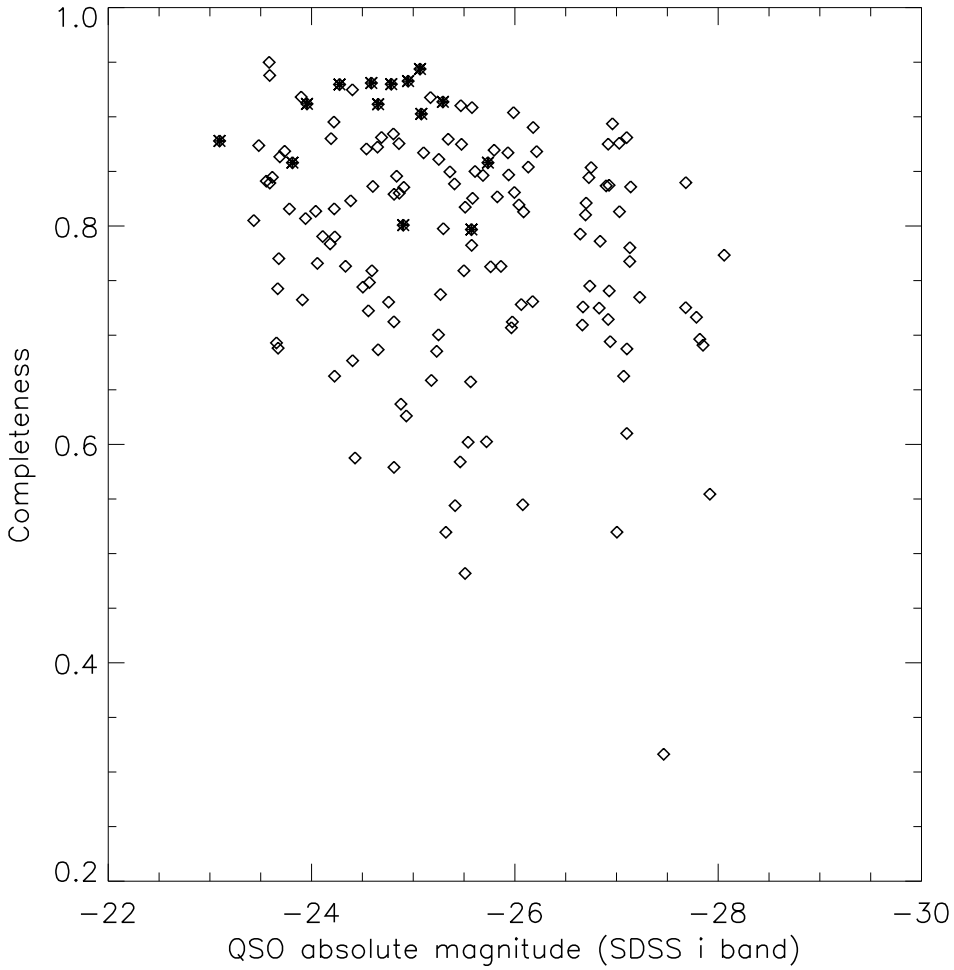

Figure 2.12: Plot showing the optical luminosity (rest-frame SDSS i band) versus the completeness at the flux limit (13.1 μJy) in the first annulus for all the QSOs in the sample. Correlation analysis shows a correlation significant at the 99.7 per cent level. Completeness from the deeper SWIRE data are shown with stars, which as can be seen are concentrated towards higher (> 80 per cent) completeness. With the exception of one outlier around one of the brightest QSOs all the first annuli are ($\gtrsim 50$ per cent) complete at the adopted flux limit.

effect is not seen in the RG fields as they are generally less luminous in the optical/near-infrared, due to the quasar nucleus being obscured so that only the stellar light from the host galaxy is seen.

2.4.3 Number Density Results

Conducting the radial search on individual AGN fields does not give significant results because the catalogues are dominated by foreground sources and there are large Poisson errors resulting from counting small numbers of objects. In practice detecting low level over-densities, which the environments of luminous high z QSOs appear to be (e.g. McLure & Dunlop 2001b) requires two things. Firstly an accurate background determination with which to compare the target fields, then in order to detect an over-density, if one exists, the fluctuations in the background source-density that is contaminating the search region must be at a lower level than the signal from the over-density. Stacking helps in achieving the second of these requirements as fluctuations will be both positive and negative whilst an over-density will always be positive. Hence this thesis mainly concentrates on a statistical analysis of stacked data from multiple fields.

2.4.4 Over-Density for the whole AGN Sample

In Fig. 2.13 the results of a radial search conducted on all the AGN fields, centred on the AGN, stacked and averaged is shown. Note that the local background level calculated from the blank field of each AGN has been subtracted so the plot shows source over-density rather than source density. The

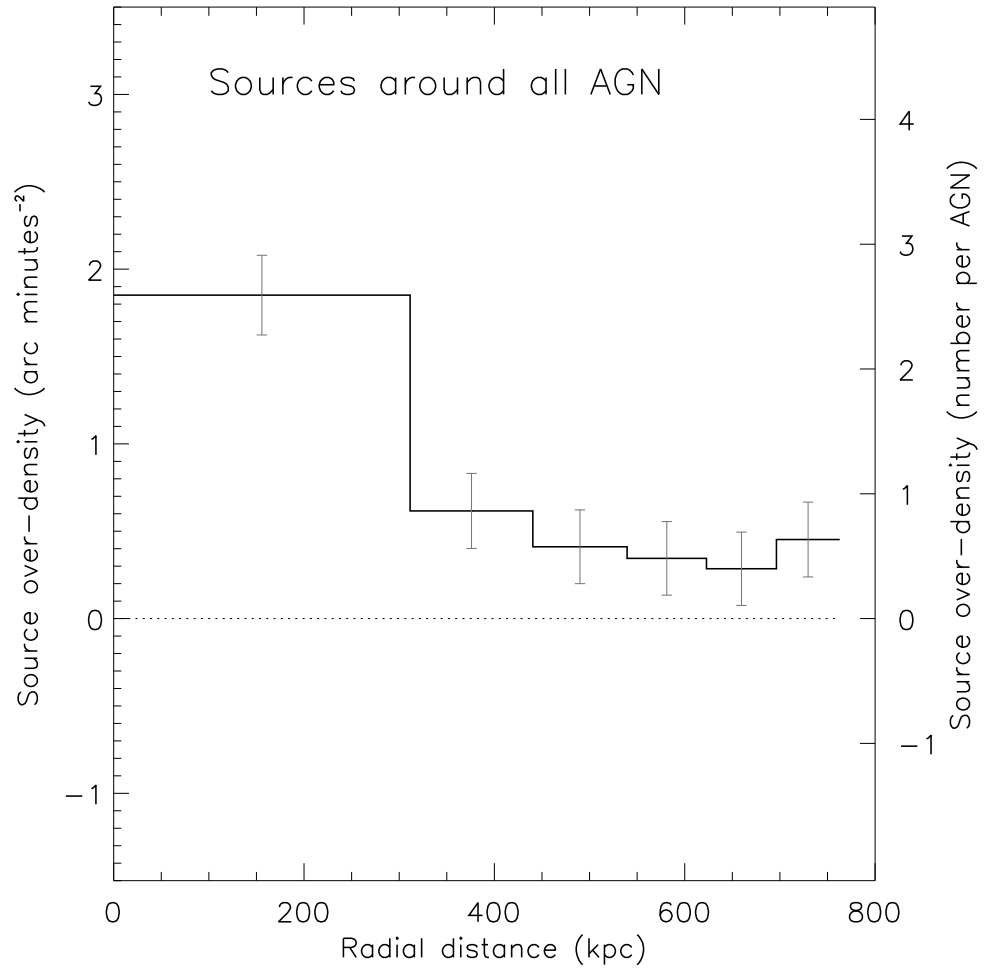

Figure 2.13: Histogram showing the average source over-density in all the AGN fields after they were corrected for completeness and the local background has been subtracted. The error bars are the result of adding in quadrature the errors on each field's over-density, which in turn are the result of adding the Poisson error on the source density measured in the AGN field to the Poisson error of the source density measured in its background field, both scaled by the mean completeness correction in each case. The dotted line simply shows the zero level. It should be noted that the radial distance is that projected on the sky converted to a distance at $z = 1$, and hence will be affected by the projection of the over-density.

Table 2.1: The over-density shown in Fig. 2.13 tabulated for each annulus and as an average for the outer annuli (*i.e.* excluding the first annulus which has a clear excess). The table shows the over-density (ΔN) both in number of sources and in units of arc min^{-2} as used in Fig. 2.13, the over-density error (err ΔN) again in both number and units of arc min^{-2} and the σ value which is the number of err ΔN that the over-density (ΔN) is above zero.

Annulus	ΔN	err ΔN	ΔN (arc min^{-2})	err ΔN (arc min^{-2})	σ
1	2.59	0.29	1.85	0.21	8.7
2	0.87	0.28	0.62	0.20	3.1
3	0.57	0.27	0.41	0.19	2.1
4	0.48	0.27	0.34	0.19	1.8
5	0.41	0.27	0.29	0.19	1.5
6	0.63	0.28	0.45	0.20	2.3
Outer annuli	2.94	0.63	0.42	0.09	4.7

error bars are the result of adding in quadrature the errors on each field's over-density, which in turn are the result of adding the Poisson error on the source density measured in the AGN field to the Poisson error of the source density measured in its background field both scaled by the mean completeness correction used in each case. It is obvious that there is an over-density in the AGN fields as a whole since all the annuli have a nominal value above the background level, but also an increase in this excess towards the position of the AGN especially the first annulus.

It thus appears that there are over-densities on two scales, one in the first annulus projected to be within 300 kpc (physical units) of the target AGNs and a larger over-density extending out to at least $\sim$ 700 kpc. The chosen annuli size came from a trade off between gaining a reasonable signal-to-noise in the first annulus whilst not watering down or throwing away too much spatial information about the over-density by including too large an

area. The radial search was thus repeated using annuli of varying size and it was found that the optimum size, in terms of signal to noise in the first annulus, is close to that adopted which have areas of 1.4 arc min^2. This exercise also showed that, even when smaller annuli were used, the central over-density still extended to ~ 300 kpc before dropping significantly towards the background level.

The significance of the over-density in each bin is simply the number of σ that the over-density is above zero. This is shown in Table 2.1 which shows the relevant values for each annulus. It can be seen that if we just consider the first annulus this is over-dense at the 8 σ level. In order to test whether the over-density in the outer annuli (i.e excluding the first annulus) is significant the counts in the outer annuli were added and the combined Poisson error was calculated. This gives an over-density of 0.42 ± 0.09 arc min^{-2} and a significance of 4.7 σ (see Table 2.1). Therefore, the outer bins are also significantly over-dense (out to at least 700 kpc).

It should be noted that these radial distances are those projected on the sky at the AGN's redshifts. Some of the galaxies making up the over-density will be further from the AGN in the line-of-sight direction and just projected as being at this distance on the sky. It is not really possible to account or correct for this as it depends on both the search radius used and the physical size of the over-densities as well as whether the AGN are in the centres of the over-densities. If the AGN were always in the centres of the over-densities then the projection of sources physically further away would make the projected source density appear to peak in the centre when in fact it could be constant but there is no way of distinguishing between this

scenario and the number of galaxies actually increasing towards the AGN, which is something else one would expect at the centre of a potential well. It is for this reason that the results here cannot be used to say anything about the shape of the over-densities around the AGN, rather just the number of galaxies within their environments.

The physical number of galaxies found on average in the first annulus, projected within ~ 300 kpc of the AGN is 2.6 ± 0.3 which is comparable to the number found in the outer annuli combined of 2.9 ± 0.6. Hence, in total there is an excess of 5.5 ± 0.7 excess galaxies projected within ~ 700 kpc of the AGN in the sample. This same projected pattern of a sharp peak in the central source over-density and then an extended flatter over-density was also reported by Best et al. (2003) for powerful radio galaxies at $z \sim 1.6$, and by Serber et al. (2006) for $z \leq 0.4$ SDSS quasars.

It is clear from this analysis, however, that there is a fair amount of field-to-field variation with individual AGN having source under/over-densities ranging from -9 to 13 arc min^{-2} projected within ~ 300 kpc (in the first annulus) corresponding to -13 to 18 galaxies compared to the background level. The Poisson errors associated with these numbers are also quite large which explains some scatter with the mean and maximum error being $\pm \sim 3$ and $\pm \sim 4$ sources arc min^{-2} corresponding to $\pm \sim 4$ and $\pm \sim 6$ galaxies per field respectively. This large range in under/over-densities that is not fully accounted for with the Poisson errors alone could be attributed to either actual changes in the environmental richness between fields, or to field-to-field changes in the foreground/background contamination that is affecting the measurements in addition to the Poisson errors quoted.

It should be noted that the results of this analysis are not being suggested as the environmental density for every AGN in the sample rather as the statistical mean of the population. It is likely that there are many factors likely to affect the environmental richness of a region other than the presence of an AGN and there are also likely to be many factors that affect an AGN's environment. However it is worth looking for statistical trends with large stacked samples such as this because if the samples are large enough then small effects that are negligible when looking at single objects become apparent and that tells us something about what effects the AGN are having on their environments and vice versa what effect the environments might be having on the AGN.

2.4.5 Over-Density versus AGN Type

To look for any differences between the environments of the AGN from different classifications the AGN sample is split into RQQ, RLQs and RG subsamples and a similar analysis is performed to that described in Section 2.4.4. The results of this analysis are shown in Fig. 2.14. On first inspection, the most notable difference between the subsets is the apparently larger over-density in the RLQ and RG samples when compared to the RQQ sample.

Using the same method as for the whole sample described in Section 2.4.4, the significance of the over-density in each annulus for each of these sub-samples is calculated. The main results are summarised in Table 2.2 which shows the over-densities and their significances and the same values in just the outer annuli (i.e excluding the first annulus). Focusing on the first

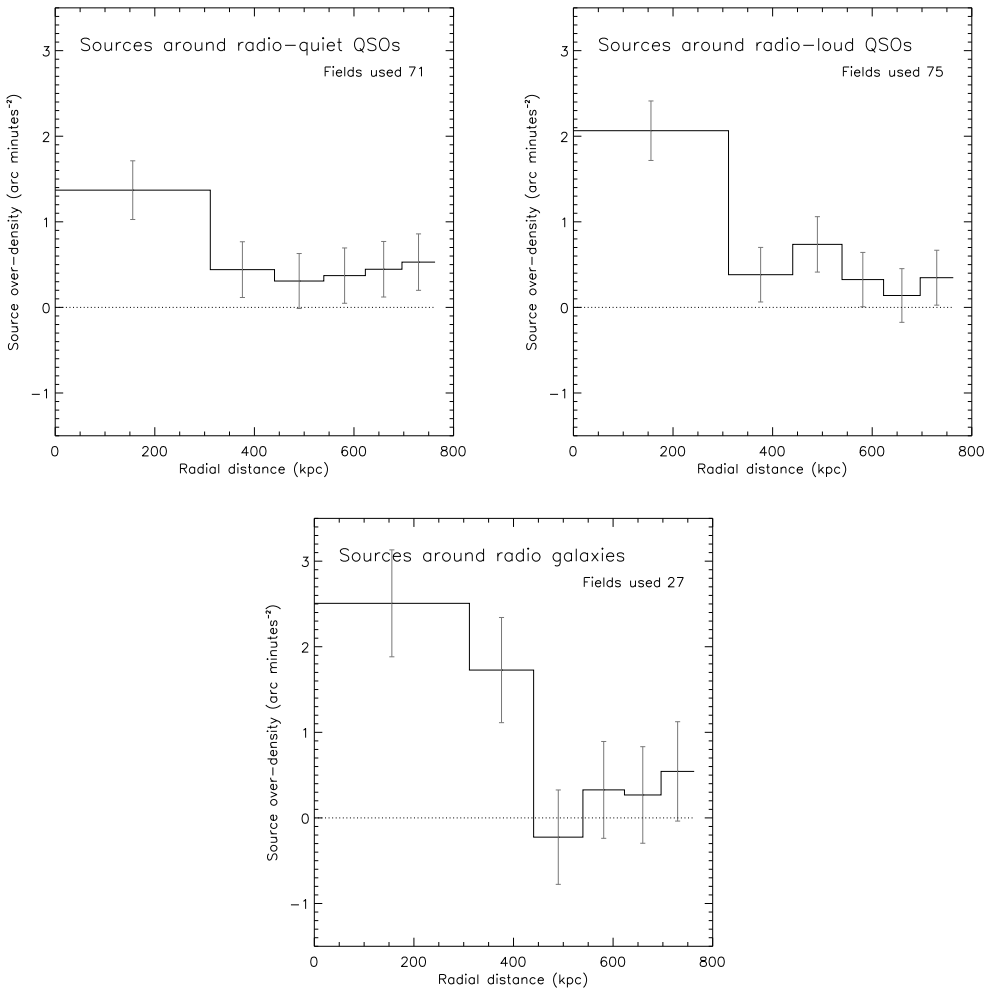

Figure 2.14: Histograms showing the average source over-density for the different AGN type sub-samples. The top left-hand panel shows the RQQs, the top right-hand panel shows the RLQs and the bottom panel shows the RGs. The error bars are the result of adding in quadrature the errors on each field's over-density, which in turn are the result of adding the Poisson error on the source density measured in the AGN field to the Poisson error of the source density measured in its background field both scaled by the mean completeness correction in each case. The dotted lines simply show the zero levels. It should be noted that the radial distance is that projected on the sky converted to a distance at $z = 1$, and hence will be affected by the projection of the over-density.

Table 2.2: The over-densities from Fig. 2.14 shown for the first three annuli and as an average for the outer bins (*i.e.* excluding first annulus). The table shows the over-density (ΔN) both in number and in units of arc min^{-2} and the σ value which is the number of ($\Delta Nerror0$) that the source density is above the blank field source density.

AGN type	Annulus	ΔN	ΔN (arc min^{-2})	σ
Radio galaxies	1	3.51	2.51	4.0
	2	2.42	1.73	2.8
	3	-0.31	-0.22	-0.4
	4	0.46	0.33	0.6
	5	0.38	0.27	0.5
	6	0.76	0.54	0.9
	Outer annuli	3.71	0.53	2.2
Radio-loud QSOs	1	2.88	2.06	5.9
	2	0.53	0.38	1.2
	3	1.04	0.74	2.3
	4	0.45	0.32	1.0
	5	0.20	0.14	0.4
	6	0.49	0.35	1.1
	Outer annuli	2.73	0.39	2.9
Radio-quiet QSOs	1	1.92	1.37	4.0
	2	0.62	0.44	1.4
	3	0.44	0.31	1.0
	4	0.52	0.37	1.2
	5	0.63	0.45	1.4
	6	0.74	0.53	1.6
	Outer annuli	2.94	0.42	3.1

annulus (projected within ~ 300 kpc), which in all cases appears to contain the sharp peak seen in the combined source density, over-densities are found of on average 3.51 ± 0.88, 2.88 ± 0.82 and 1.92 ± 0.48 galaxies which are significant at the 4.0σ, 5.9σ and 4.0σ level for the RGs, RLQs and RQQs respectively. The lower significance level for the RG sample probably just reflects the small sample size hence higher Poisson errors on similar signals. It is worth noting that in this subset the second annulus is also significant at the 2.8σ level, which if combined with the first annulus would give a more significant over-density. In the outer bins the over-densities are more similar with values of 3.71 ± 1.70, 2.73 ± 0.95 and 2.94 ± 0.96 galaxies for the RGs, RLQs and RQQs respectively.

To quantify the difference seen in the first annuli of the RLQs and RQQs a Mann-Whitney test is used, which is a non-parametric form of a t-test, and gives the probability that the null hypothesis that two data sets, in this case the source over-densities around these AGN, have the same means is true. This test returns a probability of 0.05, the null hypothesis is therefore rejected at the $\sim$ 95 per cent confidence level, suggesting that the RLQs occupy on average denser environments than the RQQs. Interestingly the RGs appear to have a larger central over-density than in the RLQ fields although more RG data would be needed to confirm this tentative result, as the Mann-Whitney test suggests the current data cannot be said to be significantly different.

In order to test whether this result is being caused by the presence of a few very over-dense fields which happen to fall into the radio-loud sample or vice-versa both the RLQ and RQQ samples have outliers $> 2\ \sigma$ from the

their means removed. The result of this is that the Mann-Whitney test gives an increased significance to the difference at a confidence level of > 98 per cent. Removing outliers that are more than 1 σ from the mean increases the confidence level further to the > 99 per cent suggesting that the central ~ 68 per cent of each sample are significantly different and the result is not caused by outliers alone, the outliers thus appear to be making the difference less pronounced. In fact if just the one QSO that has an environment that is more than 3 σ from the mean is removed the difference increases to the confidence level of > 96 per cent. This object (SDSS102005.99+0033308.5, see Fig. 2.15) is an RQQ and on inspection of the map there are two very bright objects in the centre one which may be the QSO and another $20''$ (150 kpc) away, the central bright source is ~ 2000 μJy and the other is ~ 1500 μJy. The entire central region also has an obvious excess of fainter objects, maybe this is a merging system or alternatively a background/foreground group or cluster. The same results are obtained whether the total mean and standard deviation of both samples combined are used to remove the outliers or each sample's mean and standard deviation. The distribution of the AGN's individual over-densities can be seen in Figs. 2.16, 2.18 or 2.19.

It therefore appears that all of three AGN samples have a significant over-density out to a projected distance of ~ 700 kpc with a sharp peak projected within ~ 300 kpc and the radio-loud objects on average have larger over-densities on the smaller of these scales (~ 300 kpc).

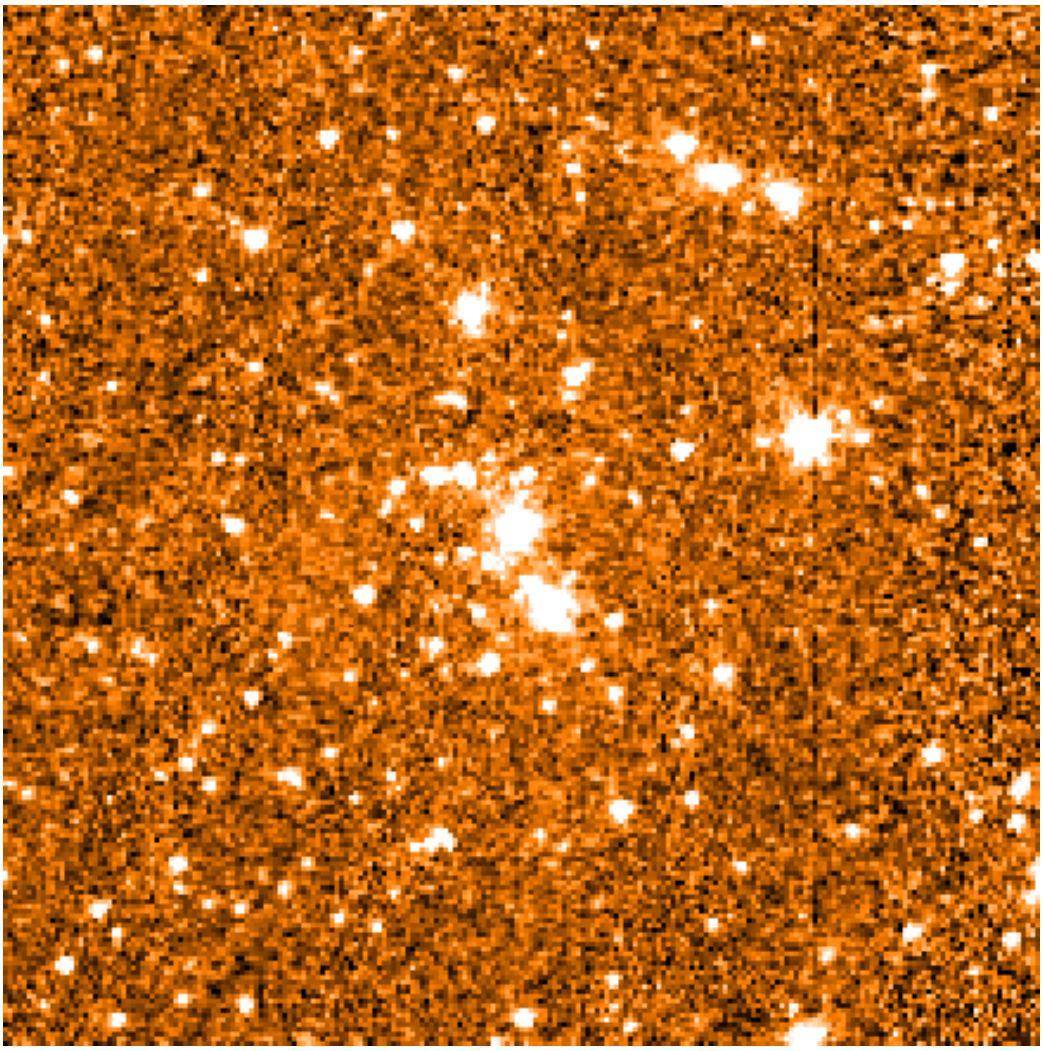

Figure 2.15: The 3.6 μm image of the field of RQQ SDSS102005.99+0033308.5, showing an especially high central source concentration including two very bright sources the central one of which may be the QSO. Possibly evidence of a merging group or cluster either associated with the QSO or in the foreground. The central bright source is ~ 2000 μJy and the other is ~ 1500 μJy.

2.4.6 Optical Luminosity vs. Environmental Density

In this Section the environmental density of the QSO part of the sample is examined as a function of the QSO's optical luminosity. This is unlikely to be able to explain the difference in the RLQ's and RQQ's environments because as shown in Section 2.2.1 and Fig. 2.4 these are found to be statistically indistinguishable. In Fig. 2.16 the result of plotting optical QSO luminosity versus environmental density is shown and it appears to be a pretty evenly filled parameter space, with no indication of a trend for larger over-densities around the most luminous QSOs. There is an apparent decrease in the dispersion of the environmental densities at the highest luminosities, however, this is most likely due to there being slightly fewer QSOs with the highest luminosities.

To search for a possible trend, a correlation analysis is performed using IRAF. This used three types of correlation analysis: the Spearman rank order test, the Generalised Kendall's τ test and the Cox proportional hazard test. In no case do the tests suggest we can reject the null hypothesis of no correlation, hence we find no evidence for a correlation of over-density with optical luminosity (see Table 2.3 for the numbers).

It therefore appears that there is not an increased environmental density around the most optically luminous QSOs in this sample which considering it spans five magnitudes in optical luminosity is surprising. This result has been found before at $z > 0.3$ by Smith et al. (1995) although most of the QSOs were below $M_v = -23$ and so could be considered Seyferts.

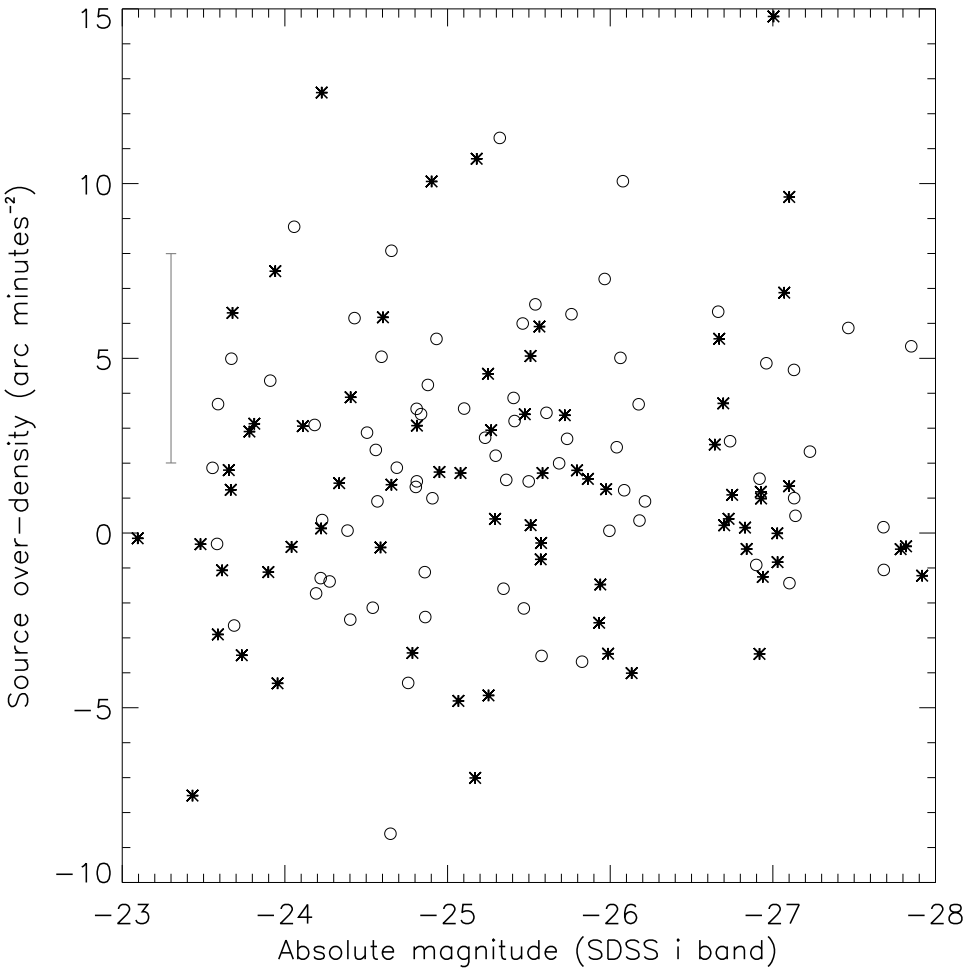

Figure 2.16: Source over-density projected within ∼300 kpc at $z \sim 1$ (first annulus of radial search) as a function of optical luminosity for the QSOs. The open circles show the RLQs and the stars show the RQQs. Also shown with an error bar is the mean size of the errors on the over-densities; this represents the Poisson error for each AGN field combined in quadrature with the Poisson error on the blank field level, that was subtracted, both scaled by their mean completeness correction.

2.4.7 Black Hole Mass versus Environmental Density

If the environments are not different based on luminosity then maybe this is due to accretion rates being the dominant factor in determining the optical luminosity rather than the underlying black hole masses which one would think intuitively should be linked to the environment in some way. In order to examine this and to try and understand the contrast between the fields of the radio-loud and radio-quiet objects, estimates of the black hole masses of the QSOs are used to look for any trend between the environments and the underlying black hole masses. It might for example, be expected that the greatest over-densities would be found around the AGN which are powered by the largest black holes and it is known RLQs are confined to objects with the largest black holes (e.g. Lacy et al. 2001; McLure & Jarvis 2004). If there is a difference in the RLQ and RQQ black hole mass distributions then this may account for the difference in their environments.

The black hole masses for the QSOs were estimated (in Jarvis et al. in prep) using the MgII line at 2800 Å from the SDSS spectroscopy as a virial estimator, a technique described by McLure & Jarvis (2002), and based on work by McLure & Dunlop (2001a). Note that black hole mass estimates are not possible in this way for the RGs because the broad-line region is obscured in these objects, but estimates are made for all of the QSOs.

To test whether the difference between the fields of the RLQs and RQQs might be related to intrinsically different black hole mass distributions, again a Mann-Whitney test was used. The test suggested that the mean black hole masses for the two samples are not significantly different and the null hy-

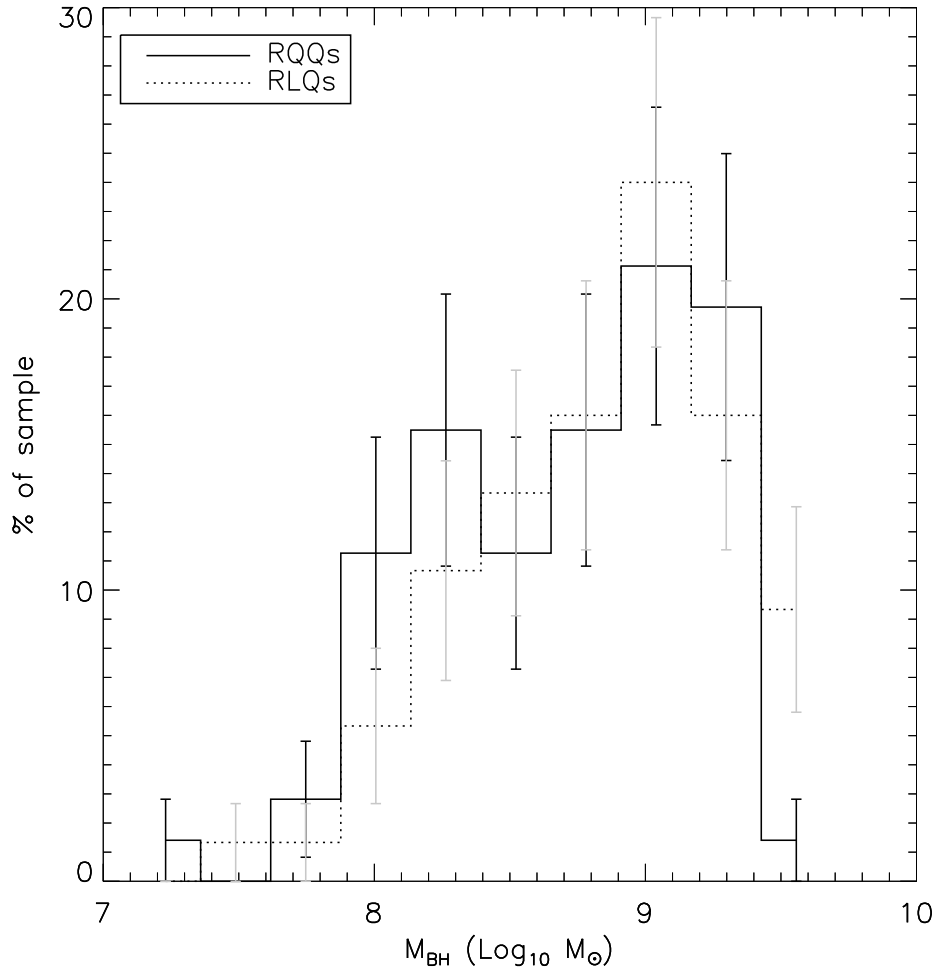

Figure 2.17: Histograms showing the distributions of RLQ (dotted line & grey error bars) and RQQ (solid line) black hole mass estimates made using the MgII line from the SDSS spectroscopy. Both histograms are normalised as a percentage of each sub-sample.

pothesis can not therefore be rejected. Moreover, a two-sample Kolmogorov-Smirnov (K-S) test again does not allow the null hypothesis that they are drawn from the same parent population to be rejected. It is worth stressing that this result does not contradict the previous works that find RLQs have, on average, more massive black holes but is rather a direct consequence of the manner in which the samples were initially selected. Specifically the fact they are identically matched in optical colours and luminosity (absolute SDSS-i band magnitude), which if everything else (i.e. accretion rates) were equal would be a proxy for black hole mass. The mean black hole masses are $\langle \log_{10}(M_{\rm BH}/\,{\rm M}_{\odot})\rangle = 8.87 \pm 0.06$ for the RLQs and $\langle \log_{10}(M_{\rm BH}/\,{\rm M}_{\odot})\rangle = 8.81 \pm 0.06$ for the RQQ so the means of the two samples are consistent and within the 1 σ errors of each other. The distribution of black hole masses are shown for both samples in Fig. 2.17.

Over-density in the first annuli versus black hole mass for every QSO, regardless of classification, is shown in the left panel of Fig. 2.18. The results of conducting the correlation analysis for black hole mass versus environment is shown in Table 2.3 which shows that the null hypothesis of no correlation cannot be rejected based on any of the tests used.

A possible source of uncertainty in the black hole masses of RQQs and RLQs could be their orientations with respect to the observer. As shown by Jarvis & McLure (2002) and Jarvis & McLure (2006) one would expect that sources with bright core radio emission would be preferentially aligned pole-on to the observer. Coupled with a disc-like broad-line region, such a bias would result in lower derived black hole masses for the RLQs relative to the RQQs given the same optical selection. However, the initial selection, based

on low-frequency radio emission using the WENSS data at 325 MHz, means that beaming effects are minimised as the radio emission at low frequencies is dominated by the extended, optically thin, lobe emission. Therefore, although it cannot be ruled out completely that a link between the environmental density and black hole mass for the sample exists, it would seem unlikely.

2.4.8 Radio Luminosity versus Environmental Density

Having upper limits for the RQQ radio powers (see Section 2.2.1) allows the investigation of the environmental densities of all the AGN as a function of radio luminosity (see Fig. 2.19). This clearly shows the range of over/under-densities discussed in Section 2.4.4. It is also worth noting the size of the errors on the over-density in these figures, as shown by the mean error bar (± 3 arc min^{-2}). Hence one would expect large scatter on any correlation present in the data. It is also noticeable that compared to the means as quoted in Tables 2.1 and 2.2 the over-densities appear to be scattered further from the mean in the positive direction. This may suggest that some of the scatter is coming from foreground contamination as this would be more likely to increase the over-density than decrease it as the background measurement is from a larger area and so foreground structures will be less of an issue.

At face value, the data in Fig. 2.19 are not that obviously correlated, however there is a total lack of any high radio luminosity AGN with luminosities of $\log_{10}(L_{325}/\mathrm{W\,Hz^{-1}\,sr^{-1}}) > 26.8$ with under-densities. In fact only looking at AGN with $\log_{10}(L_{325}/\mathrm{W\,Hz^{-1}\,sr^{-1}}) > 26$ there does appear to be

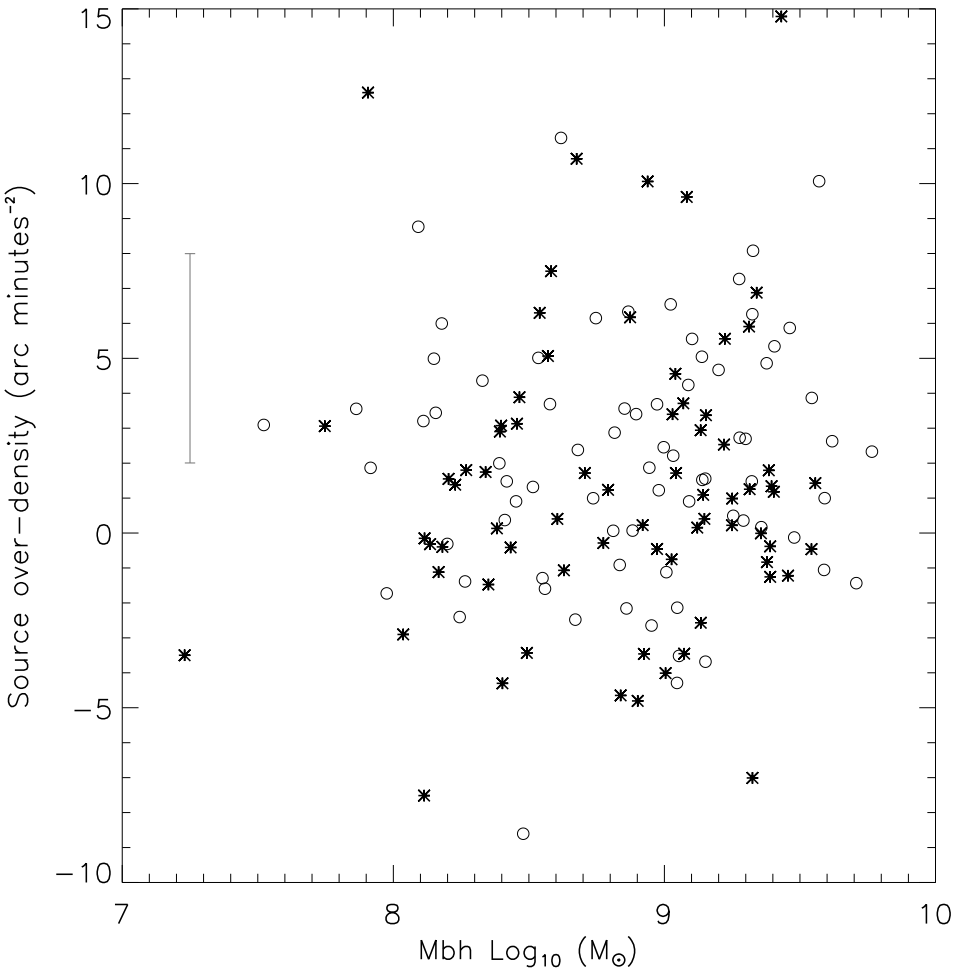

Figure 2.18: Source over-density projected within ∼300 kpc at $z \sim 1$ (first annulus of radial search) as a function of black hole mass for the QSOs. The open circles show the RLQs and the stars show the RQQs. Also shown with an error bar is the mean size of the errors on the over-densities; this represents the Poisson error for each AGN field combined in quadrature with the Poisson error on the blank field level, that was subtracted, both scaled by their mean completeness correction.

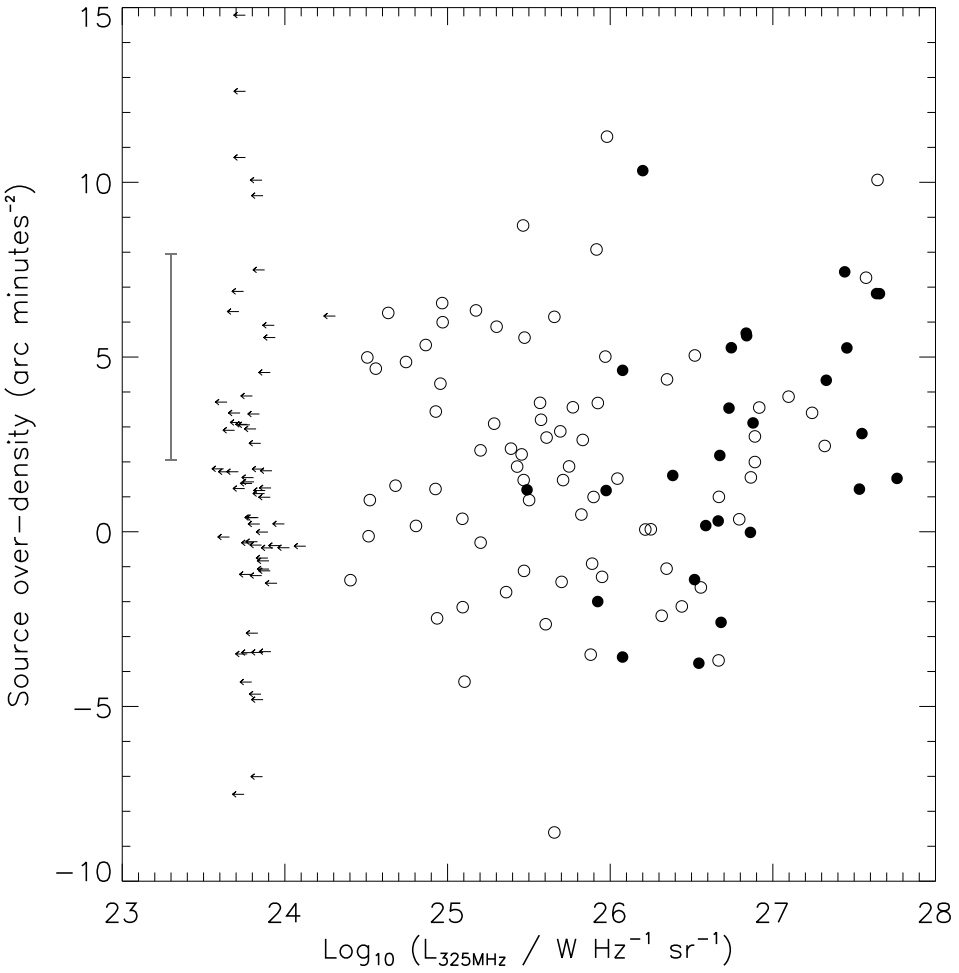

Figure 2.19: Source over-density projected within ∼300 kpc at z ∼1 (first annulus of radial search) as a function of radio luminosity at 325 MHz for all AGN. The open circles show the RLQs, the filled circles the RGs and the upper limits are for the RQQs. Also shown with an error bar is the mean size of the errors on the over-densities, these represent the Poisson error for each AGN field combined in quadrature with the Poisson error on its blank field level, that was subtracted, both scaled by their mean completeness correction.

Table 2.3: Correlation analysis on the data from Figs. 2.16, 2.18 and 2.19, *i.e.* source over-density within ∼300 kpc at z ∼1 versus black hole mass for the QSOs. As well as source over-density versus radio luminosity for all AGN, AGN with $L_{radio} > 26$, AGN with $L_{radio} < 26$, RLQs with $L_{radio} < 26$, all the RLQs and for all the RGs . All radio luminosities are in units of $\log_{10}(L_{325}/\mathrm{W\,Hz^{-1}\,sr^{-1}})$. The three tests used are Spearman's rank order test, a generalised Kendall's τ test and the Cox Proportional Hazard test, in each case the Value column shows either Spearman's ρ, Kendall's τ or a global χ^2 value for the Cox Hazard test. The significance level shown is the probability that the null hypothesis exists (*i.e.* no correlation), the final column states whether the null hypothesis is rejected. Survival analysis is used where necessary to include the RQQs upper limits in the radio luminosity analysis. In cases where the sample size is less than 30 the Spearman's rank order test is not used as it requires $N > 30$ to be accurate.

Over-density versus	Test	Value	Significance	Correlation
Optical luminosity for all QSOs	Spearman's rank	-0.039	0.638	No
	Kendall's τ	-0.018	0.736	No
	Cox Hazard	0.072	0.788	No
M_{BH} for all QSOs	Spearman's rank	0.045	0.416	No
	Kendall's τ	0.068	0.413	No
	Cox Hazard	0.684	0.408	No
L_{radio} for all AGN	Spearman's rank	0.149	0.054	∼Yes
	Kendall's τ	0.201	0.047	Yes
	Cox Hazard	1.607	0.205	No
L_{radio} for AGN with ($L_{radio} > 26$)	Spearman's rank	0.488	0.001	Yes
	Kendall's τ	0.733	< 0.001	Yes
	Cox Hazard	11.791	0.001	Yes
L_{radio} for AGN with ($L_{radio} < 26$)	Spearman's rank	0.503	0.478	No
	Kendall's τ	0.102	0.262	No
	Cox Hazard	0.503	0.478	No
L_{radio} for RLQs with ($L_{radio} > 26$)	Kendall's τ	0.943	0.003	Yes
	Cox Hazard	11.736	0.001	Yes
L_{radio} for all RLQs	Spearman's rank	-0.090	0.938	No
	Kendall's τ	-0.004	0.938	No
	Cox Hazard	-1.778	0.1823	No
L_{radio} for all RGs	Kendall's τ	0.644	0.0185	Yes
	Cox Hazard	4.083	0.043	Yes
L_{radio} for all QSOs	Spearman's rank	0.112	0.188	No
	Kendall's τ	0.136	0.208	No
	Cox Hazard	0.684	0.408	No

a good correlation.

The censored data (e.g. the RQQ upper limits) require survival analysis to be used for the correlation analysis. Therefore, again IRAF's Spearman rank order test, Generalised Kendall's τ test and the Cox proportional hazard model are used. All three tests can handle one type of limit in the dependent variable, in this case upper limits in the radio luminosity.

The results of the correlation analysis on the whole sample are shown in Table 2.3. This shows that with the exception of the Cox proportional hazard model the tests give evidence for a correlation between radio luminosity and over-density as the probability that a correlation does not exist (*i.e.* the probability that the null hypothesis is true) is at the ~ 5 per cent level. However, if the analysis is restricted to $\log_{10}(L_{325}/\mathrm{W\,Hz^{-1}\,sr^{-1}}) > 26$, which ensures that all of the sources lie well within the FRII régime then the correlation, as it appears to the eye, becomes much more significant with a very low probability that the null hypothesis is true (*i.e.* no correlation) at the < 0.1 per cent level.

Intriguingly, in the high radio luminosity range the RLQs and RGs appear to show a fairly tight trend to the eye of increasing source over-density with radio luminosity, and this is also shown with the correlation analysis. The improvement in the correlation for high radio luminosity AGN ($\log_{10}(L_{325}/\mathrm{W\,Hz^{-1}\,sr^{-1}}) > 26$) is interesting as there generally appears to be much less dispersion on the over-densities for these objects, especially when compared with the RQQs. The fact that the two samples agree so well would of course be expected in the unified scheme (Barthel 1989). If the same correlation analysis is conducted on the sample of AGN excluding the

high radio luminosity objects ($\log_{10}(L_{325}/\mathrm{W\,Hz^{-1}\,sr^{-1}}) < 26$) the correlation observed for the whole sample disappears, see Table 2.3. This suggests that the evidence for a correlation was largely created by the inclusion of the high radio luminosity objects.

A potential concern is that the RGs are not selected in the same way as the RLQs, and maybe they are causing the correlation that is observed. To test for this scenario the correlation analysis was run on just the RGs and the high radio luminosity RLQs ($\log_{10}(L_{325}/\mathrm{W\,Hz^{-1}\,sr^{-1}}) > 26$), see Table 2.3. This shows that there is significant evidence for correlation at a similar confidence level to all AGN in this range when just the RLQs are looked at. In addition when just looking at the RGs significant evidence for a correlation is found but with a slight increase in the probability that one does not exist by 1 per cent, see Table 2.3. These results suggest that it is not just the RGs causing the observed trend and rather is a combination of all the AGN in this range of high radio luminosities. The analysis is also conducted on all the QSOs and all the RLQs to check, in both cases no evidence is found for a correlation, see Table 2.3.

A possible solution that springs to mind when looking at Fig. 2.19 is that there are two populations of objects with a divide in radio luminosity at around ($\log_{10}$ (L_{325} / $\mathrm{W\,Hz^{-1}}$ $\mathrm{sr^{-1}}$) > 26). The low radio luminosity objects appear to occupy a much wider spread of environmental densities compared with the higher radio luminosity objects which not only occupy a narrower range of environments but also shown a trend of increasing environmental richness with radio luminosity. Indeed in recent work by Donoso et al. (2010) find that the environmental densities of RLQs and RGs match only

for radio luminosities of $\log_{10}(L_{325}/\mathrm{W\,Hz^{-1}\,sr^{-1}}) \gtrsim 25.4$ (when converted into the units used here). Their interpretation is that the unified scheme for radio-loud QSOs and radio galaxies might only be valid for high radio luminosities. Donoso et al. (2010) also report a similar trend to that found here, of increasing environmental density with radio luminosity for RLQs, in contrast though they do not find a difference between RLQs and RQQs.

2.5 Spatial Clustering Amplitude (B_{gq})

A more sophisticated method of measuring over-densities of galaxies around a point or a set of points in the Universe is to use the spatial clustering amplitude (B_{gg}). This technique was first used and fully described by Longair & Seldner (1979), who used it to measure the clustering of galaxies around extragalactic radio sources. The basis of the spatial clustering amplitude is to take the angular clustering amplitude (A_{gg}), i.e the degree of over-density as projected on the sky, and normalise this using a suitable luminosity function to allow over-densities around objects at different redshifts measured with different flux limited surveys to be easily compared. This technique can be used to measure the degree of clustering around any point in the universe. It can therefore, in this case be used to measure the clustering around the AGN in the sample, in which case A_{gq} and B_{gq} are defined to be the angular and spatial clustering amplitudes of galaxies around AGN.

2.5.1 Technical Description

Angular Clustering Amplitude (A_{gq})

To measure the the angular clustering about a point or set of points in the Universe, in a given survey, counts of galaxies in increasing apertures around the point's position on the sky down to the survey's flux limit are made. The number of galaxies found at an angular separation of θ can then be described by the angular correlation function (equation 2.1, see Seldner & Peebles 1978 for a full description).

$$N(\theta)d\Omega = N_{density}[1 + w(\theta)]d\Omega \tag{2.1}$$

In this function $N(\theta)d\Omega$ is the number of galaxies within the solid angle $d\Omega$ with an angular separation from the point's position of θ. $N_{density}$ is the surface density of galaxies expected per steradian, *i.e.* the background level, determined from a blank field or from averaging the whole survey. $w(\theta)$ describes the number of galaxies found as a fraction of the background level and as a function of θ; if galaxies were not clustered at all $w(\theta)$ would be zero.

It has been found however that galaxies do cluster and as such $w(\theta)$ is found to have the functional form shown in equation 2.2.

$$w(\theta) = A_{gq}\theta^{1-\gamma} \tag{2.2}$$

The γ term in this equation describes how the density of galaxies changes with angular distance from the point position on the sky. The A_{gq} term is

the angular clustering amplitude and describes the strength of the clustering compared to the background level of galaxies, essentially how rich the environment around the central point is as projected on the sky. If the environment is less rich than the background A_{gq} will be negative and if it is richer it will be positive. In general galaxies are found to be clustered such that, on average, $\gamma = 1.77$ (Groth & Peebles 1977), where as in local clusters of galaxies $\gamma = 2.00$ is found to be more appropriate (Bahcall et al., 2003).

If θ is much less than one radian then it is possible to calculate the clustering amplitude A_{gq} from the data directly using equation 2.3 (McLure & Dunlop 2001b).

$$A_{gq} = \left[\frac{N_\theta}{N_{background}} - 1\right] \left(\frac{3-\gamma}{2}\right) \theta^{\gamma-1} \tag{2.3}$$

In which N_θ is the number of galaxies within the counting radius of θ and $N_{background}$ is the number of galaxies that would be expected inside the counting radius based upon the surface density from averaging the whole survey or from a blank field $N_{density}$.

Spatial Clustering Amplitude (B_{gq})

To allow for comparison of over-densities at different redshifts obtained using different flux limited surveys, this angular clustering amplitude must be converted to a spatial clustering amplitude. The spatial correlation function has the form shown in equation 2.4.

$$N(r)\delta V = \rho_g[1 + \epsilon(r)]\delta V \tag{2.4}$$

where

$$\epsilon(r) = B_{gq}(r)^{-\gamma} \tag{2.5}$$

The B_{gq} term in equation 2.5 is the spatial clustering amplitude which is the environmental richness around the points position in space corrected by taking account of how far down the luminosity function the survey reaches at the point's redshift. Like A_{gq}, B_{gq} will be positive for over-densities and negative for under-densities.

Longair & Seldner (1979) showed that for spherically symmetric over-densities the angular clustering amplitude can be converted to the spatial equivalent by equation 2.6.

$$B_{gq} = \frac{A_{gq} N_{density}}{I_\gamma \phi(z)} \left(\frac{D_A}{1+z} \right)^{\gamma-3} \tag{2.6}$$

In which I_γ is a constant, taking the value of 3.78 for $\gamma = 1.77$ (Groth & Peebles 1977), D_A is the angular diameter distance to the target and $\phi(z)$ is the adopted luminosity function integrated at the target's redshift.

2.5.2 Luminosity Function

The reliability of the B_{gq} calculation relies heavily on the accuracy of the chosen luminosity function and that the data are compatible with it. The luminosity function of Cirasuolo et al. (2010) is used here which is a K-band luminosity function that takes into account evolution of the galaxy population out to $z{\sim}4$. A K-band luminosity function is chosen as at $z \sim 1$ the 3.6 μm data will be sampling light emitted at 1.8 μm which is just short-

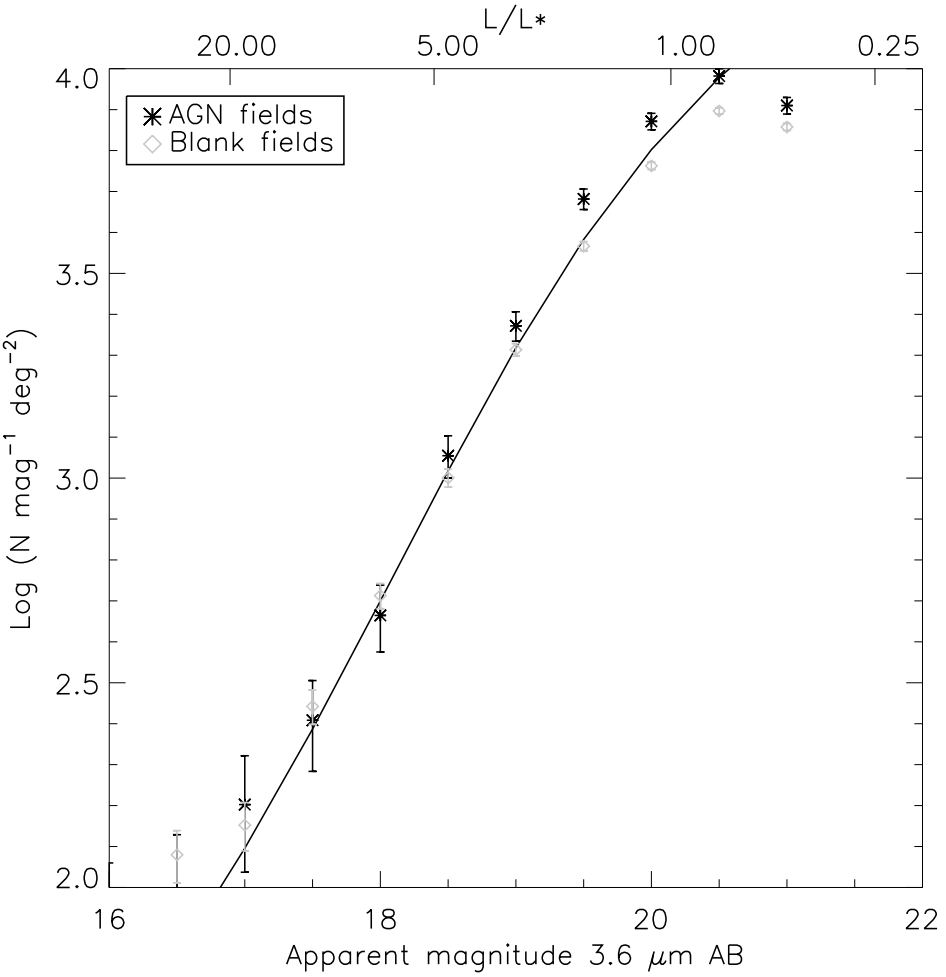

Figure 2.20: The number counts from the blank fields (diamonds) and first annulus of the AGN fields (stars) plotted in bins of 0.5 magnitudes; both counts have the calculated completeness correction applied. The line shows the predictions from the adopted luminosity function of Cirasuolo et al. (2010). The top y-axis shows how these apparent magnitudes compare to L* at $z \sim 1$. Error bars show the Poisson errors on the number counts in both cases.

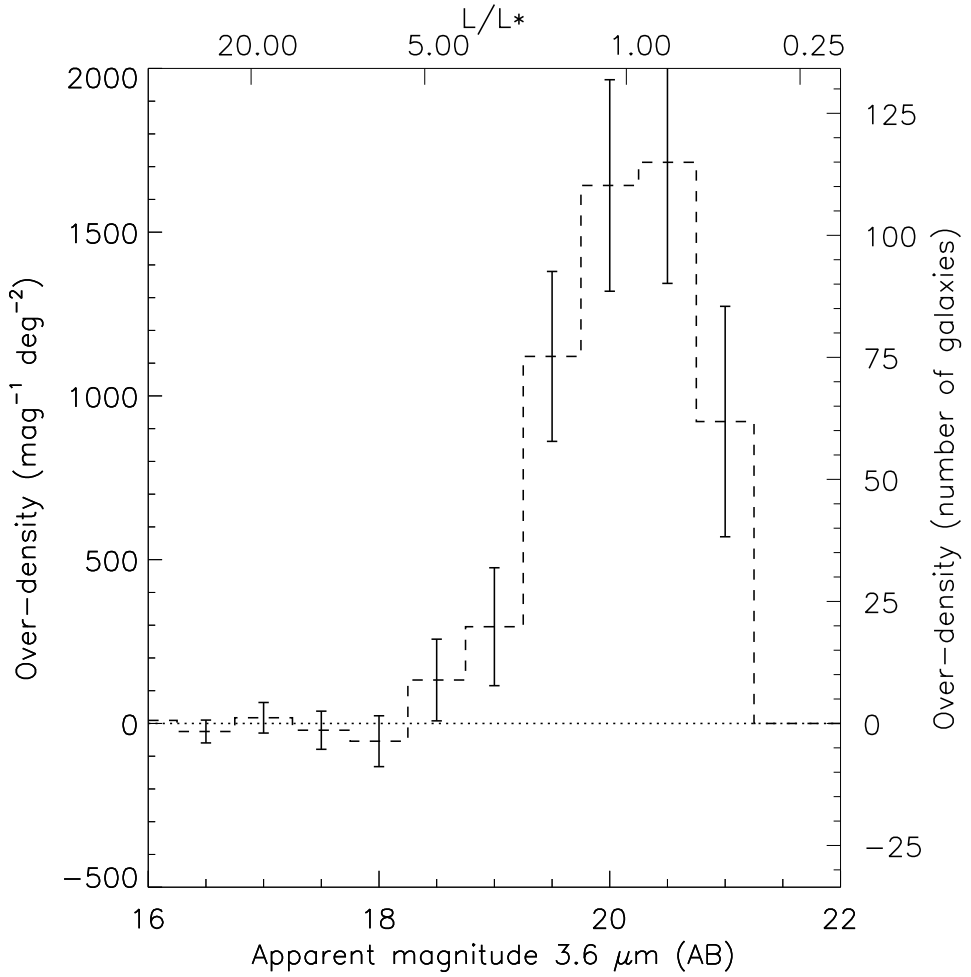

Figure 2.21: The result of subtracting the number counts of sources in the blank fields from those in the AGN fields, showing where the excess of sources found around the AGN lie in terms of their apparent magnitude. The top axis shows how these apparent magnitudes relate to the luminosity of an L* galaxy at $z \sim 1$, showing that the over-density corresponds to an excess of 0.3 to 4 L* galaxies at $z \sim 1$. Error bars show the Poisson errors on the number counts in AGN and blank fields added in quadrature; all numbers have completeness corrections applied.

ward of the rest-frame K-band meaning only a small K correction at the redshift of interest is required. This is probably also the best constrained luminosity function at the near-infrared wavelengths available at these high redshifts. The agreement between the luminosity function and the data can be tested using the blank field number counts, which should for the B_{gq} analysis to be valid, be given by integrating under the luminosity function down to the faintest galaxy detectable.

The Cirasuolo et al. (2010) luminosity function is a Schecter function of the form shown in equation 2.7.

$$\phi(M) = 0.4ln(10)\phi_0 10^{-0.4(M_K - M_k^*)(\alpha+1)} exp(-10^{0.4(M_K - M_k^*)}) \tag{2.7}$$

In which both M_k^*, the characteristic luminosity, and ϕ_0, the number density of M_k^* galaxies, are functions of z and so take into account evolution out to $z{\sim}4$. Comparing this function to the data involves integrating down to the the faintest galaxy detectable in the 3.6 μm data in a series of redshift bins out to $z{\sim}4$. Each redshift bin requires a different combination of K and colour correction to convert absolute magnitudes in the rest frame K-band into observed 3.6 μm apparent magnitudes. In the integration redshift bins of 0.1 and bins of absolute magnitude of 0.5 mags were adopted. The K and colour corrections are taken to be those for the middle of the bins and these are calculated by using a Bruzual & Charlot (2003) elliptical galaxy template and the HYPER software package (Bolzonella et al., 2000).

The resulting prediction for the observed $3.6\mu m$ number counts are compared to those from the blank and AGN fields in Fig. 2.20. It can be seen

that the blank fields agree well with the luminosity function in the apparent magnitude range between ~ 17 and ~ 19. Sources brighter than 17 are firstly rare, less than 100 per square degree, and so there are not enough in the sample to accurately compare to the luminosity function, but also are likely to be dominated by local galaxies and possibly stars which the luminosity function is not designed to represent. At the faint end the *Spitzer* data start to become incomplete at apparent magnitudes fainter than ~ 19, even with the completeness correction applied, and so the number counts begin to fall below the predictions. The AGN fields show a clear excess of sources compared to both the blank fields and the luminosity function for apparent magnitudes fainter than ~ 19.

The result of subtracting the number counts in the blank fields from those in the AGN fields is shown in Fig. 2.21; this is useful as it allows the over-density to be split in luminosity space. It can be seen that the excess corresponds to galaxies that are between $\sim$ 0.3 and $\sim$ 4 L* at $z\sim$1 and is therefore consistent with the interpretation of this over-density as being associated with the AGN in the sample.

2.5.3 Spatial Clustering Amplitude Results

Using the spatial clustering amplitude gives the same results as presented in Section 2.4 using the number densities alone. Fig. 2.22 shows the distribution of B_{gq} for the three AGN sub-samples. As with the number densities there is a similarly large scatter of the B_{gq} values of individual AGN and so it is probably more informative to look at the mean values. As in the number

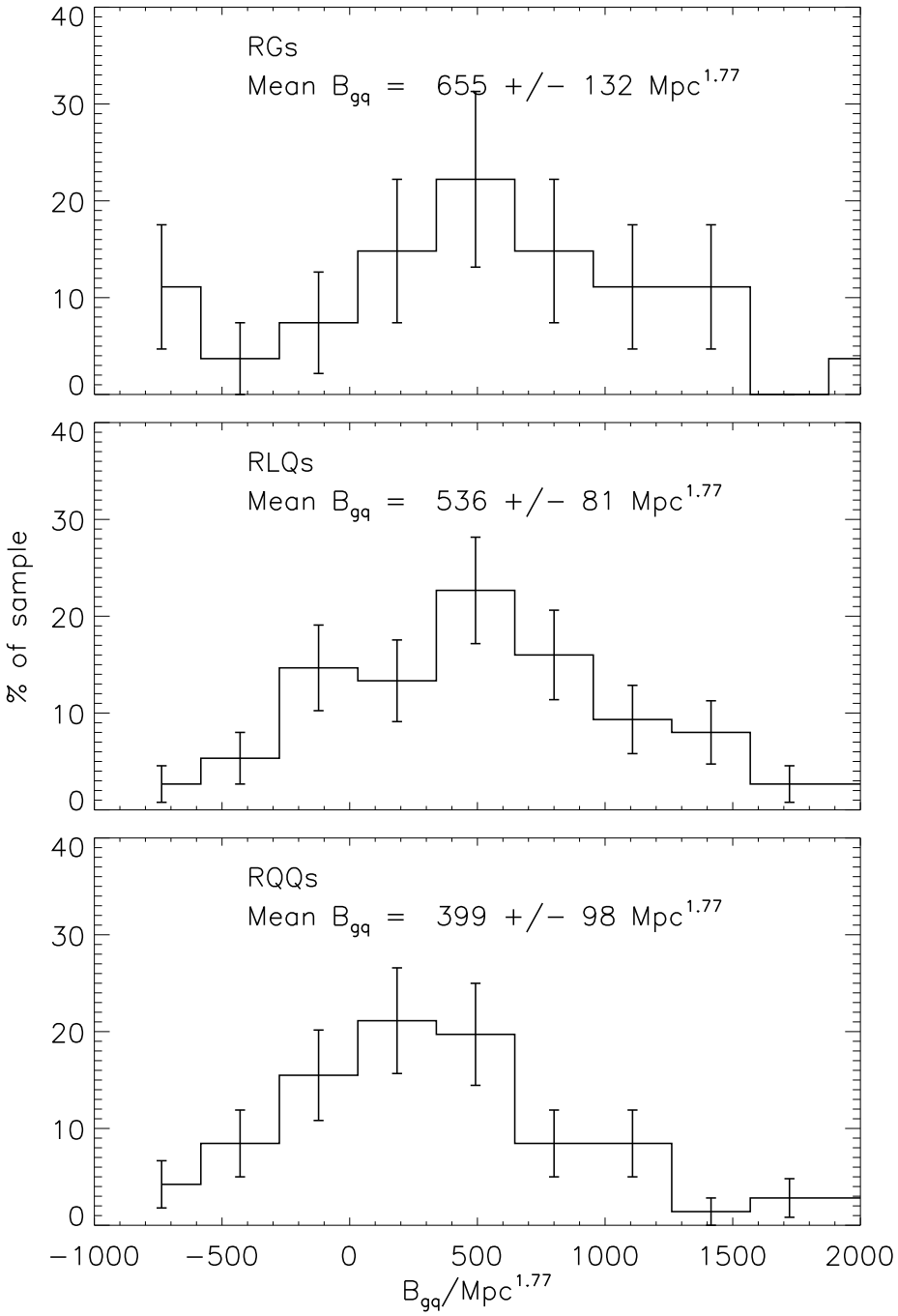

Figure 2.22: Histograms showing the distributions of B_{gq} for all three types of AGN as a percentage of the total number in each sub-sample. The top panel is for the RGs, the middle for the RLQs and the bottom for the RQQs. Also shown is the mean B_{gq} values for each subset. Which shows the same trend as with the number density analysis in Fig. 2.14. Error bars show the Poisson errors on the number counts in each bin.

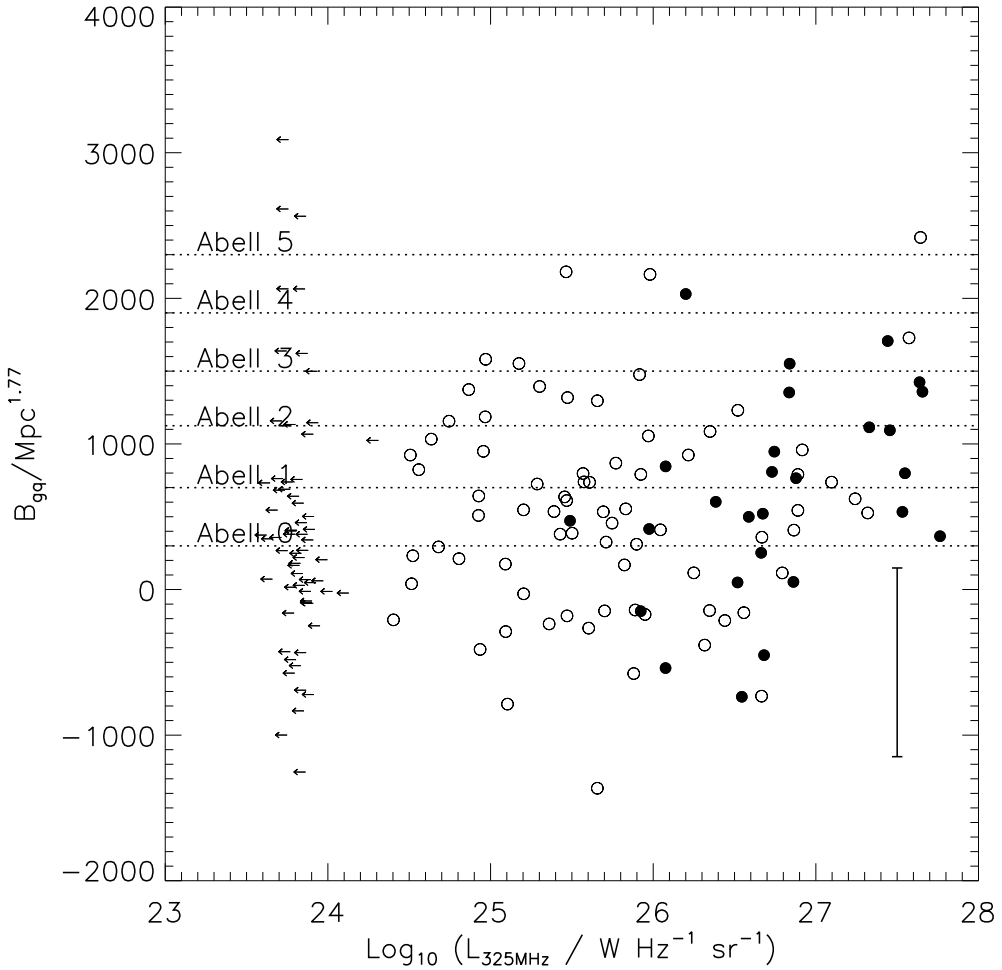

Figure 2.23: B_{gq} versus radio luminosity for all AGN. The RGs are shown by filled symbols, the RLQs by open symbols and the RQQs by their upper radio luminosity limits. The same trend is apparent that is seen just with the number density analysis alone in the right-hand panel of Fig. 2.19. Also shown is how this sample compares to Abell classification. An error bar which represents the mean B_{gq} error on all the data points is also shown.

density analysis the RGs have the highest mean B_{gq} value of 655 ± 132 Mpc$^{1.77}$ followed by the RLQs with 536 ± 81 Mpc$^{1.77}$ and then the RQQs which have a mean value of 399 ± 98 Mpc$^{1.77}$. The difference between the RLQs and RQQs distributions is again significant at the > 96 per cent confidence level using a Mann-Whitney test. Note also note that Fig. 2.23 which shows B_{gq} versus radio luminosity for the whole sample is very similar to Fig. 2.19. As with number density alone a correlation analysis suggests a positive correlation of increasing source density with radio luminosity which improves for the highest radio powers.

Comparing the mean B_{gq} values determined here with those from McLure & Dunlop (2001b) for very similar well matched samples, albeit smaller and at lower redshift, shows that the results found here agree favourably. The values from McLure & Dunlop (2001b) are as follows $B_{gq} = 575 \pm 165$ Mpc$^{1.77}$, 267 ± 51 Mpc$^{1.77}$, 326 ± 94 Mpc$^{1.77}$ for the RGs, RLQs and RQQs respectively. Hence, the B_{gq} numbers for RGs and RQQs are perfectly consistent with those of McLure & Dunlop (2001b). Most of the earlier authors however, find that RQQs typically occupy environments akin to field galaxies with a $B_{gq} \sim 60$. This was suggested by McLure & Dunlop (2001b) as possibly being due to including QSOs in the sample that had M_v fainter than 23 mag and were thus better described as Seyferts which may have more field like environments (De Robertis et al., 1998). This may explain some of contrast found between RLQs and RQQs environments in the works with lower luminosity QSOs but it cannot explain the difference found in this chapter as all the QSOs in this sample have M_i brighter then 23.

The only disagreement between this work and that of McLure & Dunlop

(2001b) is for the RLQs which here are found, on average, to have a B_{gq} a factor of two higher. Similarly lower B_{gq} values are found for RLQs by Ellingson et al. (1991), Wold et al. (2001) and with a subset of those from McLure & Dunlop (2001b) by Fisher et al. (1996). The sample sizes in all these works were small and so maybe this explains the difference or simply that they are at lower redshift ($z < 0.6$). However, the key difference for all these samples may in fact be that they are of lower radio power $\log_{10}$ (L_{325} / W Hz^{-1} sr^{-1}) $<$ 25.9 (converting to 325 MHz using a spectral index of 0.7) than the RLQs in this work. If a difference between RLQs and RQQs environments only becomes pronounced when the highest radio power RLQs ($\log_{10}$ (L_{325} / W Hz^{-1} sr^{-1}) $>$ 26.0) are included, as Section 2.4.8 suggests, then this explains why McLure & Dunlop (2001b) and Wold et al. (2001) find no evidence for a difference or for a correlation with radio power. This may in fact explain why some authors find a difference between RLQ and RQQ environments while others do not and could be considered a selection effect due to the rarity of the highest radio power AGN at low redshift making them less likely to be included in samples.

Additionally although McLure & Dunlop (2001b) find no evidence for a correlation with radio power in their RLQ B_{gq} data they do suggest there may be tentative evidence for one in their small RG sample. Their RG and RLQ samples are matched in radio power but this is at high frequency (5 GHz) and so the RLQ radio powers may be affected by beaming, in this case they may actually be of lower radio power and hence do not correlate in the same way that the low radio power RLQs presented in this work do not either. Conversely RLQs and RGs in this sample are matched using

their low frequency radio emission at 325 MHz and so should be orientation independent.

The especially interesting feature that B_{gq} analysis allows, which is not possible with just number density, is to compare over-densities to those at other redshifts and hence common measures of cluster richness used in the local universe such as Abell classes (Abell, 1958). To do this the same calibration of B_{gq} to Abell class is used as was used by McLure & Dunlop (2001b), bearing in mind the large uncertainty in this conversion. In this calibration Abell class 0 has a B_{gq} of 300 Mpc$^{1.77}$ and there is 400 Mpc$^{1.77}$ separating the different classes. How the AGN environments in this sample compare to this measure of local cluster richness is shown in Fig. 2.23. What is clear from this figure is that although these AGN reside in over-densities they are not in especially dense environments. On average they are typically in Abell class 0/1 or lower density groups or clusters, with perhaps those with the highest density environments in richer Abell class groups or clusters but these might just be scattered by the large uncertainties involved. Looking at the sub-samples it can be seen that the RQQs are found, on average, in environments comparable to or less rich than Abell class 0 clusters where as the RLQs and RGs are on average in environments similar to Abell classes 0/1. Which again is similar to previous findings in the literature (Yee & Green, 1984, 1987; Ellingson et al., 1991). There is of course significant dispersion on these numbers for individual AGN and this is understandable looking at the size of just the Poisson errors which are by no means the only uncertainty in the calculation of B_{gq}.

2.6 Discussion

The stacking analysis on the environments of a large sample of AGN presented in this chapter indicates that, on average, AGN at $z \sim 1$ have 2 to 3 (0.3-4 L^*) galaxies containing a substantial evolved stellar population projected within ~ 300 kpc. There is also a significant over-density extending out to at least a projected distance of 700 kpc which combined represents an excess of ~ 5 evolved (0.3-4 L^*) galaxies per AGN on average.

The analysis also finds evidence that the radio emission we observe from AGN is in some way related to the galaxy density in its environment. Firstly there is evidence that the RLQs and RGs occupy more dense environments than the RQQs. More specifically, however, if AGN classification is ignored and over-density is looked at as a function of radio luminosity (Fig. 2.19 and Fig. 2.23) there is evidence for a positive correlation between the two at the 2σ level (Table 2.3). This is, however, shown to result from a more significant (3σ level) correlation for radio-loud AGN with radio luminosities $\log_{10}(L_{325}/\mathrm{W\,Hz^{-1}\,sr^{-1}}) > 26$. This correlation is shown to remain significant when the RG and RLQ sub-samples in this radio power range are considered separately and is thus consistent with unified theories (Antonucci, 1993).

The correlation for the high radio power AGN might be indicative of there being two populations of radio-loud objects with a split at around $\log_{10}(L_{325}/\mathrm{W\,Hz^{-1}\,sr^{-1}}) \sim 26$ with the lower radio power objects occupying a wide range of environments, whereas the higher power objects only occur in a narrower range. This result may in fact explain a lot of the conflicting results over whether RLQs occupy denser environment than RQQs. It appears that

many of the authors who find the environments are the same do not have in their samples the most radio powerful of RLQs (e.g. Fisher et al. 1996; McLure & Dunlop 2001b; Wold et al. 2001). This fits with the finding in this chapter that only the most radio-loud ($\log_{10}(L_{325}/\mathrm{W\,Hz^{-1}\,sr^{-1}}) > 26$) AGN seem to inhabit denser environments on average than RQQs.

Initially one might expect that these results could be due to the higher radio power objects having intrinsically larger black hole masses than their lower power or radio-quiet counterparts. Indeed, recent work has found that RLQ's black hole masses are on average 45 per cent more massive than RQQ's (e.g. Lacy et al. 2001; McLure & Jarvis 2004). If the largest black holes as would be expected then reside in the largest dark matter haloes, or are found closer to the centre of their haloes, they would thus also be likely to have the highest density environments. It is shown however, that estimates of the black hole masses of the QSOs in this sample from their SDSS spectroscopy are statistically indistinguishable. This is as a result of the careful matching in QSO optical colours and luminosity. Moreover, the over-density around the QSOs shows no trends with either optical QSO luminosity or black hole mass (Fig. 2.16 and Fig. 2.18) both to the eye or using a correlation analysis (Table 2.3).

At this point, it is worth considering whether there might be a systematic bias in the way the black hole mass estimates are made for the radio-loud and radio-quiet subsets. For example, if the Eddington ratios are for some reason systematically lower for the radio-loud objects then they must host more massive black holes to produce a given optical luminosity. One possibility is that radio-loud objects are powered by a radiatively inefficient accretion

process such as Bondi accretion of the hot phase of the IGM (e.g. Hardcastle et al. 2007) while the radio-quiet objects are accreting cold gas in the standard manner. However, such a possibility is easily dismissed since radiatively inefficient accretion processes can only explain the multi-wavelength properties of low-excitation radio sources which are almost all Fanaroff-Riley (FR) class I objects whereas the entire sample used here is made up of QSOs, with the radio-loud objects all having radio luminosities typical of FR II sources (Fig. 2.5). Furthermore, given that the samples are matched in absolute optical magnitude and optical colours, any difference in accretion properties must contrive to produce a distribution of MgII line widths that would lead to identical black hole mass distributions; this seems unlikely.

This discussion leads to the one of two potential conclusions, either the environments of the AGN are somehow affecting the observed radio properties or alternatively the AGNs radio emission is influencing the environmental density. The second of these is a much harder scenario to envisage as it would mean that ∼100 kpc-scale radio jets would need to influence galaxy formation which occurs on Mpc scales. That said there are suggestions that large scale radio jet activity could indeed quench or trigger star formation on a group or cluster scale (e.g. Rawlings & Jarvis 2004; Wiita 2004).

Exploring the first of these hypothesis leads to the question why would a denser environment in terms of galaxies lead to increased radio emission? Well what do we know is required for synchrotron radio-emission? Firstly a source of high energy particles and secondly a relatively dense medium for them to collide with. We know the first of these exists in the form of the AGN and the second can either be the Inter-Stellar-Medium (ISM) or

the Inter Galactic Medium (IGM). The jets in powerful radio-loud AGN remain relativistic until they reach the IGM and so it is this which is more important for their luminosity. A potential explanation for a denser IGM is as follows. Firstly tidal stripping of gas and dust from galaxies would be more prevalent in denser environments due to higher exposure to close encounters or mergers and secondly the larger potential well the galaxy would be sitting in attracting gas into the IGM. The IGM would likely therefore, be denser in regions of higher galaxy density. A higher IGM density gives more material for kpc-scale radio jets to work on once they have left the host galaxy, thereby increasing the radio luminosity produced through synchrotron losses.

This effect, known as jet confinement, was discussed by Barthel & Arnaud (1996) who use it to explain the unusually steep far-infrared to radio spectral slope of Cygnus A as boosting of the radio luminosity caused by a higher environmental density. The estimated enhancement in radio luminosity for AGN in clusters, compared to the field, was given by Barthel & Arnaud (1996) as ~ 1.5 orders of magnitude which might well be sufficient to explain the results presented here (see Fig. 2.19 or Fig. 2.23). In the local universe Kauffmann et al. (2008) find a similar difference in matched samples of radio-loud and radio-quiet emission-line AGN from SDSS; they also offer an explanation in terms of radio jets being enhanced in denser environments. The results of this analysis suggest that this relationship extends to higher luminosity objects at higher redshifts.

An alternative explanation is that the differences observed in the radio properties and environments of AGN are linked by a third parameter such as the spin states of their black holes. This is certainly plausible as it could

much more readily explain a radio power dichotomy, if indeed it turns out that there is one. It could also explain the results presented here if for some reason the spin is affected by the environmental density. This idea is mentioned frequently in the literature and usually takes the form of black holes spinning faster in denser environments due to increased exposure to mergers, which spin up the black holes (e.g. Wilson & Colbert 1995, Moderski et al. 1998, Volonteri et al. 2007 and Sikora et al. 2007). However as yet it is not observationally possible to measure the spin of black holes in high-z AGN and so the hypothesis is not yet testable.

2.7 Conclusions

This Chapter presents analysis of the environments of a large sample of AGN at $z \sim 1$ in order to study the relationship between AGN activity and environmental density at an epoch close to the peak of AGN activity. The main conclusions are as follows:

1. The AGN fields show, on average, an excess above the field of ~ 5 galaxies containing a substantial evolved stellar population within a projected distance of ~ 700 kpc. The source density shows a sharp peak (2-3 galaxies) within a projected radius of ~ 300 kpc of the AGN.

2. The environments of the RLQs and RQQs in the sample are shown to be tentatively different, with the RLQs inhabiting denser environments at the 96 per cent confidence level.

3. There also appears to be evidence for a trend of increasing galaxy over-

density with increasing AGN radio luminosity. This is explored further and it is found to be caused by a strong correlation in the highest radio luminosity RLQs and RGs.

4. The spatial clustering amplitude is measured for the AGN in the sample and the means compare reasonably well with those in the literature at lower redshift. In general it is found that the RQQs are found on average in environments comparable to Abell class 0 clusters whereas the RLQs and RGs are, on average, in environments similar to Abell class 0/1.

5. Since the RLQs and RQQs have indistinguishable black hole mass distributions the observed difference in environmental density is not a result of observing different populations of objects. This leads to the conclusion that the radio power of an AGN is in some way influenced by the environmental density in which it resides.

6. These results could be explained by jet confinement, *i.e.* the boosting of radio jets in areas of higher IGM density. A denser IGM might be expected in galaxy-dense regions due to mergers and tidal stripping of gas and dust or simply a deeper potential well to attract gas.

7. Alternatively perhaps the environments are linked to the radio properties of AGN via the spin state of their black holes which may also be increased in dense environments through increased merger exposure.

It is of course entirely possible and likely that the radio properties of AGN are not determined by a single parameter but instead a combination of pa-

rameters which would naturally explain the large scatter on the observed relationship found here. It is clear from previous work that for an AGN to be radio-loud it requires a certain mass of black hole ($\sim 10^8$ $M_\odot$, McLure & Jarvis 2004) but it is shown that this cannot be the only factor involved. This work and that of others using well matched samples (e.g. Kauffmann et al. 2008; Donoso et al. 2010) suggests that there is some link between radio-loudness and the environment as well. Future observations, such as deep radio observations with the Low-Frequency Array (LOFAR), will allow us to investigate the environments as a function of radio luminosity well down into the RQQ régime and up to higher redshifts, and place firmer constraints on the conclusions based on this sample alone.

Chapter 3

The Environments of High-z QSOs using the *Spitzer* Extragalactic Representative Volume Survey (SERVS)

This Chapter is mostly based on work published in the Astrophysical Journal (Falder et al., 2011).

3.1 Introduction

The *Spitzer* Extragalactic Representative Volume Survey (SERVS; Mauduit et al. 2012, in prep) is a warm *Spitzer* survey at 3.6 and 4.5 μm which will cover an area of 18 deg^2 in fields already extremely well-studied, and hence with a large amount of ancillary data. The survey reaches depths of $\sim 1\,\mu$Jy

allowing L_* galaxies to be observed out to $z \sim 5$, thus making it ideal for studying the environments in which AGN reside out to these epochs.

Recently, *Spitzer* has been has been utilised in the search for high-redshift galaxy clusters (e.g. Eisenhardt et al. 2008, Wilson et al. 2009, Papovich et al. 2010). Its wavelength range, specifically that of IRAC, provides the necessary extension needed to take colour selection cluster finding techniques to $z > 1$. Indeed it has led to the highest known spectroscopically confirmed cluster to-date (Papovich et al. 2010; Tanaka et al. 2010) at $z = 1.62$. This was found solely from an over-density of IRAC sources in the XMM-LSS field of the *Spitzer* Wide-Area Infrared Extragalactic survey (SWIRE; Lonsdale et al. 2003). As the 3.6 μm filter passes up and over the stellar peak the 3.6-4.5 μm colour changes from negative to positive. This makes for a useful way of removing the low redshift foreground contamination when $z > 1.3$. In addition, the negative K correction caused by the peak in stellar emission moving towards longer wavelengths means that IRAC can efficiently reach the depths required to study the high-redshift universe in technically achievable exposure times. At $z > 3$ only a handful of these potential clusters have been detected to date, mainly around individual radio-galaxies (e.g. Overzier et al. 2006, 2008).

These features that have proved useful for cluster finding are also very useful for the study of the environments of AGN at high-z for the same reasons. Recently, in a study similar to the work in this thesis Hatch et al. (2011) have studied the environments of $z \sim 2.4$ radio galaxies. In their work they find potential proto-clusters around three of their six targets, with good evidence that the excess objects are blue star-forming galaxies. In Chapter 2

over-densities were found at $z \sim 1$ in IRAC data around a large sample of SDSS QSOs and RGs. The depth of those observations allowed for the detection of $\sim 0.3L_*$ galaxies at the redshift of the AGN ($z \sim 1$) and could have detected L_* galaxies to $z \sim 2$. On the other hand, SERVS will allow the detection of L_* galaxies at $z \sim 5$ (Fig. 3.1).

The main difference between the AGN sample used in Chapter 2 and the sample used in this chapter is that SERVS is a field rather than a targeted or snap shot survey. This means the sample of AGN is selected due to being in the survey region rather than based on a set of criteria related to the AGN. Hence, there will not be a sufficient number of powerful radio-loud AGN to look for similar effects as seen in Chapter 2 because these are rare and require large areas or snapshot surveys to study in large numbers. However, the almost unrivalled combination of depth and area that SERVS provides makes it possible to see if luminous AGN in general are found in over-densities at $z >> 1$.

The layout of the Chapter is as follows: in Sections 3.2 and 3.3 the observations and the sample of QSOs are discussed, in Section 3.4 the analysis is described, the results are presented in Section 3.5 before comparing them to the results from Chapter 2 at $z \sim 1$ in Section 3.6 and to models in Section 3.7. Finally there is a summary in Section 3.8.

3.2 Observations and Catalogues

The primary observations used in this Chapter are those from the *Spitzer* Extragalactic Representative Volume Survey (SERVS). The data reach ap-

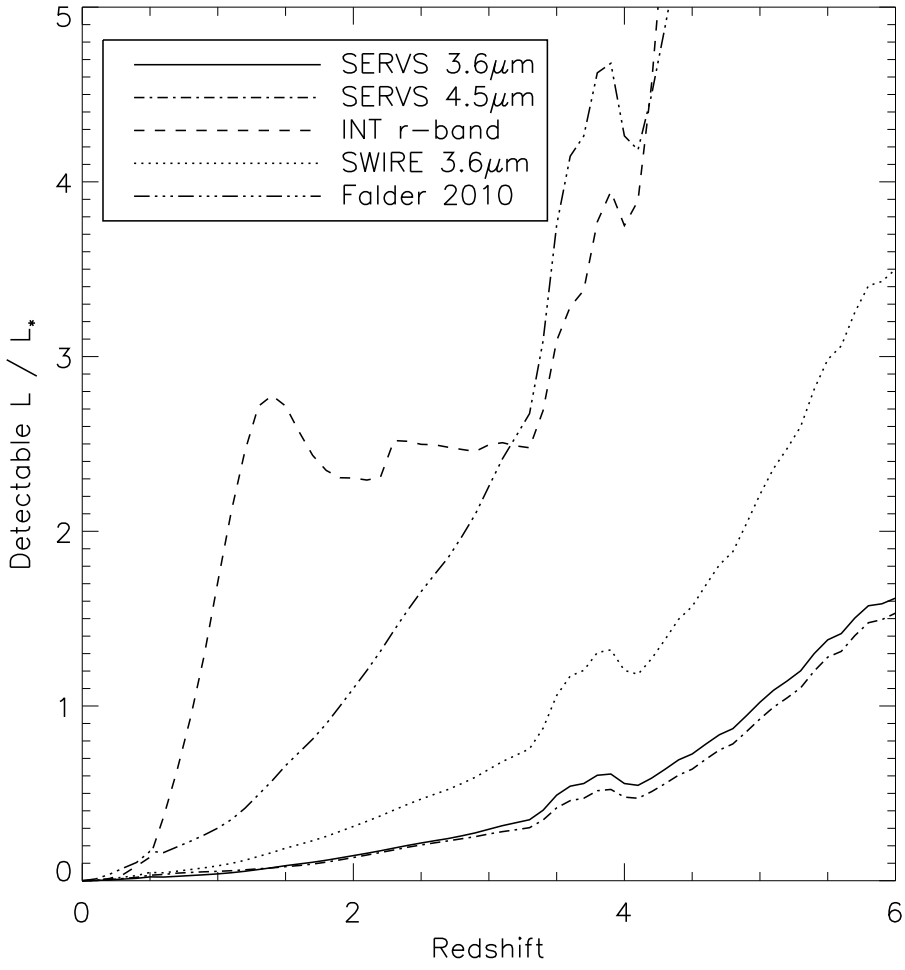

Figure 3.1: The sensitivities in terms of L_* versus redshift for the INT r-band data (dashed line) as well as the SERVS 3.6 μm and 4.5 μm data (solid and dash-dot lines respectively). Also shown for comparison is the SWIRE survey's 3.6 μm data (dotted line) and the 3.6 μm data used in Falder et al. (2010) (triple-dot-dash line). Full details of the models used to construct this figure are given in the text.

proximate average 5 σ depths of ~ 1 μJy (23.9 mag) at 3.6 μm and ~ 2 μJy (23.1 mag) at 4.5 μm. Eventually SERVS will cover 18 deg^2 of the extremely well studied fields from the SWIRE survey. In this chapter the SERVS overlap with the SDSS is used, thus restricting the analysis to the northern SERVS fields: Elais N1 (EN1; 1.01 deg^2 that overlaps the SDSS) and the Lockman Hole (4.93 deg^2). Full details of the fields, observations and data reduction as well as the survey strategy will be given in Mauduit et al. (2012, in prep).

In addition to the *Spitzer* data, optical photometry from the *Issac Newton* Telescope (INT) Wide-Field Camera and Kitt Peak National Observatory (MOSAIC1), originally used by the INT Wide Field Survey (McMahon et al., 2001) and the SWIRE optical imaging campaign (Lonsdale et al., 2003) but since expanded and re-reduced by Gonzalez-Solares et al. (2012, in prep), is used. These data reach a 5σ depth of 24.2 mag in the r-band.

In Fig. 3.1 the sensitivity of the SERVS data and the r-band data in terms of L_* is shown. For comparison the 3.6 μm sensitivity from the SWIRE survey and that of the data used in Chapter 2 is shown. The main point to note is that while SWIRE can detect L_* galaxies at $z \sim 2.5$, SERVS can detect them at $z \sim 5$. This plot was made using the restframe K-band luminosity function of Cirasuolo et al. (2010) assuming no evolution past $z = 4$. All colour conversions between bands are derived using a Bruzual & Charlot (2003) elliptical galaxy model with reddening of $A_v = 0.8$ applied according to the extinction law of Calzetti et al. (2000) and the HYPERZ software package (Bolzonella et al., 2000); this will be discussed at length in Section. 3.4.2. The K correction is calculated using this model from Bruzual

& Charlot (2003) to place SEDs at various redshifts and comparing the rest-frame and observed-frame flux in the K-band filter.

The catalogue used is the SERVS data fusion catalogue (Vaccari et al. 2012, in prep). This matches the single-band SERVS IRAC 3.6 and 4.5 μm catalogues generated with the SExtractor software package (Bertin & Arnouts, 1996) using a search radius of $1''$, computes an average coordinate (for sources detected in both bands) and matches the resulting IRAC two-band catalogue with ancillary photometric data-sets from the far-ultraviolet to far-infrared (e.g. GALEX, SDSS, CFHT, CTIO, ESO, INT, KPNO, 2MASS, UKIDSS and SWIRE) using a search radius of $1.5''$. Since the idea is to use the 3.6-4.5 μm colour to select sources likely to be at the correct redshift for the QSOs, this for the most part restricts the catalogue to only those sources which are detected in both bands.

Determining the exact depth of a large survey is non-trivial as the coverage is not uniform in depth due to the overlaps of the scan pattern. Small areas will therefore be deeper than the average, this is an important consideration when measuring source density. Therefore to study the environments accurately the data needs to be restricted to a flux level which ensures equal depth throughout the maps. This issue will be addressed with a completeness simulation in Section 3.4.5.

3.3 Sample

QSOs are identified in the SERVS regions by cross matching the SERVS source catalogues with the seventh data release of the SDSS quasar survey

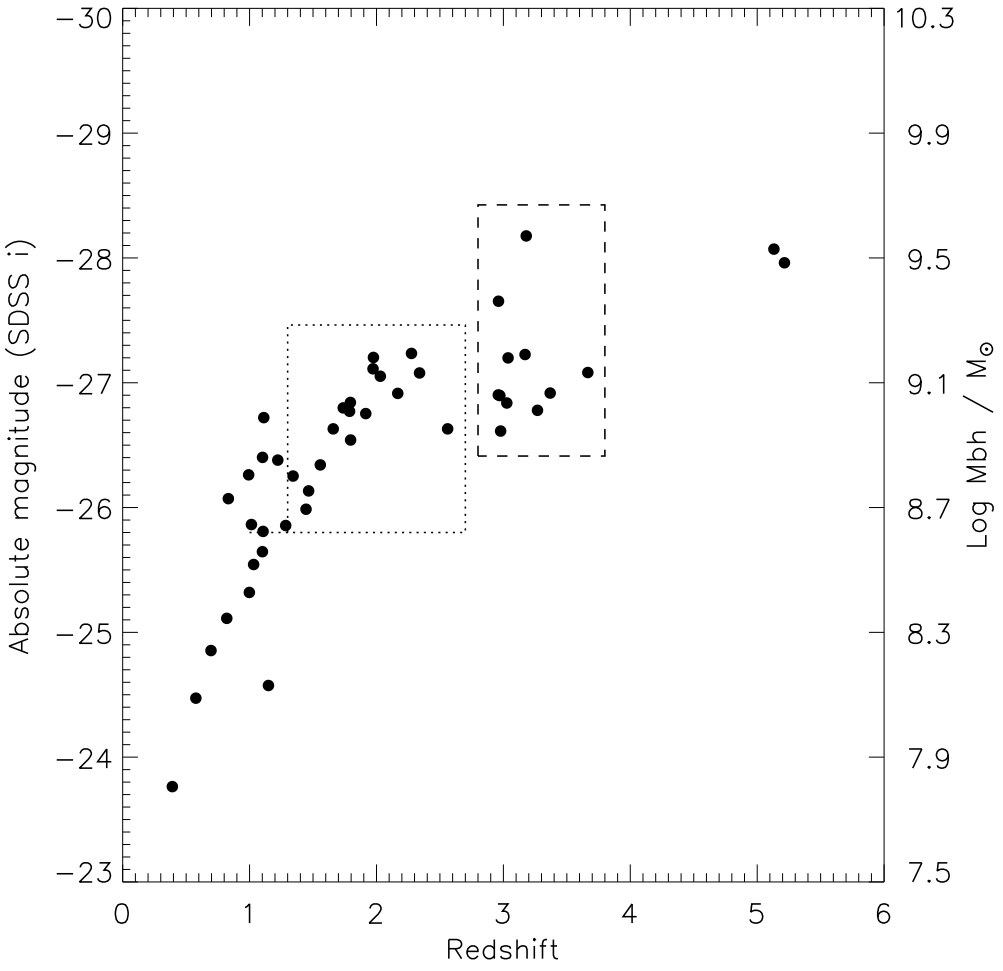

Figure 3.2: Redshift versus rest frame optical absolute magnitude (SDSS i-band) for QSOs from the seventh data release of the SDSS quasar survey (Schneider et al., 2010) which are in the SERVS fields. The boxes show the two redshift bins the sample is split into for study as described in the text. On the right hand axis black hole mass lower limits for these QSOs are shown. These are calculated by assuming that the QSOs are accreting at the Eddington limit and using the relation from Rees (1984) with a bolometric correction factor of 15 (Richards et al., 2006a) to the SDSS i-band absolute magnitudes.

(Schneider et al., 2010) using the software package TOPCAT (Taylor, 2005) to select the SDSS QSOs in the overlap regions. In total 46 QSOs are found in the SERVS northern fields; 5 in EN1 and 41 in the Lockman Hole. The small number in EN1 is due to the SDSS only overlapping a small portion of the observed region. These numbers include only QSOs that are at least 400″ from the edges of the regions of equal coverage in both the 3.6 and 4.5 μm maps which allows the study of the environments of theses QSOs out to these distances without any effects from the image edges. The distribution of the sample in the L-z plane is shown in Fig. 3.2. Six of the lower redshift QSOs are detected by the FIRST radio survey (Becker et al., 1995) at 1.4 GHz, these could therefore be considered as radio-loud. The small sample size spread across a range of redshifts however means that these cannot be studied on their own with this analysis like they were in Chapter 2.

In this chapter the environments of the higher redshift QSOs in the SERVS data are concentrated on as their environments have not been studied before with data of this depth or for more than a handful of objects. The higher redshift ($z > 1.3$) QSOs are split into two course redshift bins which are shown in Fig. 3.2. The first is centred on $z \sim 2.0$ and spans the range $1.3 < z < 2.7$ and the second is centred on $z \sim 3.3$ and spans the range $2.8 < z < 3.8$. These bins were chosen since there is a natural divide in the sample at $z \sim 2.8$ which gives samples of 11 and 17 QSOs in the two bins. This is a trade off between having enough QSOs in the sub-samples for stacking whilst restricting the sample to as small a fraction of cosmic time as is possible.

3.4 Analysis

3.4.1 Radial Search Stacking

To study the QSO environments the relatively simple technique used in Best et al. (2003) and in Chapter 2 is employed. This involves placing a series of concentric annuli around each QSO and counting the number of sources that meet the selection criteria, described in more detail later in Section 3.4.2. The source density as a function of radial distance can then be examined for each QSO. The annuli are kept to a fixed area as the radial distance increases to keep the Poisson noise at a similar level from bin-to-bin. The QSOs themselves are excluded from the search because including them would bias the first annulus; this is done by not counting any sources within 1″ of the QSO's SDSS coordinates.

As the aim of this chapter is partly to compare these findings to those from Chapter 2 on the $z \sim 1$ sample the aim is to conduct the analysis in a comparable way. In Chapter 2, two over-densities were reported, a sharp peak in the central source density projected to be within 300 kpc of the AGN and then a lower level over-density extending out to at least a projected distance of 700 kpc. This pattern has also been seen elsewhere in the literature, for example in Best et al. (2003) around powerful radio sources at $z \sim 1.6$, and by Serber et al. (2006) for SDSS QSOs.

When over-densities are looked for within 300 kpc of the AGN in this sample, while many AGN appear to have an over-dense first annulus, they lack a significant detection. This is probably due to having far fewer targets in the sample. The sample used in Chapter 2 contained a much larger number

of AGN (∼170) than are present in any of the redshift bins or indeed the whole sample.

To allow for an easy comparison to the larger scale over-density found in Chapter 2 annular bins with a first bin projected physical radius of 700 kpc are used. These match the largest search radius possible in the Chapter 2 data, which was in turn fixed by IRAC's field of view. To take into account the change in scale between different redshifts the angular bin sizes for each QSO are adjusted based on its redshift. This means the annuli are matched in terms of their physical size, where the radius of the first annulus is 700 kpc at the redshift of each QSO.

To achieve a statistical result the source density of the QSOs in two coarse redshift bins are stacked together using the raw number counts. To ensure that like with like are being compared in the stacking analysis we match the range of galaxy luminosities that the survey is sensitive to around each QSO. This is done in each redshift bin by calculating what absolute magnitude the survey flux limit represents at the highest redshift of the QSOs in that bin, and then adjusting the flux cut used around each QSO to ensure the surveys sensitivity is matched for each QSO in that bin. As an upper limit, the flux a $10L*$ galaxy would have at the maximum redshift of the redshift bin is calculated and applied as an upper cut on sources with fluxes greater than this limit. The reason for choosing $10L*$ is to ensure this is not cutting any likely associated galaxies allowing for significant uncertainty in the luminosity function at these redshifts.

The reasoning for adopting this method of analysis is that at these high-redshifts other methods of measuring environmental density such as B_{gq} and

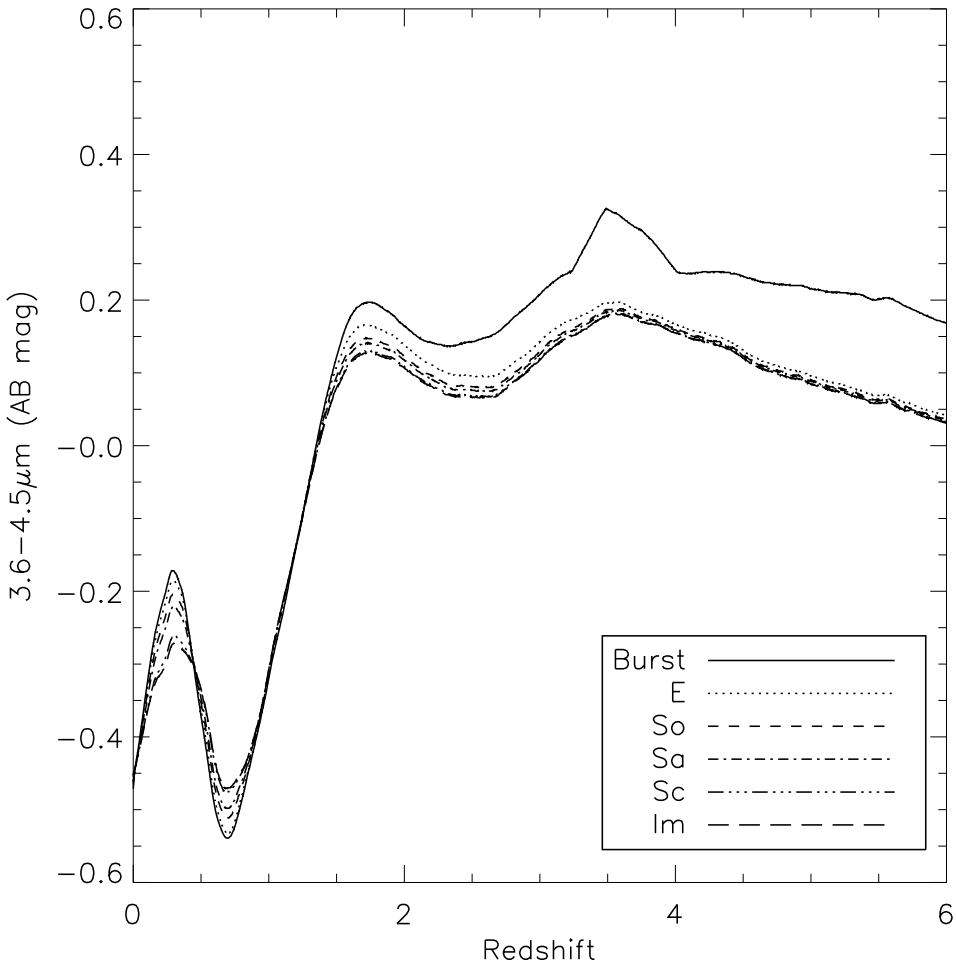

Figure 3.3: IRAC 3.6-4.5 μm colour versus redshift, care of the Bruzual & Charlot (2003) stellar population models and the HYPERZ software package (Bolzonella et al., 2000). The colours are shown for six different commonly used models; these consist of a single burst model, four exponentially declining SFR models representing elliptical, S0, Sa and Sc type galaxies with $\tau =$ 1,2,3 and 15 Gyr respectively, and a model with a constant SFR (Im). All models have a formation redshift of 10 and no reddening.

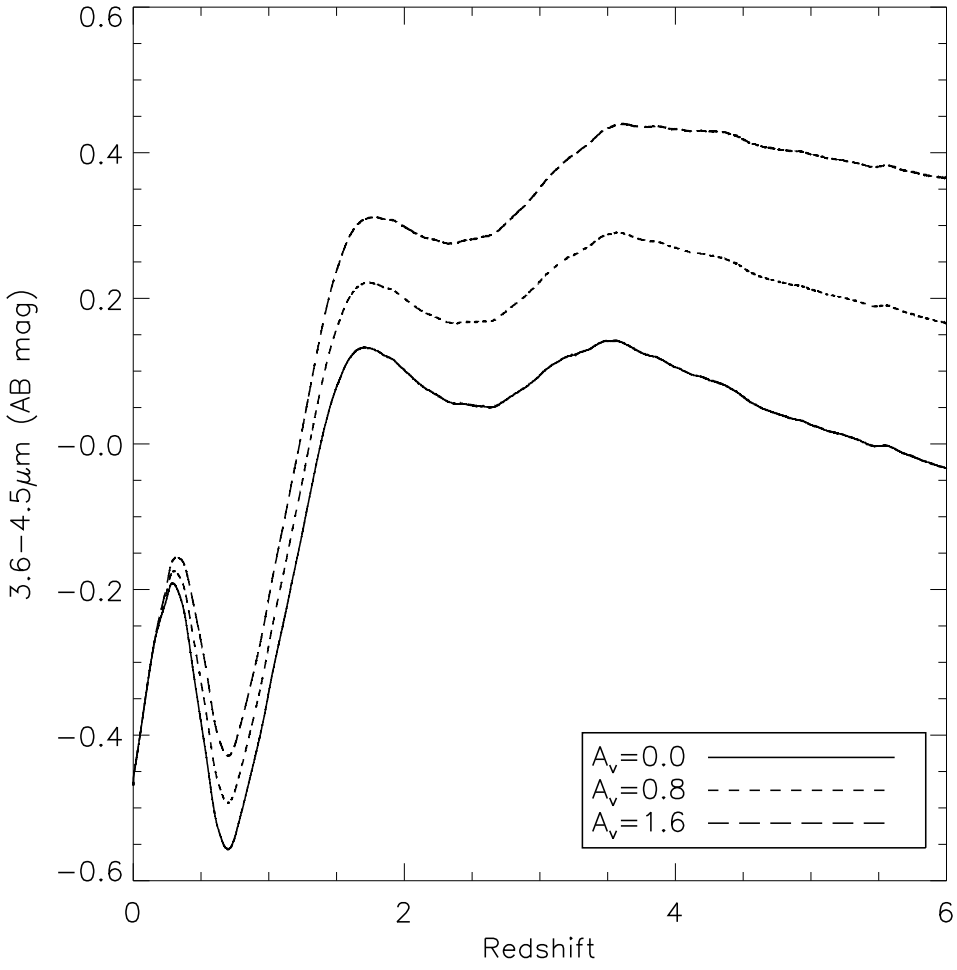

Figure 3.4: IRAC 3.6-4.5 μm colour versus redshift. Showing the effect of reddening on the elliptical model from Fig. 3.3. The lines show models without reddening and with $A_v = 0.8$ and 1.6 applied according to Calzetti et al. (2000). This shows with Fig. 3.3 that a reasonable level of reddening is likely to have more of an effect on a galaxy's colour in this colour space than its star formation history.

two-point correlation functions are difficult to calibrate correctly. The large error bars that result from the assumptions made about the luminosity function and optical K correction at these redshifts also make obtaining statistical results difficult from more sophisticated measures of environmental density.

3.4.2 Galaxy Colours

In order to increase the sensitivity of the survey to galaxies at the same redshifts as the QSOs the IRAC 3.6-4.5 μm colour is used. To help decide on the correct colour cuts to make, the HYPERZ software package (Bolzonella et al., 2000) and the stellar synthesis models of Bruzual & Charlot (2003) are used. In Fig. 3.3 the colour of six commonly used models versus redshift is shown. These are a single burst model, four exponentially decreasing star formation rate (SFR) models with timescales τ=1, 2, 3 and 15 Gyr designed to represent elliptical, S0, Sa and Sc type galaxies respectively and a model with a constant SFR (Im). What is clear from Fig. 3.3 is that, with the exception of the burst model all the models produce a very similar 3.6-4.5 μm colour; at most the burst model differs by 0.15 mags.

In Fig. 3.4 the effect that reddening has on the 3.6-4.5 μm colour is shown; this is shown for the elliptical model without reddening along with two models with $A_v = 0.8$ and 1.6, added according to the Calzetti et al. (2000) reddening law. This shows that adding a reasonable amount of reddening can have a bigger effect on this colour space at high-z than the choice of star-formation history. In all cases a formation redshift of $z = 10$ has been assumed. Changing this value to $z = 100$ made virtually no difference, and

although using $z = 5$ does make a difference, at most it makes the colour bluer by only ~ 0.1 magnitudes at high-z. The key thing to note is that for $z > 1.3$ this colour space provides a good method for selecting galaxies most likely to be at high-redshift.

Since the QSO sample spans a range of $0.3 < z < 5.3$, different colour cuts can be applied to encompass different parts of the sample. Where the results of the analysis are interpreted in terms of L_* the elliptical model with $A_v = 0.8$ is used (see Fig. 3.1). However, for the colour cuts on the data, colours that would fit any of the models are experimented with. There are several factors to consider here, firstly the real colours of galaxies will contain significant scatter. Only two parameters that can scatter the colours are shown, SF history and extinction, but in reality there will be more, not to mention the intrinsic scatter produced by measurement errors.

In Papovich (2008) the scatter of the 3.6-4.5 μm colour was shown by over-plotting data with spectroscopic redshifts on to the model predictions; this was possible for $z < 3$ and it showed that there was ~ 0.2 mags of scatter at all redshifts. An especially problematic feature that Papovich (2008) reported was a population of galaxies at $z \sim 0.5$ with a significantly redder colour than could be predicted by any of the fitted models or with reddening. Papovich (2008) found these galaxies had colours inconsistent with being AGN but instead could be explained by galaxies with an extreme level of star-formation like ARP220 where warm dust is heated by star-formation. These galaxies will certainly contaminate the colour space predicted to be occupied by high-z galaxies.

These issues create problems as encompassing a range of 0.4 magnitudes

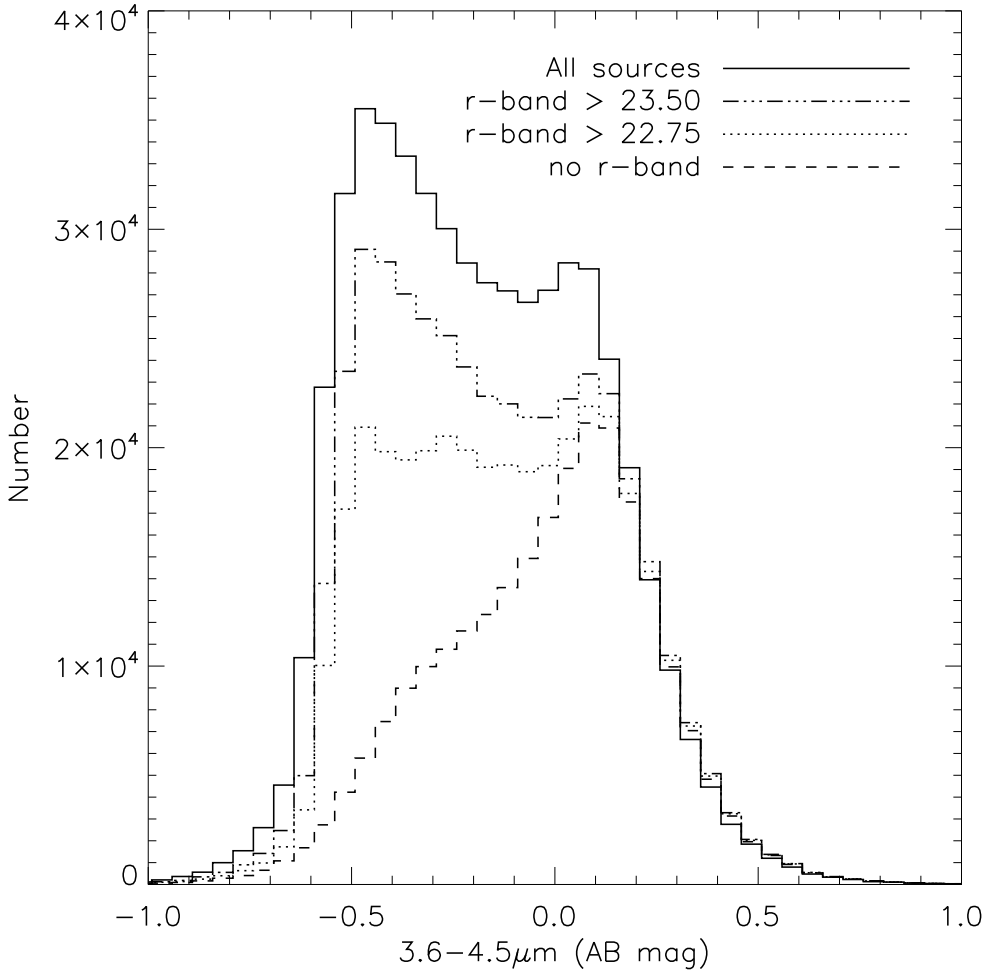

Figure 3.5: Histogram of the IRAC 3.6-4.5 μm colour distribution in the SERVS source catalogues, shown for all sources (solid line), for sources with an r-band detection of 23.50 or fainter (dot and dashed line), for sources with an r-band detection of 22.75 or fainter (dotted line) and for those sources not detected in the r-band (dashed line). This figure clearly shows that most sources with 3.6-4.5 μm > 0.2 are undetected in the r-band and therefore most likely to be at high-z, as Fig. 3.3 would suggest.

of colour space will mean a large foreground contamination is included, potentially washing out the signal from the high-z galaxies of interest. It may prove the case that the survey is more sensitive to galaxies at the redshifts of interest by using a narrower region of colour space which, while losing some galaxies at the correct redshift, means more contamination is removed. The distribution of IRAC 3.6-4.5 μm colour from the SERVS source catalogues is shown in Fig. 3.5. When compared to Figs. 3.3 & 3.4 the spread of colours is reassuringly similar.

What is needed therefore is a way of optimising the colour cut criterion for each redshift range. Ideally this would be done using a spectroscopic sample of galaxies which are in the SERVS fields, similar to that used by Papovich (2008). It would then be possible to use different colour criteria and see which values return the most galaxies at the redshift required compared to other redshifts. However, the number of spectroscopic redshifts available in the SERVS fields, or in general at these high-redshifts, is insufficient for this type of analysis. Instead therefore, a Monte-Carlo method is used to adjust the colour-cut criteria used around the QSOs. This method allows both the upper and lower colour cut to be adjusted in steps within suitable ranges determined from Figs. 3.3 and 3.4. The source-density is measured for each Monte-Carlo run and the colour cuts which give the largest over-density with respect to the background are taken to be the most efficient. This works on the assumption that the signal will peak when we include the most galaxies associated with the QSOs compared to contaminating galaxies. To get an idea of the probability that these over-densities are real, and not just noise spikes, the same experiment can be conducted many times around randomly

chosen locations in the SERVS maps, avoiding the locations of the QSOs in the process.

The inability to effectively remove foreground contamination with this colour space for $z < 1.3$ makes the QSOs at these redshifts harder to study with this method. At these low redshifts the available ancillary data are also able to provide a better means to study environments using photometric redshifts or alternative colour cuts. This is another reason why in this chapter this part of the sample is avoided. There are far larger studies of such objects' environments already in the literature (for example Yee & Green 1987, McLure & Dunlop 2001b, Wold et al. 2001, Kauffmann et al. 2008, and with *Spitzer* in Chapter 2 and so it is felt that a study with the small number in this sample would add little to the work already done at these redshifts. In contrast, as mentioned the environments of high-z QSOs have not been well studied in large numbers or with data of this depth before.

3.4.3 Ancillary Data Cuts

In addition to the IRAC colour cut discussed in Section 3.4.2 the r-band data from the INT (which reaches a 5 σ limiting magnitude of 24.2) are used to cut as much additional foreground contamination as possible. This will hopefully allow at least some of the $z \sim 0.5$ galaxies, mentioned previously, that contaminate the colour space of higher-z galaxies to be removed. The effect of removing all sources with an r-band detection on the 3.6-4.5 μm colour space is shown in Fig. 3.5. The cut has the clear effect of removing around two thirds of the sources with a negative 3.6-4.5 μm colour; this is

consistent with Figs. 3.3 & 3.4 which suggest that these sources should have $z < 1.5$. The other interesting feature is that very few sources with 3.6-4.5 μm > 0.2 are detected in the r-band at all, again consistent with Figs. 3.3 & 3.4, which suggest that these sources are likely to lie at $z > 3$.

3.4.4 Background Level

It is important to have a measure of the background level of sources expected in the field with which to measure any over-densities against. There are several ways in which this can be done, one would be to use a systematic offset from the target and measure the source density in that region. This is known as a blank or control field and provides an estimate of the local background level; this was the method used in Chapter 2. Another method when working with a large survey such as SERVS is to use a global background where the average source density of a large area or the whole survey is used. There are advantages and disadvantages to each method; using the larger area washes out any fluctuations on small scales which might affect a local value. However, if these local fluctuations are on an angular scale which makes it important to take them into account in the background determination then a local background will help if it is close enough to the target. The trade off with this method is that being too close may result in measuring the same structure of galaxies in both the background and target field.

Both methods have been experimented with in this chapter. The global background has been calculated for each of the two SERVS fields, EN1 and the Lockman Hole, by placing a series of 0.5° radius circles on to the cat-

alogues and determining the average source density contained within them. The local values have been calculated by using the average source density in an annulus which is sufficiently far from the QSOs that it should not be measuring the same structure. These annuli have a maximum radius of 400″ from the QSO to ensure none of them fall off the image edges. The inner radius is determined such that it should be 2 Mpc from the QSOs at their redshift. This should be far enough that it is unlikely to be measuring the same large-scale structure that the QSOs reside in. Most evidence in the literature suggests that this should be sufficient as except for the largest galaxy groups and clusters, most of their members are found within a radius < 2 Mpc (for example Hansen et al. 2005 and Papovich et al. 2010).

Obviously the background levels have to be determined in an identical way to the source density in the environments of the QSOs and will be a different for each colour cut that is used. The error on the background is calculated as the Poisson error on the raw number counts used for the background measurements. This is then scaled to the same area and added in quadrature to the error on the source density measurements to get the error on any over-density.

3.4.5 Completeness

In order to account for the incompleteness of the *Spitzer* data near the flux limit of the survey an extensive completeness simulation was conducted. This largely followed the process used in Chapter 2 and full details are given there. It involved cutting out regions of the *Spitzer* images surrounding each QSO

that measured $900'' \times 900''$, *i.e.* , large enough to include all annuli used in the analysis. Into each of these cutouts 10000 artificial sources are added for 40 different flux levels. To avoid increasing source confusion these were added in batches of 1000 which meant that they were never too close together that they could become confused with another artificial source. At each flux level the number of inserted sources was compared to those found in the SExtractor catalogues. A source was considered recovered if it was found within $1.2''$ (2 pixels) of the inserted location and within a factor of two of the inserted flux. The results of this analysis are measured for each annulus separately which then enables a completeness correction to be applied specific to each annulus. This means it is possible to account for missed area in the vicinity of bright stars or indeed the QSOs, as was shown to be an issue in Chapter 2.

To eliminate the scatter in the measured completeness curves as in in Chapter 2 an empirical model of the form Completeness $= (S^a)/(b + cS^a)$ (Coppin et al. 2006) was used, where S is the 3.6 or 4.5 μm flux density and a, b and c are constants that are fitted. It was found, however, that this model alone was unable to provide a good fit at the knee between the bright end and the steep slope; the data appear less complete here than would be expected based on the S shape curve although this is at most a 10 per cent effect. It is suspected this effect is likely due to source confusion as the SERVS data are confused using the classical definition of 30 beams per source (Mauduit et al. 2012, in prep). In order to overcome this effect a power-law was fitted to the data points when the completeness was greater than 0.70 (see Fig.3.6). The completeness is measured in both the 3.6 μm

and 4.5 μm images. This means it is possible for each detected source in the real catalogues to calculate the correct completeness correction to apply by multiplying the completeness fraction corresponding to the measured 3.6 μm and 4.5 μm fluxes of the source. The mean completeness curve is shown for the 3.6 μm data in Fig. 3.6 based on the outer annuli, therefore away from the bright QSOs.

This kind of completeness simulation goes some way to addressing the issue of the differing depth of a large survey as it measures the completeness on small scales. However as with all completeness simulations there will be errors associated with the corrections applied and so usual practice is to only apply corrections up to a factor of two. Therefore the flux of sources should be restricted at a level where at worst the survey is 50 per cent complete. As the first annulus is likely to contain most of the over-densities it is important that the data are always at least 50 per cent complete in these annuli. The mean 50 per cent completeness level in the first annulus at 3.6 μm is 1.50 ± 0.11 μJy ($23.46^{+0.08}_{-0.07}$ mag) and at 4.5 μm of 1.77 ± 0.08 μJy ($23.28^{+0.05}_{-0.05}$ mag). To be conservative sources are only used which have fluxes greater than the highest flux level at which any of the QSO's first annuli are 50 per cent complete in each channel; these values are 1.71 μJy (23.32 mag) at 3.6 μm and 1.89 μJy (23.21 mag) at 4.5 μm.

3.5 Results

As previously mentioned in order to have suitable numbers of objects for stacking, the sample is divided into the two redshift bins shown in Fig. 3.2.

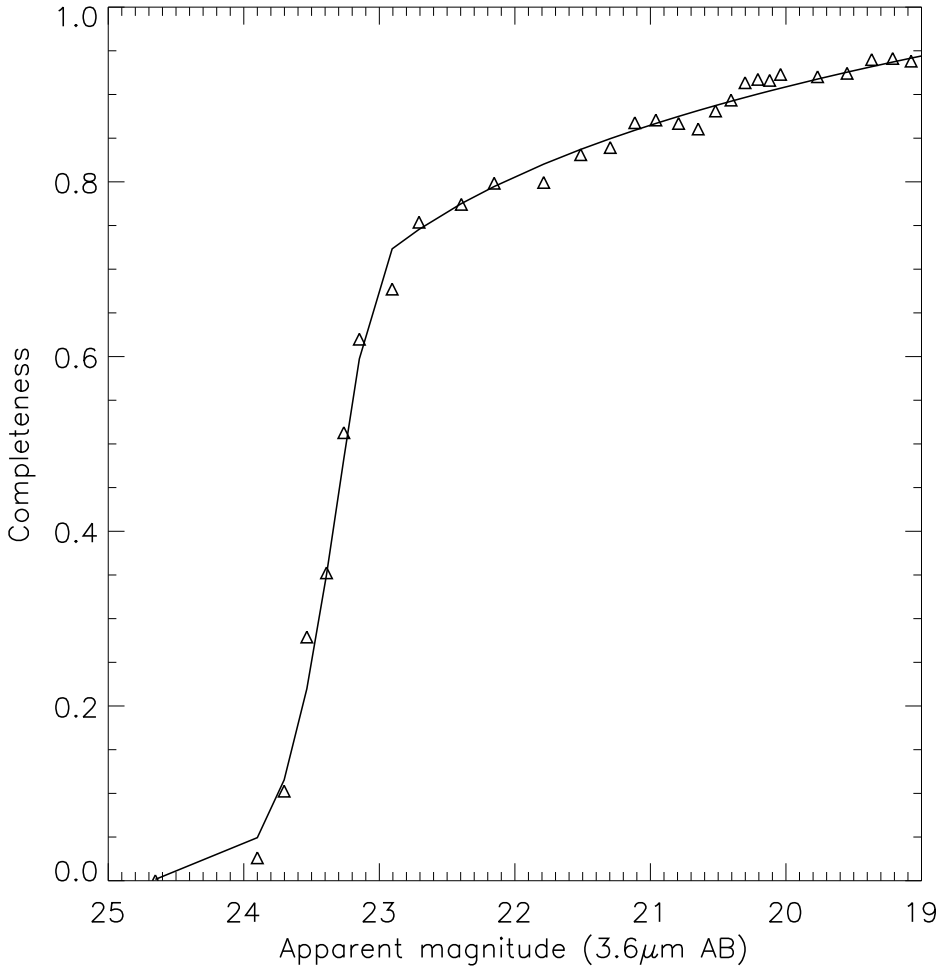

Figure 3.6: The mean completeness fit for the IRAC ch1 data made using the average of the completeness in the outer few annuli, therefore away from the bright QSOs. The data points show the results from the extensive simulation and the curve is a combination of a fit to an empirical model of the form Completeness $= (S^a)/(b + cS^a)$ for completeness less than 0.7 and a power law for completeness greater than 0.7 (see text for full details).

These samples are referred to as the $z \sim 2.0$ sample and the $z \sim 3.3$ sample which refers to the redshift at their centres. The two $z \sim 5$ QSOs environments were also looked at but it was not possible to make a significant detection of galaxies in their environments, which is not surprising for such a small sample at the survey's limit.

3.5.1 $z \sim 2.0$ Sample

In the redshift range $1.3 < z < 2.7$ there are 17 QSOs of which two are detected by FIRST. These are 105001.04+591111.9 and 105039.54+572336.6 with radio luminosities of $\log_{10}(\mathrm{L}_{1400}/\mathrm{W\ Hz^{-1}\ sr^{-1}}) = 25.39$ and 25.16 respectively (calculated using the FIRST radio flux and assuming a spectral index of 0.7). The flux limit at which the data are 50 per cent complete at the maximum redshift of this part of the sample corresponds to an absolute magnitude of -23.4 at 3.6 μm and so the search is restricted around each QSO to galaxies brighter than this value (note that the K correction is ignored within the bin as this is a ~ 0.02 magnitude effect but the uncertainty of this is probably larger). The adopted limit represents galaxies which are brighter than roughly 0.7 L_* in this redshift range.

To choose a colour criterion for this sample Figs. 3.3 and 3.4 are used which show which colours are likely to select galaxies at the redshift of the sample. The Monte-Carlo code is then used to vary both the upper and lower colour cuts in steps within an appropriate range of model predictions. The results of this analysis are shown in Table 3.1 which shows that the most significant over-density of 4.10 σ occurs in the stacked source density

Table 3.1: Table showing the set of upper and lower 3.6-4.5 μm colour criterion used for the Monte-Carlo analysis on the sample centred on $z \sim 2.0$, along with each set's associated Poisson significance. Also shown is the percentage of times that this significance was achieved in the Monte-Carlo simulation around random positions. The colour criterion that gives the most significant over-density is shown in bold. The bottom two colour steps are designed for comparison to look above and below the region of colour space at which it is expected the over-density should lie and indeed these criterion do not produce a significant over-density.

Lower cut	Upper cut	$\sigma_{Poisson}$	Monte-Carlo %
-0.30	0.10	3.22	0.50
-0.30	0.15	4.01	0.10
-0.30	0.20	3.32	0.60
-0.30	0.25	3.13	1.00
-0.30	0.30	3.18	1.00
-0.25	0.10	3.29	0.40
-0.25	**0.15**	**4.10**	**0.10**
-0.25	0.20	3.37	0.40
-0.25	0.25	3.17	0.80
-0.25	0.30	3.21	0.80
-0.20	0.10	3.23	0.40
-0.20	0.15	4.08	0.00
-0.20	0.20	3.29	0.50
-0.20	0.25	3.07	1.00
-0.20	0.30	3.12	1.20
-0.15	0.10	2.60	1.20
-0.15	0.15	3.56	0.20
-0.15	0.20	2.72	1.80
-0.15	0.25	2.50	3.10
-0.15	0.30	2.56	3.20
-0.10	0.10	2.03	3.80
-0.10	0.15	3.12	0.50
-0.10	0.20	2.23	4.30
-0.10	0.25	2.00	7.41
-0.10	0.30	2.08	7.01
-0.05	0.10	1.50	10.11
-0.05	0.15	2.76	1.00
-0.05	0.20	1.79	9.21
-0.05	0.25	1.56	13.71
-0.05	0.30	1.65	12.11
NA	-0.20	0.70	31.03
0.20	NA	-0.84	78.18

when a colour criterion of $-0.25 <$ 3.6-4.5 μm < 0.15 is used. In addition to this IRAC colour cut, sources are removed that are detected in the r-band with an apparent magnitude brighter than 23.5. This criterion corresponds to removing objects that are $\sim 4L_*$ or brighter according to the choice of models, meaning only the rarest galaxies associated with the QSOs are being excluded, if anything.

The individual histograms of source over-density versus radial distance for each of these 17 QSOs are shown in Fig. 3.7; these show the source density with the local background level subtracted. One of these QSOs has a significant over-density around it at > 3 σ level (given by Poisson statistics), while several of the other first annuli are more than 1 σ over-dense, which suggests stacking may produce a robust signal. It is worth noting that neither of the two radio-loud QSOs (labelled) show any sign of an over-density, which means they will not be biasing the stacked source-density as the results of Chapter 2 suggest they might. The global background, while looking consistent in most cases, seems to be too high or low in a few cases, suggesting these QSOs are in a region with a locally high or low background density. It is for this reason the local background measure is favoured and adopted for measuring the level of the over-density.

The resulting stacked source density is shown in Fig. 3.8, which shows an over-density projected to be within 700 kpc of the QSOs and which is significantly above the local background level at the 4.10 σ level (given by Poisson statistics). The next annulus is also above the background level hinting that the over-density extends to around the 1 Mpc scale. If the QSO that has an individually significant over-density is excluded the first

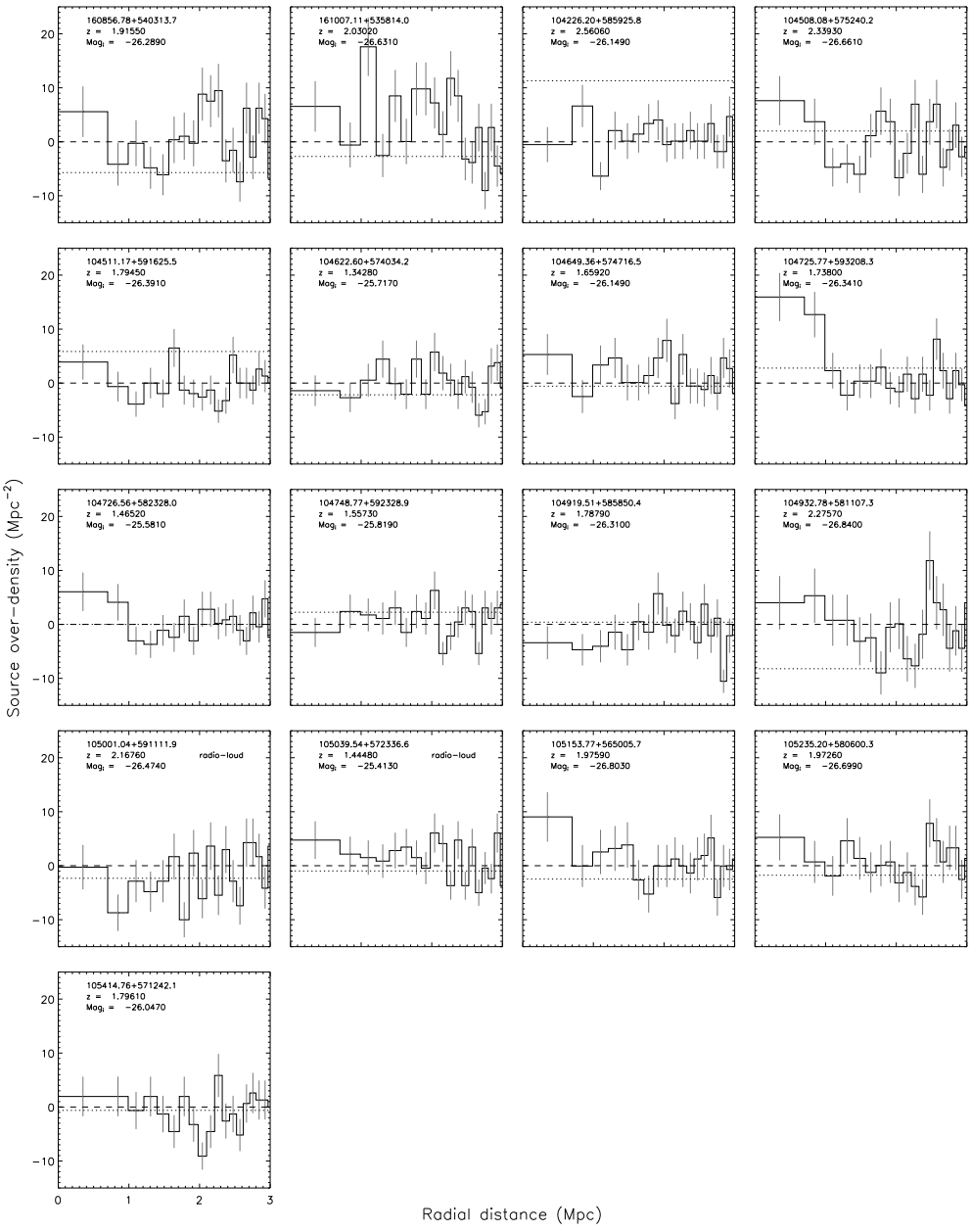

Figure 3.7: Individual source over-density before being completeness correction vs radial distance for the 17 QSOs in the redshift range of $1.3 < z < 2.7$. The first bin has a radius of 700 kpc and the other bins are of the same area as the first. The error bars show the Poisson error on the number counts. The dashed line shows the subtracted local background level (zero level) determined from an annulus spanning the angular distance corresponding to a distance of 2 Mpc to 400 ″ from the QSOs. The dotted line shows, for comparison, the global background as determined from taking the average source density in large apertures over the SERVS fields. Also labelled are the QSO's redshifts and absolute SDSS i-band magnitudes and those which are radio-loud.

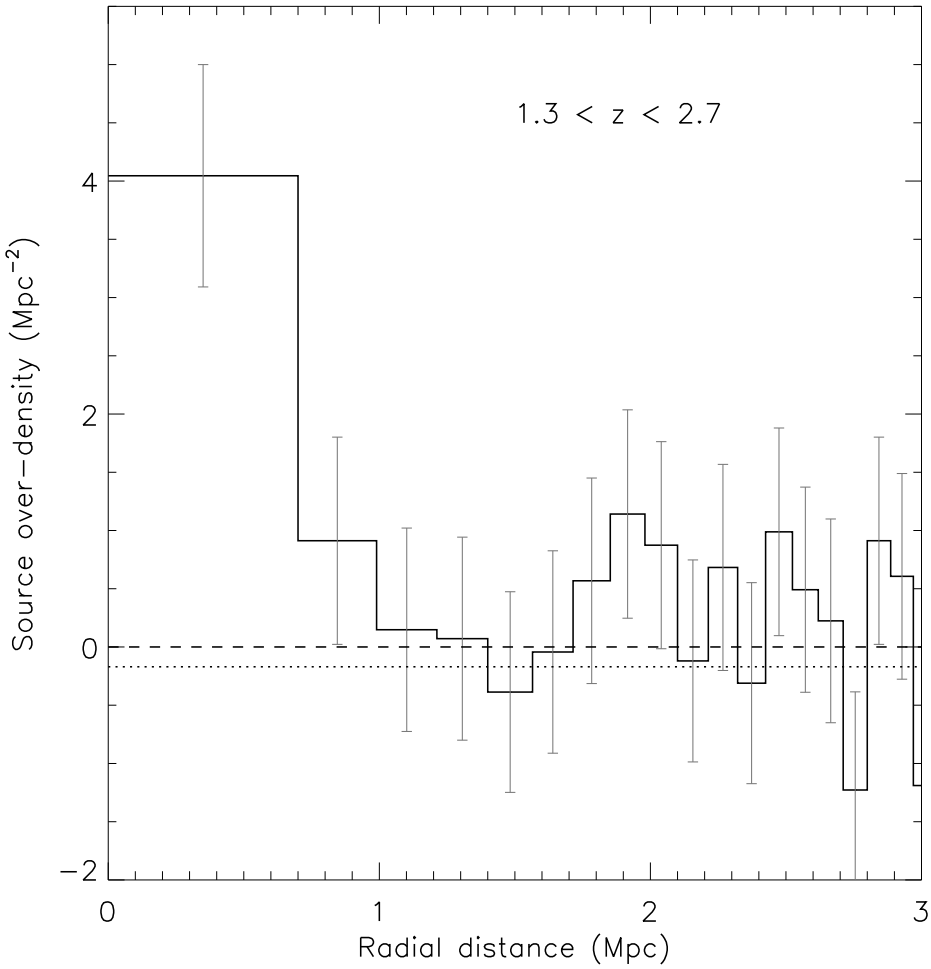

Figure 3.8: Stacked source over-density before being corrected for completeness vs radial distance for the 17 QSOs in the redshift range of $1.3 < z < 2.7$ ($z \sim 2.0$ sample). The first bin has a projected radius of 700 kpc and the other bins are of the same area as the first. The error bars show the Poisson error on the number counts. The dashed line shows the subtracted local background level (zero level) determined from an annulus of angular size corresponding to 2 Mpc to 400 $''$ from the QSOs at their redshifts. The dotted line shows, for comparison, the global background as determined from taking the average source density in large apertures over the SERVS fields.

annulus reduces to the 3.3 σ level suggesting that the over-density in the stacked histogram is not caused by that one object alone. Using the global background has the effect of increasing the detected over-density to the 4.44 σ level; the level of the global background is shown for comparison with a dotted line in Figs. 3.7 and 3.8.

To put the choice of colour cut into context a histogram of the 3.6-4.5 μm colour space is shown in Fig. 3.9 for both the local background and the first annuli surrounding the QSOs; shown in the bottom panel is a histogram of the result of subtracting the colours of sources making up the local background from the colours of sources found in the first annulus. There is a clear over-density significant at the 4 σ level in the QSO fields, the location of which in this colour space is consistent with it being in the redshift range of the QSOs as predicted by the models in Section 3.4.2.

The Monte-Carlo code was then executed 1000 times on batches of 17 random locations (to match the number of QSOs used) being sure to avoid any QSO's location in the process. This analysis shows that similar sized over-densities are found only 0.1 per cent of the time in the same colour space. This increases to only 0.5 per cent of the time over all colour space sampled in the analysis (see Table 3.1). This approach suggests therefore that the over-density is likely to be real and associated with the QSOs at the 99.5 per cent confidence level. The reason that this random field test does not replicate the confidence level suggested by Poisson statistics is that in reality galaxies are clustered, and so the probability of finding a second galaxy is not mutually exclusive of finding the first as is assumed by the Poisson distribution. It is worth noting that if a more simplistic colour cut

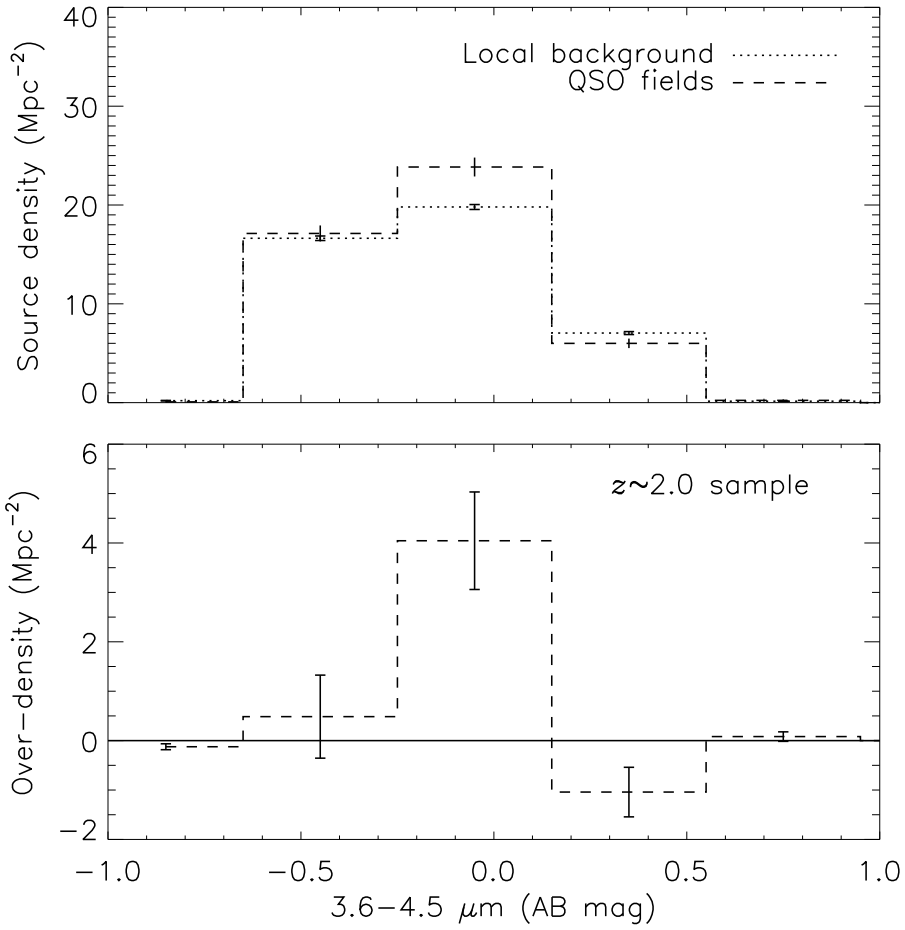

Figure 3.9: Histograms showing the IRAC 3.6-4.5 μm colour of sources around the QSOs in the $z \sim 2.0$ sample. In the top panel the dotted line shows the averaged local background source density surrounding the QSOs and the dashed line shows the averaged source density inside the first annulus surrounding these QSOs. The bottom panel shows the result of subtracting the local background from the source density in the first annulus. The remaining excess is consistent with the choice of colour cut and with being at the redshift of the QSOs as predicted by the models in Section 3.4.2.

$-0.25 <$ 3.6-4.5 μm is used to remove only foreground galaxies, a 2.8 σ (Poisson) over-density still remains.

Physically, the over-density in the first annuli of these QSOs including a correction for completeness corresponds to on average 7-10 galaxies, taking into account the 1σ errors, that are brighter than $\sim 0.7L_*$ at this redshift (assuming the chosen models). This number is in excess of the local field level and projected to be within $\sim$ 700 kpc of the QSOs.

3.5.2 $z \sim 3.3$ Sample

In the bin that spans the redshift range $2.8 < z < 3.8$ there are 11 SDSS QSOs. Using Figs. 3.3 and 3.4, colour cuts are again experimented with, as in Section 3.5.1, using the Monte-Carlo method. The results of this analysis are given in Table 3.2 which shows that a colour criterion of $0.20 <$ 3.6-4.5 μm < 0.45 provides the largest over-density. Again to minimise contamination from the foreground, all sources detected in the r-band with an apparent magnitude brighter than 23.5 are removed. In this redshift range this criterion corresponds to cutting objects that are $\sim$ 4 L_* or brighter, according to the choice of models, ensuring once again only the rarest galaxies associated with the QSOs are excluded, if any. The flux at which the data is 50 per cent complete corresponds to an absolute 3.6 μm magnitude of -24.4 at the maximum redshift of the sample. The search around each QSO is thus restricted to galaxies brighter than this limit; the K correction is ignored within the bin as the uncertainty on this is likely as large as the correction which is $\sim$ 0.2 magnitudes in the models used. The adopted

Table 3.2: Table showing the same as in Table 3.1 but for the sample centred on $z \sim 3.3$. This is shown both for the analysis down to the conservative 50 per cent completeness limit (c50) and the 30 per cent completeness limit (c30) of the *Spitzer* data.

Lower cut	Upper cut	σ_{c50}	M-C $\%_{c50}$	σ_{c30}	M-C $\%_{c30}$
-0.10	0.30	0.94	28.50	1.29	23.00
-0.10	0.35	1.33	19.90	1.77	14.70
-0.10	0.40	1.36	18.80	1.83	14.00
-0.10	0.45	1.63	13.90	2.08	9.10
-0.05	0.30	1.17	22.10	1.49	19.40
-0.05	0.35	1.57	14.70	1.99	11.70
-0.05	0.40	1.60	13.50	2.05	11.30
-0.05	0.45	1.88	10.00	2.31	7.60
0.00	0.30	0.79	31.90	1.08	26.20
0.00	0.35	1.24	20.70	1.64	16.10
0.00	0.40	1.27	19.20	1.70	15.80
0.00	0.45	1.58	14.10	1.98	10.90
0.05	0.30	1.61	10.80	1.77	11.50
0.05	0.35	2.04	6.90	2.33	5.40
0.05	0.40	2.06	7.10	2.38	5.40
0.05	0.45	2.37	4.20	2.66	3.50
0.10	0.30	1.18	19.40	1.36	17.60
0.10	0.35	1.69	9.60	2.01	7.30
0.10	0.40	1.71	9.90	2.06	7.50
0.10	0.45	2.06	6.00	2.38	4.30
0.15	0.30	1.59	10.20	1.95	5.70
0.15	0.35	2.14	4.40	2.62	2.20
0.15	0.40	2.14	4.40	2.65	2.60
0.15	0.45	2.51	1.70	2.99	0.70
0.20	0.30	1.60	9.20	2.11	2.80
0.20	0.35	2.22	2.90	2.86	0.70
0.20	0.40	2.19	2.90	2.85	0.50
0.20	**0.45**	**2.62**	**1.10**	**3.22**	**0.10**
0.45	NA	0.46	37.80	0.23	41.70
NA	0.05	0.55	36.10	0.75	31.90

flux limit represents galaxies which are brighter than roughly $1.1L_*$ in this redshift range.

The individual histograms of source density versus radial distance for each of these 11 QSOs are shown in the top panel of Fig. 3.10. Though there are no statistically significant over-densities, many of the first annuli are more than 1 σ (given by Poisson statistics) with one 2 σ above the local background level. Looking at the individual histograms (Fig. 3.10) evidence is again found to suggest that using local background subtraction is the right approach.

The stacked source density is plotted in Fig. 3.11 which shows a clear peak in the source density projected as being within 700 kpc of the QSOs. This peak is significantly above the local background at the 2.62 σ (given by Poisson statistics). Using a global background in the stacking process has little affect on the result, only reducing the significance to the 2.55 σ level. It is found that if the search is allowed to be slightly more sensitive by going down to a flux density at which the data is only 30 per cent complete the stacked source density in this colour space becomes more over-dense improving to the 3.2 σ level, see Table 3.2. This evidence suggests that the result is likely to be real since a stronger signal is achieved despite relaxing the conservative flux cut, hence including less secure source detections.

The 3.6-4.5 μm colour space of the sources found in the local backgrounds and first annuli of this sample is shown in Fig. 3.12. Also shown is the result of subtracting the local background showing where the detected over-density lies in this colour space. There is a clear over-density at the ~ 2.6 σ level in the colour range chosen ($0.20 <$ 3.6-4.5 μm < 0.45). This is also consistent

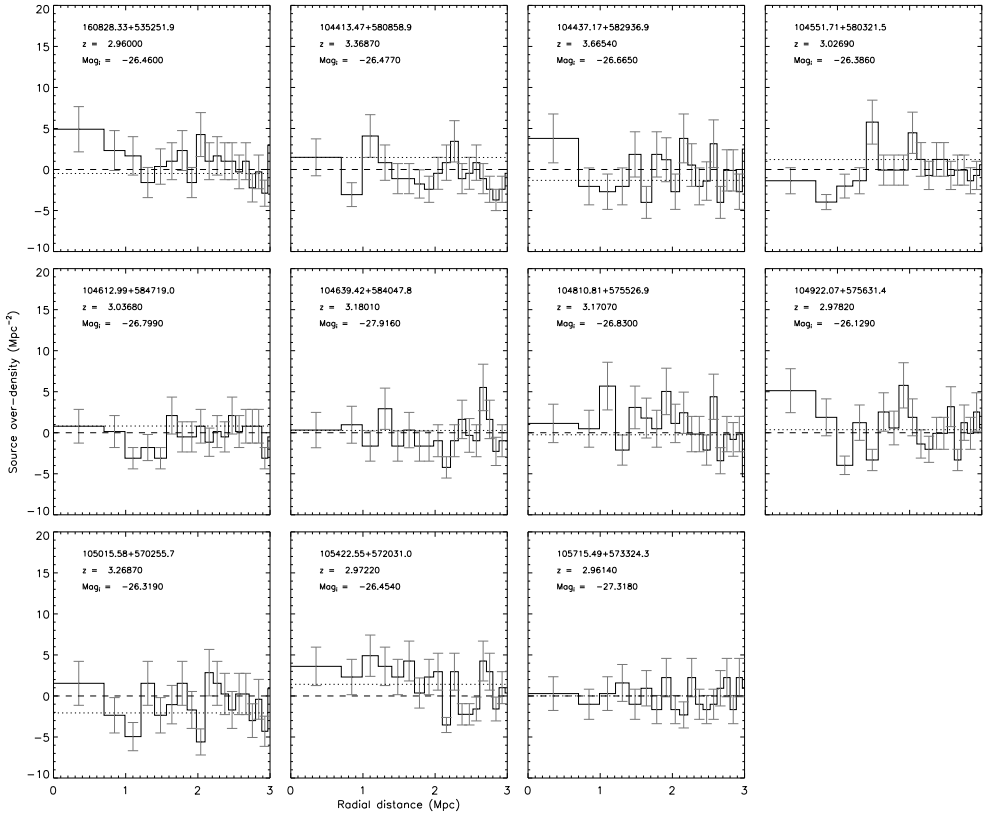

Figure 3.10: The individual source over-density versus radial distance for the 11 QSOs in the redshift range $2.8 < z < 3.8$ ($z \sim 3.3$ sample). The first bin has a projected radius of 700 kpc and the other bins cover the same projected area as the first. The error bars show the Poisson error on the raw number counts. The dashed line shows the subtracted local background level (zero level) determined from an annulus of an angular size equivalent to 2 Mpc to 400 $''$ from the QSOs. The dotted line shows, for comparison, the global background as determined by taking the average source density in large apertures over the SERVS fields. Also labelled are the QSO's redshifts and absolute SDSS i-band magnitudes. These are the source density before being corrected for completeness.

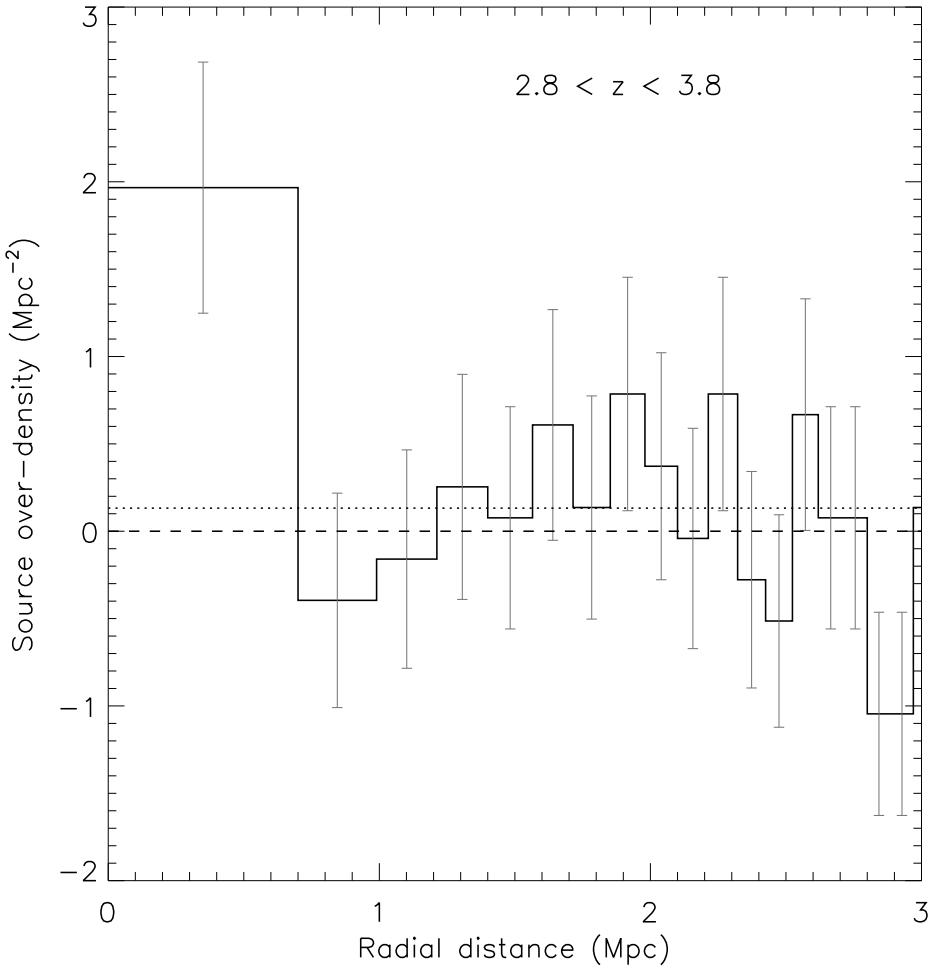

Figure 3.11: Stacked source over-density versus radial distance for the 11 QSOs in the redshift range of $2.8 < z < 3.8$ ($z \sim 3.3$ sample). The first bin has a projected radius of 700 kpc and the other bins have the same projected area as the first. The error bars show the Poisson error on the raw number counts. The dashed line shows the subtracted local background level (zero level) determined from an annulus of an angular size equivalent to 2 Mpc to 400 $''$ from the QSOs. The dotted line shows, for comparison, the global background as determined from taking the average source density in large apertures over the SERVS fields. This is the source density before being corrected for completeness.

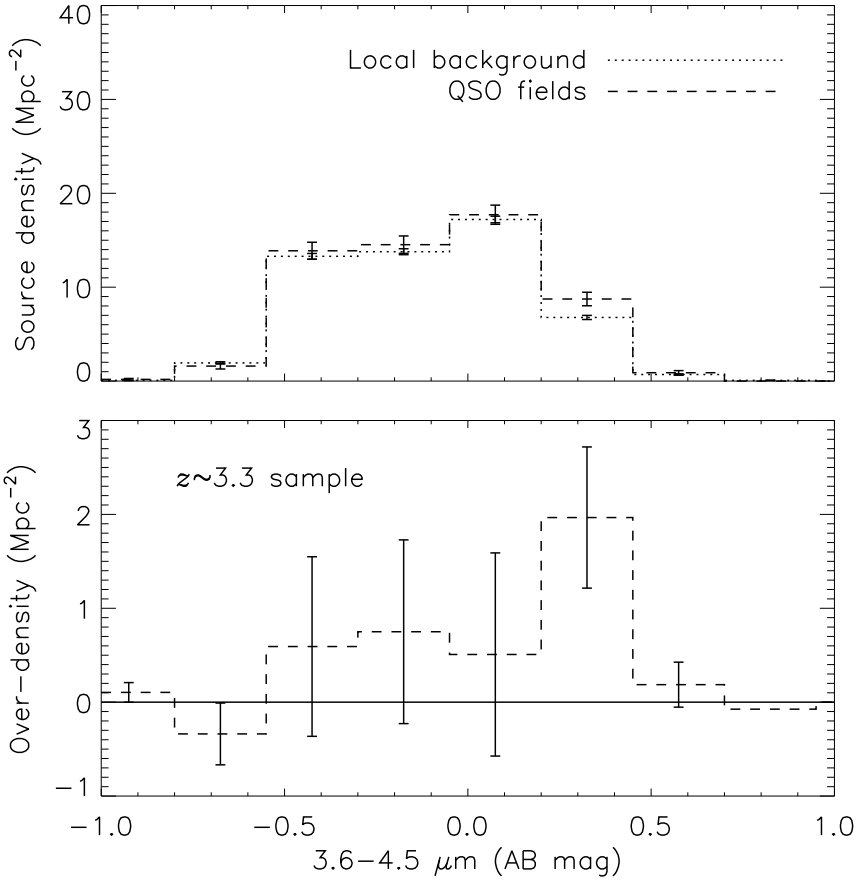

Figure 3.12: Histograms showing the IRAC 3.6-4.5 μm colour of sources in the SERVS catalogues. In the top panel the dotted line shows the average local background source density surrounding the QSOs in the $z \sim 3.3$ sample and the dashed line shows the average source density inside the first annulus surrounding these QSOs. The bottom panel shows the result of subtracting the local background from the source density first annulus. Showing that the remaining excess is consistent with the choice of colour cut and with being at the redshift of the QSOs as predicted by the models in Section 3.4.2.

with the colours expected of galaxies in this redshift range, as predicted by the models in Section 3.4.2, providing further evidence that the detected over-density is at the redshift of the QSOs in this part of the sample.

Running the Monte-Carlo code 1000 times on batches of 11 random locations, avoiding QSOs, similar sized over-densities are found only 1.1 per cent of the time in this colour space. If this is extended to all the colour space used in the analysis (see Table 3.2) then this increases to 11.9 per cent, hence a less significant excess. However, using the more sensitive 30 per cent completeness flux limit the significance improves such that in the colour space chosen a 3.2 σ over-density is only found 0.1 per cent of the time, and over all colour space this is found 5 per cent of the time.

Physically this over-density with a correction for completeness corresponds to on average 2-5 galaxies that are brighter than $\sim 1.1L_*$ (with the choice of models) in excess of the local field level around each QSO projected to be within ~ 700 kpc.

3.6 Comparison between QSOs Environments and Redshift

3.6.1 Comparison between Redshift Bins

To allow for comparison between the two sub-samples the $z \sim 2.0$ sample is re-analysed such that only galaxies with absolute magnitudes brighter than -24.4 at 3.6 μm are used. This is to match the sensitivity of the $z \sim 3.3$ sample, again neglecting the K correction which is a 0.02 magnitude effect.

In doing this 3-6 galaxies are found that are brighter than $\sim 1.1L_*$ around the $z \sim 2.0$ sample, which compares to the 2-5 galaxies found around the $z \sim 3.3$ sample. Hence the population of massive, brighter than $\sim L_*$, galaxies around the two samples seems to be comparable. This is certainly good evidence that the massive galaxies in proto-clusters are already in place by $z \sim$ 3-4, where to-date only a handful of detections have been made predominantly around individual high-z radio-galaxies (e.g., Overzier et al. 2006, 2008). This picture fits in with the idea of downsizing where massive galaxies form and cluster before those of lower mass (Cowie et al. 1996; Heavens et al. 2004).

3.6.2 Comparison with Chapter 2.

In this Section these results are compared to the work on AGN environments at $z \sim 1$ discussed in Chapter 2. The *Spitzer* data from the $z \sim 1$ sample are sensitive to galaxies with a 3.6 μm absolute magnitude of -22.9 at $z \sim 1$. The data from Chapter 2 were thus reanalysed using a projected 700 kpc annulus (to match that used on the SERVS QSOs) and restricted to flux limits which mean that the same absolute magnitude range at $z \sim 1$ is sampled as discussed here using the SERVS data.

In the environments of the $z \sim 2.0$ sample the SERVS *Spitzer* data are sensitive to galaxies with absolute magnitudes of -23.4 at 3.6 μm or brighter. To compare with the $z \sim 1$ sample a K correction of 0.4 magnitudes (from the models discussed in Section 3.4.2) is applied and hence the $z \sim 1$ data are reanalysed down to an absolute magnitude of -23.0. This gives a detection of

4-6 galaxies projected as being within 700 kpc, compared to the 7-12 around the $z \sim 2.0$ sample.

Around the $z \sim 3.3$ sample the SERVS *Spitzer* data are sensitive to galaxies with absolute magnitudes of -24.4 or brighter. Again applying a K correction of 0.4 magnitudes the $z \sim 1$ sample is reanalysed down to an absolute magnitude of -24.0. This gives 1-2 galaxies projected within 700 kpc compared to the 2-5 around the $z \sim 3.3$ sample.

At face value therefore it suggests that the number of massive galaxies found around the $z \sim 1$ sample is slightly lower. This may well be the case and would fit in with the idea of downsizing of the AGN population where AGN at higher redshift are those in bigger groups or clusters than at lower redshift (Romano-Diaz et al., 2011). Another possible scenario is that the galaxies around the AGN with $2 < z < 4$ have merged to form a more centrally peaked over-density of a smaller number of galaxies. This would explain the inability to detect the smaller scale over-density found in Chapter 2, which in terms of signal-to-noise was found to be an equally large signal to the combined large scale over-density. It is possible however, that the colour selection that is used in this chapter means that foreground contamination is more efficiently removed than in Chapter 2 and therefore leads to detecting a cleaner signal, this may go some way to explaining the difference. Additionally given the uncertainty in the K correction and errors in the completeness corrections it is difficult to say for sure if there is evidence for evolution in the environments the AGN inhabit at these epochs.

3.7 Comparison with Galaxy Formation Models

In this Section the findings of the analysis of AGN environments is compared with predictions from the Durham semi-analytic galaxy formation model of Bower et al. (2006). This model is based on the ΛCDM Millennium simulation (Springel et al., 2005). Bower et al. (2006) then populate the dark matter haloes created by the Millennium simulation with galaxies using their semi-analytic formula, Galform. The Millennium simulation is an N-body simulation consisting of a box with sides of $500/h$ Mpc in co-moving units containing 10^{10} particles of mass $8.6\times10^{8}\,\mathrm{M}_{\odot}/h$. The simulation started from an initial set of density perturbations at $z = 127$ calculated analytically, which is then allowed to evolve under the influence of only gravity to the present day. Snapshot catalogues of the structures (dark matter haloes) that formed and merged in the box were saved at 64 epochs and it is these on to which the Durham galaxies are added.

The choice of the Durham model is partly based on the fact that they give their galaxies central black hole masses (see Bower et al. 2006 for details), which are used here to compare to the QSOs, but also because it has recently been shown to be one of the best fitting models to the observed luminosity function at $z < 4$ (Cirasuolo et al., 2010). However, as with all current models of galaxy formation there are still some issues with both the faint and bright end predictions (e.g. Cirasuolo et al., 2010; Henriques et al., 2011).

In order to compare the results presented here with those predicted by the Durham simulations the model catalogues are queried for each sub-sample of

the QSOs. The model catalogues are searched for galaxies with luminosities a factor of two fainter than the *Spitzer* data is sensitive to around each redshift sub-sample. In each redshift range the model catalogues are queried at the closest snapshot to the mid-point of that redshift range. To mimic the search of AGN environments the model catalogues are searched around galaxies with black hole masses greater than three different values (M_{bh} >$10^{8.50}$, $10^{8.75}$ and $10^{9.0}$ $M_{\odot}$).

This procedure should replicate as closely as possible that performed with the AGN samples, as observing the fields around luminous high-z AGN is effectively identical to searching the environments of a subset of the largest black holes at any epoch. It is not currently possible for most of the SERVS sample to measure the black hole masses using virial methods as even the MgII line moves out of the SDSS spectral range at $z = 2.25$. However, it is known that these high luminosity QSOs must be hosted by some of the largest black holes at any given epoch.

One way to quantify this is through using Eddington arguments to place lower limits on the black hole masses of the QSOs. This was done by using the SDSS absolute i-band magnitudes with a bolometric correction of 15 (Richards et al., 2006a) and the assumption that the QSOs are accreting at the Eddington limit and so their bolometric luminosity is equal to their Eddington luminosity. This then allows for an estimate of the lower limit on the mass of black hole required to power each QSO using the relationship between Eddington luminosity and black hole mass from Rees (1984). The results of this analysis are shown on the right-hand axis of Fig. 3.2. It is worth noting that there are no black holes in the model catalogues at $z \sim 3.3$ that

have a mass $> 10^{9.25}\,\mathrm{M}_{\odot}$, hence this is why the search in the models is not extended to these values, which would better reflect the estimated values.

The full simulation box can be used for the comparison to the $z \sim 3.3$ sample, but for the lower redshift part the volume queried is restricted to a $350/h$ Mpc on a side box due to the time restriction on queries. This is not an issue, however, because at lower redshift the population of large black holes is, as would be expected, higher and so less area is required to find the same number of suitable targets. As the longest wavelength that the model produces is the K-band the modelled $K - 3.6$ μm colour from Section 3.4.2 is used to match to the model catalogue to the observations. To account for the effect of, in reality, measuring counts in a cylinder we search within our physical search radius of 700 kpc in two dimensions of the simulation and then within 3 Mpc in the third dimension. This effect as described in Yee & Ellingson (1995) was found to increase the sources detected by a factor of $\sim$1.5. The measured over-densities in the observations, which is assumed to all be associated with the QSOs, can then be compared to the number of comparable galaxies that are found in the model catalogues around similar sized black holes.

The results of this comparison are shown in Fig. 3.13 for the $1.3 < z < 2.7$ sample and in Fig. 3.14 for the $2.8 < z < 3.8$ sample. The grey shaded band shows the 1 σ error on the number of galaxies found surrounding the QSOs in each case, and the error bar shows the estimated depth of the observation in terms of galaxy absolute magnitude (model dependant due to K and colour correction). The lines then show the number of galaxies predicted by the model within the same cylindrical search area for galaxies with black hole

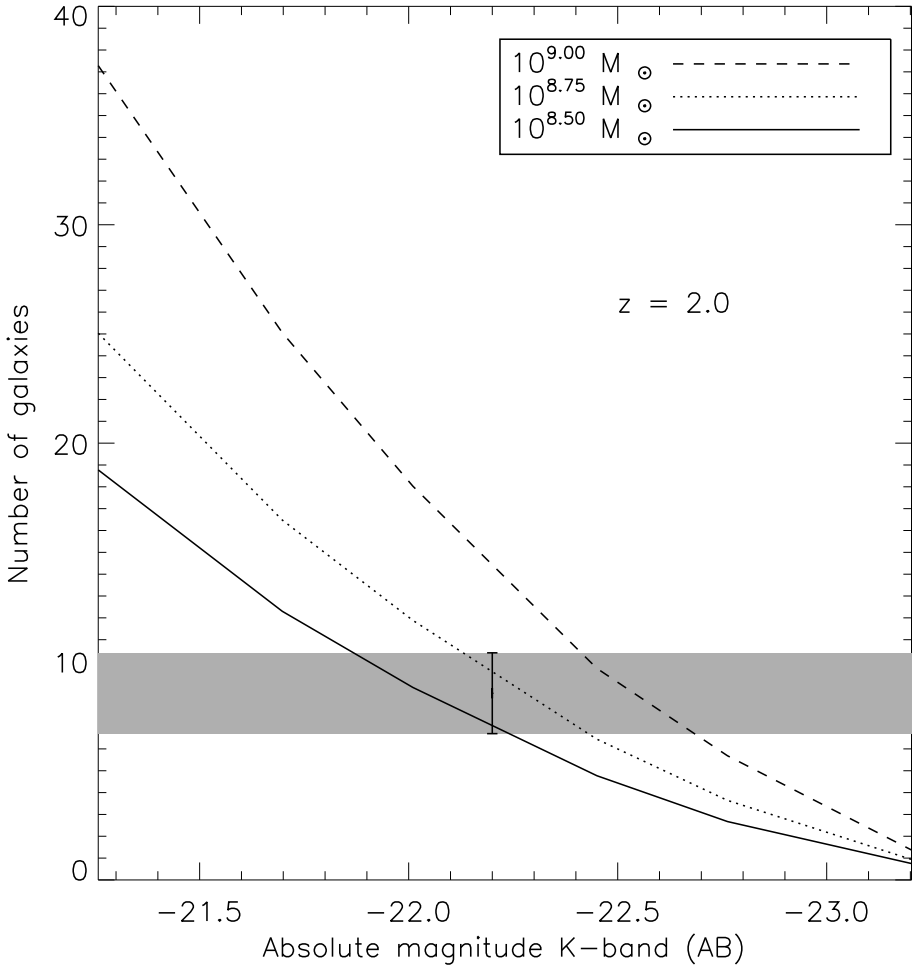

Figure 3.13: Comparison of the $1.3 < z < 2.7$ sample to the Durham model. The grey shaded band shows the 1 σ error on the number of galaxies detected surrounding the QSOs in this sample, and the location of the error bar shows the estimated depth reached in terms of galaxy luminosity (model dependant due to K and colour correction). These numbers are completeness corrected. The lines then show the number of galaxies predicted by the model within the same radius with black hole masses greater than three different values (where the solid, dotted, and dashed lines represent $10^{8.50}$, $10^{8.75}$ and $10^{9.0}\,\mathrm{M}_\odot$ black holes respectively).

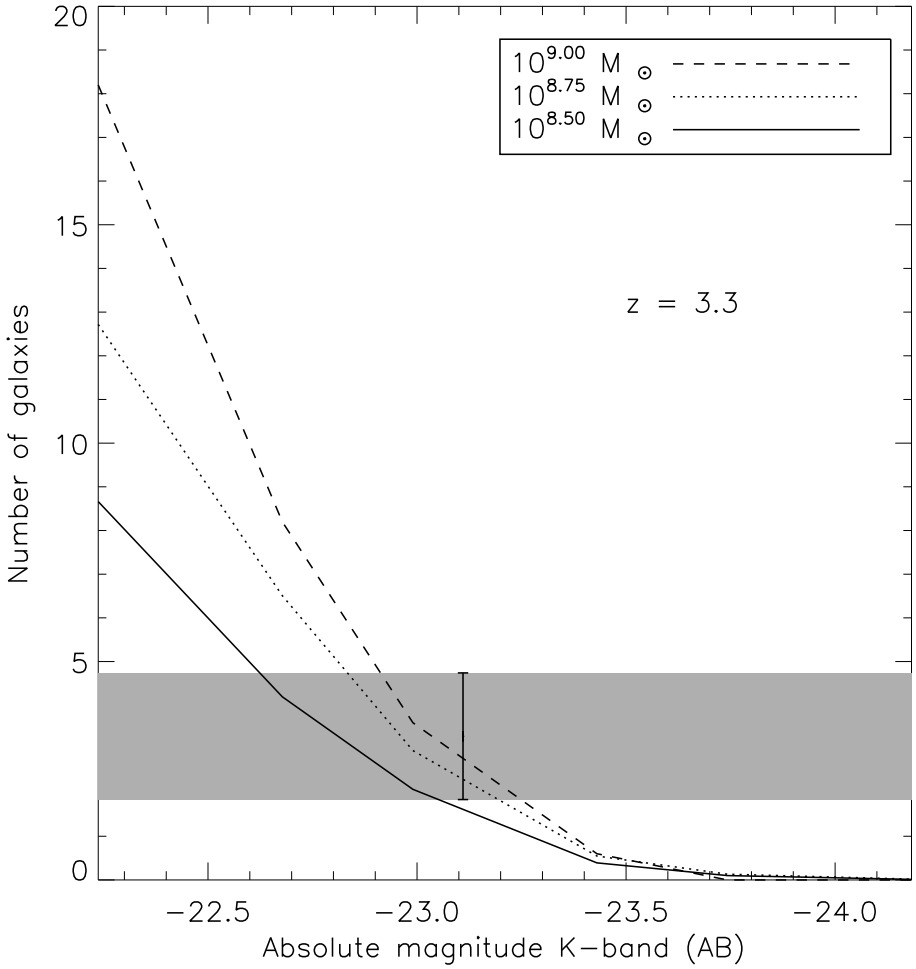

Figure 3.14: Comparison of the $2.8 < z < 3.8$ sample to the Durham model. The grey shaded band shows the 1 σ error on the number of galaxies detected surrounding the QSOs in this sample, and the location of the error bar shows the estimated depth reached in terms of galaxy luminosity (model dependant due to K and colour correction). These numbers are completeness corrected. The lines then show the number of galaxies predicted by the model within the same radius with black hole masses greater than three different values (where the solid, dot, and dashed lines represent $10^{8.50}$, $10^{8.75}$ and $10^{9.0}\,\mathrm{M}_\odot$ black holes respectively).

masses greater than three values.

Interestingly, in both cases the detected source density matches well with the predictions of the models. In the $z \sim 2.0$ redshift bin the model predictions for the $10^{8.50}$ and $10^{8.75}\,\mathrm{M}_{\odot}$ black holes fall within the 1 σ error bars of the observed source density. In the $z \sim 3.3$ redshift bin the model predictions for the $10^{8.75}$ and $10^{9.00}\,\mathrm{M}_{\odot}$ black holes fall within the 1 σ error bars of the observed source density. It is worth noting that interestingly the estimates of the black hole masses for the $z \sim 3.3$ part of the sample are on average higher due to the higher average QSO luminosities at these redshifts. This may well be reflected in how they compare to the model predictions

3.8 Summary

In this chapter a study of the environments of SDSS QSOs in the deep SERVS survey using data from *Spitzer*'s IRAC instrument at 3.6 and 4.5 μm is conducted. The analysis concentrates on the high redshift QSOs in the sample as these have not previously been studied with statistically large samples or with data of this depth. These are highly luminous QSOs ($M_i \lesssim -26$) and hence harbour massive black holes ($M_{bh} \gtrsim 10^8\,\mathrm{M}_{\odot}$). In contrast, the environments of lower redshift QSOs have been studied in detail with a much larger sample in Chapter 2. The $z > 1$ QSOs are split into two sub-samples depending on their redshift which allows different source selection criteria to be applied to each redshift sample. The criteria applied are a combination of an IRAC 3.6-4.5 μm colour selection and a cut of sources detected above a certain brightness in the ancillary r-band data from the INT.

Using this method a significant ($> 4\sigma$) detection of an over-density of galaxies around the QSOs in the sub-sample centred on $z \sim 2.0$ and ($> 2\ \sigma$) in the sub-sample centred on $z \sim 3.3$ is found. This provides further evidence that high luminosity AGN can be used to trace clusters and proto-clusters at these epochs. The number counts of L_* or brighter galaxies around each sample are counted and found to be comparable, suggesting the massive galaxies in proto-clusters are in place by $z \sim 3-4$ which is consistent with the idea of downsizing. These findings are then compared to those in Chapter 2 at $z \sim 1$ and it is found that the over-densities found in this chapter are slightly larger ($\sim$ factor of two) than those found in Chapter 2. Also the smaller scale (300 kpc) over-density seen in Chapter 2 is not observed around this sample. These points may be evidence of downsizing of the AGN host population or that the galaxies seen around the higher-z AGN have merged forming a smaller but more compact over-density by $z \sim 1$. However, it is possible that the colour selection used in this work allows for a more efficient detection of possible companion galaxies and combined with the uncertainties involved in making the comparison it is possible the numbers are broadly consistent.

Finally the results are compared to the predictions from the Durham (Bower et al., 2006) galaxy formation model GALFORM, built on top of the MILLENNIUM simulation (Springel et al., 2005) dark matter halo catalogues. In both cases the model predictions are within the 1 σ error bars of the measured source densities from this chapter. This suggests that broadly speaking the models are producing the right kind of environments for black holes large enough to host the QSOs studied in this chapter.

Chapter 4

Far-Infrared Environments of QSOs using the *Herschel*-ATLAS

4.1 Introduction

In this chapter, data from the *Herschel*-Astrophysical Terahertz Large Area Survey (H-ATLAS; Eales et al. 2010) using the *Herschel* space telescope (Pilbratt et al., 2010) are used to study the far-infrared (FIR) environments of a large sample of SDSS and 2SLAQ type-1 QSOs. This extends the work conducted in the previous chapters studying the environments of these objects with the rest-frame optical emission, hence probing stellar mass, to instead look for dusty star-forming galaxies in the QSOs' environments.

4.2 Data

The data used in this chapter are FIR imaging from the phase 1 data release of the H-ATLAS survey, using the recently launched *Herschel* Space Telescope. These data consist of observations using both imaging cameras on *Herschel* at five wavelengths from 70 to 500 μm and reach a 5 σ depth of $\sim$ 33.5 mJy/beam at 250 μm. Details of the images and catalogues created as part of the science demonstration phase (SDP) of the survey are given in Pascale et al. (2011) and Rigby et al. (2011) respectively. The cross ID process used for the available multiwavelength data is described in Smith et al. (2011). In this work the phase 1 H-ATLAS catalogues are used which currently cover the H-ATLAS/GAMA 9hr, 15hr and about half the 12hr fields. The catalogues contain sources detected at $> 5\sigma$ in at least one band (either 250, 350, or 500 μm) of the Spectral and Photometric Imaging Receiver (SPIRE, Griffin et al. 2010) data, as these data are the deepest of the H-ATLAS survey. The area covered by the phase 1 data is currently approximately 90 sq. degrees.

In Fig. 4.1 the sensitivity of H-ATLAS is shown in terms of the SFR that can be detected at different redshifts assuming a simple modified black body to describe the FIR SED of galaxies with a temperature of 26 K and dust emissivity index of $\beta = 1.5$ (described further in Section 4.4.5). This figure shows that if these assumptions are appropriate it should be possible to detect galaxies with SFRs of $\sim$ 100 $M_{\odot}yr^{-1}$ (*i.e.* Luminous-Infrared-Galaxies, LIRGS) out to $z \sim 1$ and those with $\sim$ 1000 $M_{\odot}yr^{-1}$ (*i.e.* Ultra-Luminous-Infrared-Galaxies, ULIRGS) out to $z \sim 2$. This means in the

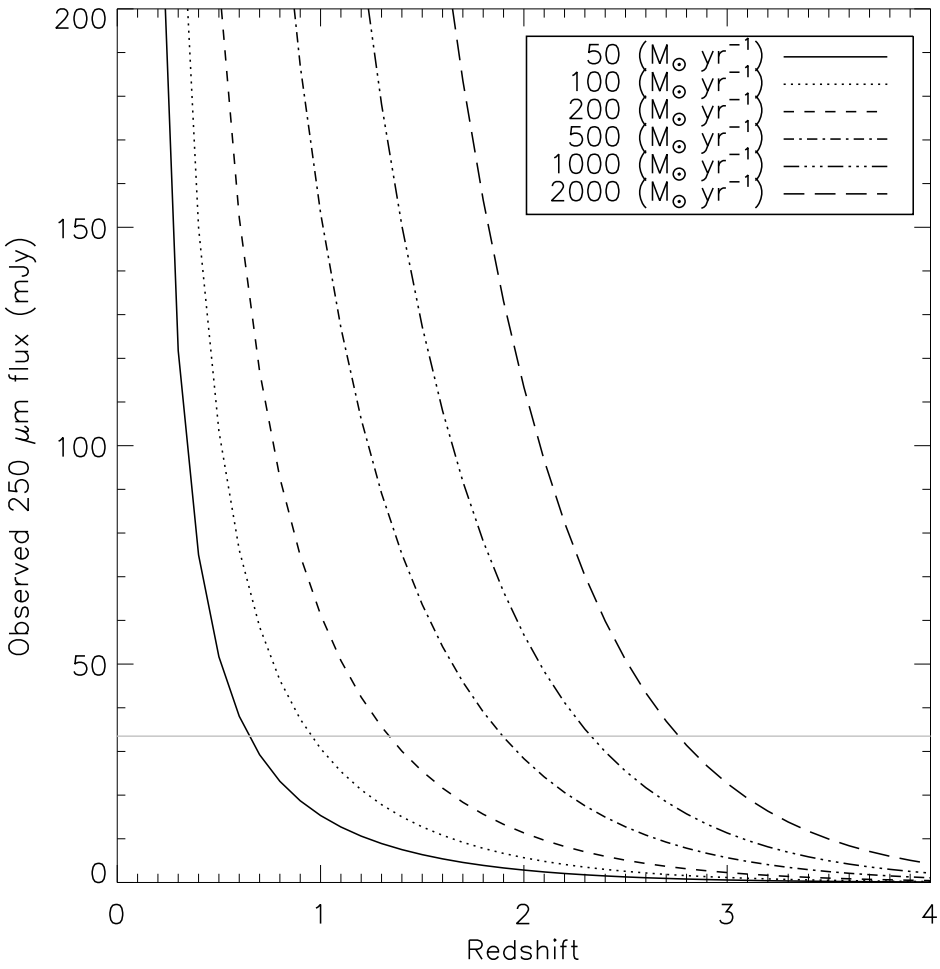

Figure 4.1: H-ATLAS survey sensitivity in terms of the SFR that can be detected at a given redshift. The different lines show different SFRs and the 250 μm flux they will have between $0 < z < 4$. The conversion between flux and SFR assumes a simple modified black body for the FIR SED of galaxies with a temperature of 26 K and dust emissivity index of $\beta = 1.5$; full details are given in Section 4.4.5. The horizontal grey line shows the 5σ sensitivity of H-ATLAS at 250 μm (33.5 mJy).

range $0.0 \lesssim z \lesssim 2.0$ the survey should be sensitive to the kinds of galaxy that were detected by SCUBA in Stevens et al. (2010) around slightly higher redshift AGN.

4.3 QSO Sample

Broad-line (type-1) QSOs are identified in the phase 1 region of the H-ATLAS survey by matching the area covered by H-ATLAS source catalogues firstly with the seventh data release of the SDSS quasar survey (Schneider et al., 2010). This was achieved using the software package TOPCAT (Taylor, 2005) and allows SDSS QSOs in the overlap regions with H-ATLAS to be selected. In addition to this sample of QSOs some of the H-ATLAS phase 1 region (parts of the 9 and 15hr fields) are covered by the the 2dF-SDSS LRG and QSO (2SLAQ) survey (Croom et al., 2009), which targets the faint end of the broad-line QSO population, and so QSOs are also selected in the overlap with this catalogue.

2SLAQ uses the same SDSS photometry and similar colour selection techniques but gained spectroscopic follow up of potential QSOs down to an $i_{mag} = 22.0$ compared to the $i_{mag} = 19.0$ used in SDSS quasar survey. The apparent i-band magnitudes given in the 2SLAQ catalogue were corrected for extinction using the values in the catalogue and then transformed into rest-frame i-band using a K correction for QSOs of the form $K_{corr} = -2.5(\alpha + 1)\log_{10}(1 + z)$ (Wisotzki, 2000) where the spectral index $\alpha = 0.5$. These were then converted to absolute magnitudes which can then be directly compared to the Mi magnitudes given in the SDSS quasar cata-

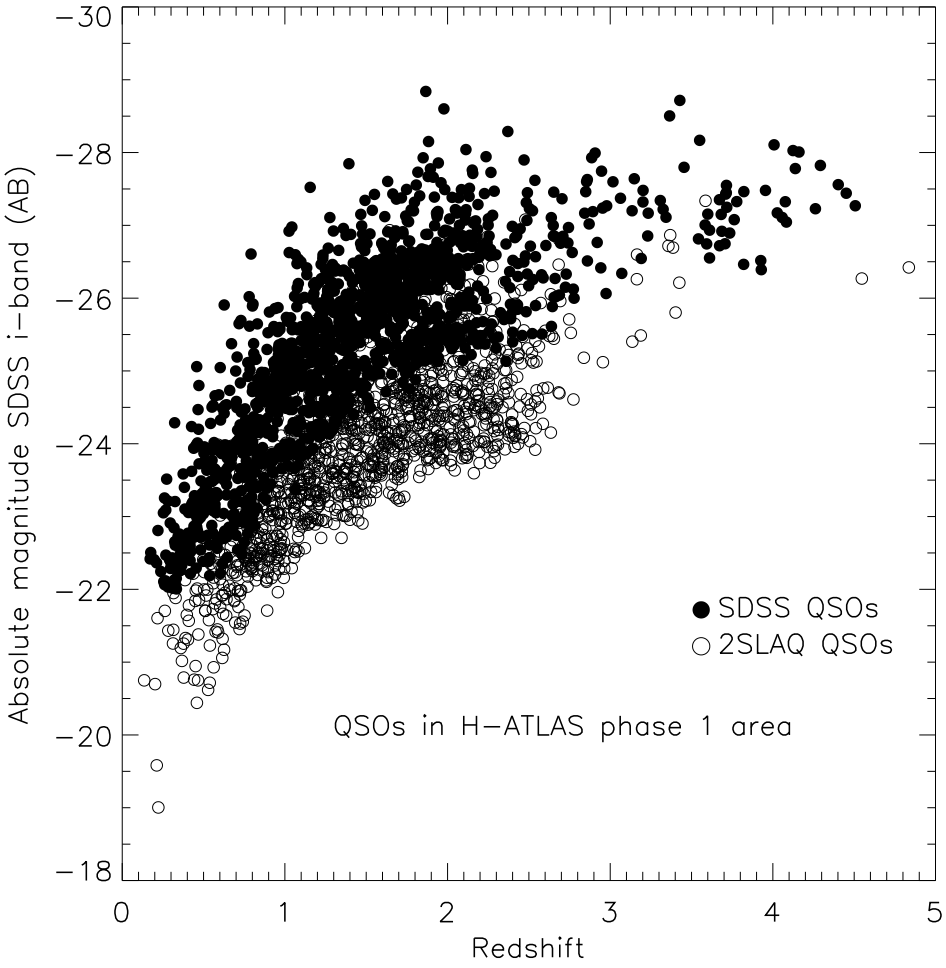

Figure 4.2: Redshift versus optical absolute magnitude (SDSS i-band) for the QSOs in the H-ATLAS phase 1 data. SDSS QSOs are shown with filled symbols and 2SLAQ QSOs are shown with open symbols.

logue.

Once the QSO catalogues were roughly cut to match the region surveyed by the phase 1 H-ATLAS data it was ensured that all QSOs were at least 4 Mpc (at their redshifts) from the edges of the H-ATLAS maps; this provides ample area with which to determine a local background source density. The distribution in the L-z plane of these two samples of QSOs is shown in Fig. 4.2. In total there are 1431 QSOs from SDSS and 1257 from 2SLAQ in the region contained in the phase 1 data, 2136 of these are below $z = 2$.

4.4 Analysis

4.4.1 Environment Stacking

A stacking technique similar to that used in the previous chapters is used to look for a statistical over-density of galaxies in the environments of the QSOs in sample. Over-densities around the QSOs are searched for in two ways, firstly by counting sources in the H-ATLAS 5 σ catalogues and secondly, to allow a more sensitive search than possible with the catalogues, by adding up the flux in the maps around the QSOs. Both methods search within an angular distance equivalent to 1 Mpc at the QSOs' redshifts.

The uncertainty in the position of a 5 σ source at 500 μm is given by 0.6 $(\mathrm{S/N})^{-1}\times$ FWHM (Ivison et al., 2007) where the FWHM = 35.15 $''$ at 500 μm thus giving a 4.2$''$ uncertainty. Therefore any source which is within 10$''$ or any flux extracted from the map within 30$''$ of the QSOs' SDSS coordinates is not counted and this should conservatively exclude any

QSOs which are detected by H-ATLAS, the inclusion of which would bias the search for an over-density. This procedure is especially necessary as ~ 8 per cent of the QSOs in the SDP field were found to have been detected in the SDP catalogue (Bonfield et al., 2011).

4.4.2 Background Level

To measure the background level of sources, a local background is adopted as this has previously been shown to be the best measure for this kind of analysis (Falder et al., 2011). The local background is determined by placing an annulus around each QSO with an angular size equal to 2-4 Mpc at each QSO's redshift. As mentioned when selecting the sample it was ensured that each QSO was far enough inside the H-ATLAS maps to allow its environment to be searched out to at least 4 Mpc at their redshift.

In addition the results are compared with those obtained using a global background determined from large 1 degree radius apertures on the H-ATLAS catalogue and computing the average source density of these.

4.4.3 Source Number Density Results

As a first pass to see if it is possible to detect an over-density around this QSO sample in the H-ATLAS data, the sources found around all the QSOs with $z < 1.5$ (1399 QSOs) are simply stacked together and compared to the stacked local background. The result is an excess source density around the QSOs positions above the local background measure of 0.0080 ± 0.0027 sources per arcmin^{-2} which is a $\sim 3\ \sigma$ over-density; this equates to roughly

Table 4.1: Table showing the over-density of FIR galaxies around the QSO sample split into eight course redshift bins. Columns show the redshift range of each bin, the number of QSOs, mean redshift, the excess number of galaxies per arcmin^2 as well as the excess number of galaxies per field and the Poisson significance of this excess. All numbers quoted have the corrections applied for flux boosting and incompleteness from Rigby et al. (2011).

z	QSOs	$< z >$	Over-density (N/arcmin)	Over-density (N)	σ
0.0 - 0.5	138	0.37	0.013 ± 0.006	0.51 ± 0.24	2.1
0.5 - 1.0	524	0.78	0.010 ± 0.005	0.18 ± 0.08	2.1
1.0 - 1.5	738	1.25	0.007 ± 0.005	0.09 ± 0.06	1.5
1.5 - 2.0	737	1.74	0.003 ± 0.005	0.03 ± 0.06	0.5
2.0 - 2.5	402	2.20	-0.005 ± 0.006	-0.07 ± 0.08	-0.8
2.5 - 3.0	85	2.68	-0.021 ± 0.012	-0.30 ± 0.17	-1.8
3.0 - 3.5	25	3.25	0.030 ± 0.024	0.49 ± 0.38	1.3
3.5 - 4.0	25	3.71	-0.007 ± 0.020	-0.13 ± 0.36	-0.4

one excess source for every seven QSOs.

Taking account of the incompleteness of the H-ATLAS data using the completeness and flux boosting corrections for point sources provided in Rigby et al. (2011) this becomes one excess source around every six QSOs. Using the global background measure returns essentially the same numbers. Reducing the search radius to 500 kpc and increasing it to 1500 kpc was also tried; the former reduced the statistical significance of the excess presumably due to increasing Poisson noise on even smaller numbers and the latter caused a slight reduction in the significance which is probably due to watering the excess down by including a larger area without the same proportional gain in the number of excess galaxies.

To address the question of whether Poisson statistics are on their own appropriate for measuring the significance of this over-density a Monte-Carlo simulation was conducted. This involved re-running the same experiment

1000 times but each time using a QSO catalogue where the positions were randomly generated. The results of this analysis show that $\sim 3\,\sigma$ over/under-densities occur only ~ 1 time per 1000 runs suggesting that this over-density is significant at the $\sim$ 99.9 per cent level. This is close to what Poisson statistics predict and much closer than was found using near-infrared data from *Spitzer* in Chapter 3.

This experiment suggested that it is indeed possible to detect an excess, albeit small, of FIR galaxies around the QSOs in the H-ATLAS data. However it covered a broad range of redshifts ($0 < z < 1.5$) and QSO luminosities so it might be expected that these average numbers do not apply universally across this range of redshift or luminosity either because at low z we can detect lower SFRs or because all the star formation is occurring around the high z part of the sample. Therefore the same experiment was conducted again, this time splitting the QSOs in the sample with $z < 4.0$ into smaller redshift bins of width 0.5. The results of this analysis are shown in Table 4.1, which shows that most of the over-density lies in the lower redshift parts of the sample and in fact the level of over-density decreases with increasing redshift, excluding the two very high redshift bins.

The most statistically significant over-densities (2.1 σ) are in the two bins with $0.0 < z < 1.0$, the over-density in the higher of these bins is smaller than in the lowest z bin but the reduced Poisson error from having more QSOs (524 versus 138) leads to a equally significant detection. This effect also explains the increased significance (3.2 σ), despite having a smaller excess (0.0080 sources per arcmin^{-2}) of the combined over-density around QSOs with $z < 1.5$. It is intriguing although not statistically significant that the 25

QSOs with $3.0 < z < 3.5$ have the second largest excess number of sources in their environment. This is likely just down to the large Poisson error but could be tested with the full H-ATLAS survey which will give a factor of around three more SDSS and 2SLAQ QSOs in this redshift range.

The general picture then is that when looked at as a statistical population a large population of galaxies with high SFRs is not seen around the QSOs in the sample. Instead a small excess is found representing on average one galaxy with a high SFR in the environment of one in six QSOs. Around the lowest redshift QSOs this increases to one excess galaxy around two QSOs, or to put it another way half of these QSOs have a FIR bright companion galaxy. Considering the detection rate for the QSOs in the sample is only around 5-10 per cent (Bonfield et al., 2011) this is perhaps not surprising as it is likely most galaxies are simply not luminous enough in the FIR to be detected.

These numbers are, however, much lower than the detected number found by SCUBA at higher redshift, where almost all the AGN fields studied contained multiple galaxies with extreme SFRs. Galaxies with SFRs of the like would be detectable in the H-ATLAS data if they were there around these QSOs. In relation to the over-density of SMGs around more typical QSOs reported by Stevens et al. (2010), H-ATLAS is not quite sensitive enough in the same redshift range when using a modified black-body SED model with temperature = 26 K and $\beta = 1.5$ to say if these kind of excesses are present around this QSO sample. However, the same kinds of excess can be ruled out for galaxies with significantly warmer SEDs ($\sim$ 46 K) as this increases the sensitivity to star formation in the redshift range studied here.

It should of course be understood that the reported over-densities are the statistical mean values of the population and it is possible and probably likely that multiple excess galaxies are found around a smaller number of the QSOs. This will be looked at further in Section 4.4.7. In the following Sections the nature of the galaxies that make up the small excess that is found around this QSO sample is explored.

4.4.4 Fluxes of the Excess Galaxies

Even though it is not possible to know which sources in the H-ATLAS catalogue are making up the excess, it is possible to look for a statistical excess in their distribution of fluxes. This was done by binning up the fluxes in both the QSOs' environments and the background regions. The number counts in each case were then normalised to the area surveyed and the background number counts were subtracted from the environment counts. The error bars on the resulting histogram are the Poisson errors on the QSO environment and background number counts added in quadrature.

The locations of the excesses in Table 4.1 in flux space are shown in Fig. 4.3, using flux bins that are 10 mJy wide. This analysis shows firstly that the excess of sources around QSOs with $0.0 < z < 1.0$ lies in the range of $20 \lesssim S_{250} \lesssim 60$ mJy and that most of the excess for QSOs with $1.0 < z < 1.5$ is at $\sim$ 50-60 mJy. There is also an excess of sources at $\sim$ 40-50 mJy and slightly below the flux limit around the QSOs in the redshift range $1.5 < z < 2.0$. The highest three redshift bins suffer badly from small number statistics as the total number of excess galaxies around these QSOs is

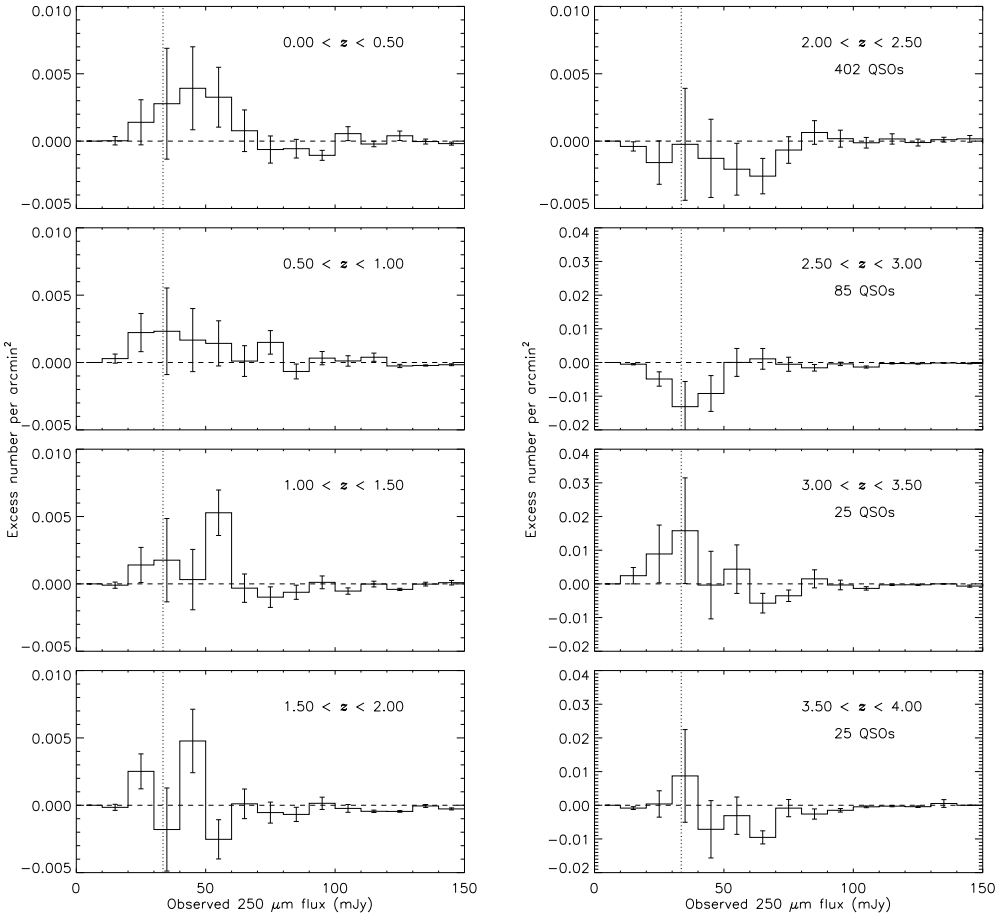

Figure 4.3: Over-density of galaxies in flux space around the QSOs in the redshift bins used in Table 4.1 created by subtracting the number counts in the local backgrounds from those in the environments. Sources are binned by their 250 μm flux in 10 mJy bins and the counts are corrected for flux boosting and incompleteness using the correction from Rigby et al. (2011). It should be noted that the three highest redshift bins have a different scale due to the large error bars resulting from small number statistics. Error bars are Poisson, generated by adding in quadrature the error bars on the environment and background histograms. The vertical dotted line represents the 5 σ flux limit of the H-ATLAS data at 250 μm, hence bins left of this line are likely incomplete.

down to a handful at most. The over-density found around the $3.0 < z < 3.5$ QSOs is all found near the surveys flux limit as would be expected if it were indeed a real excess. The statistics in these high z bins would be cleared up with more QSOs which the full H-ATLAS survey will provide.

An interesting feature in some of the redshift ranges is that the bins at and slightly below the 250 μm 5 σ flux limit are not dominating the detected excess as would be expected from steep number counts at faint fluxes. This could just be down to small number statistics and other errors or alternatively may suggest that the QSOs environments do not contain galaxies with FIR luminosities below a certain value, this would clearly be an interesting result but more QSOs would be needed to confirm or disprove this hypothesis. Again the full H-ATLAS survey will provide about three times as many QSOs than available in the phase 1 release used here in due course.

4.4.5 Star Formation Rates

Galaxies detected by *Herschel* are mostly star-forming galaxies as the FIR emission from galaxies is dominated by reprocessed light from star formation, predominantly the UV emission from short lived massive O and B stars. It is interesting therefore, to estimate the star formation rate (SFR) of the galaxies detected in the QSOs environments. To do this, first their total far-infrared luminosity (L_{FIR}) must be estimated which is the total emission produced by the dust component of the galaxy. This can then be used to estimate their SFR using the relation from Kennicutt (1998) for dusty star-burst galaxies.

This relation has the form

$$\mathrm{SFR}(\mathrm{M}_{\odot}\ \mathrm{yr}^{-1}) = 4.5 \times 10^{-44} \mathrm{L}_{\mathrm{FIR}}(\mathrm{ergs\ s}^{-1}) \tag{4.1}$$

where L_{FIR} is defined as the integrated rest-frame emission between 8 and 1000 μm.

To estimate the L_{FIR} an SED is fitted to the detected galaxies which can then be integrated beneath. A modified black-body was used, as this avoids any comparison to a potentially atypical source or unsuitable template library. The grey body was parametrised using a dust temperature of 26 K and a dust emissivity index (β) of 1.5 as this has been shown by Dye et al. (2010) to be the median fit for a sample of 1688 $z < 0.5$ H-ATLAS galaxies. It is worth noting that while varying β between $1.0 < \beta < 2.0$ has little effect on the SFR (factor of ~ 1.5 at most; see Fig. 4.4) varying the temperature between $16\ K < T < 46\ K$ can change the resulting SFR by a factor of up to ~ 7 for $0.5 < z < 1.5$ and more outside this range as shown in Fig. 4.5.

If the redshift of a H-ATLAS galaxy was known then the SED could be redshifted and normalised with one or more observed flux measurements. It could then be converted from flux units to luminosity using the luminosity distance of the galaxy. The slight complication in this process is that the over-density found here, as explained in Section 4.4.1, is a statistical excess in the number counts of sources, it is not known exactly which sources are making up the excess. Therefore the specific fluxes and redshifts of any of the galaxies that are detected in the QSOs environment are not known. However, as an excess in the flux space distribution of sources has been detected near

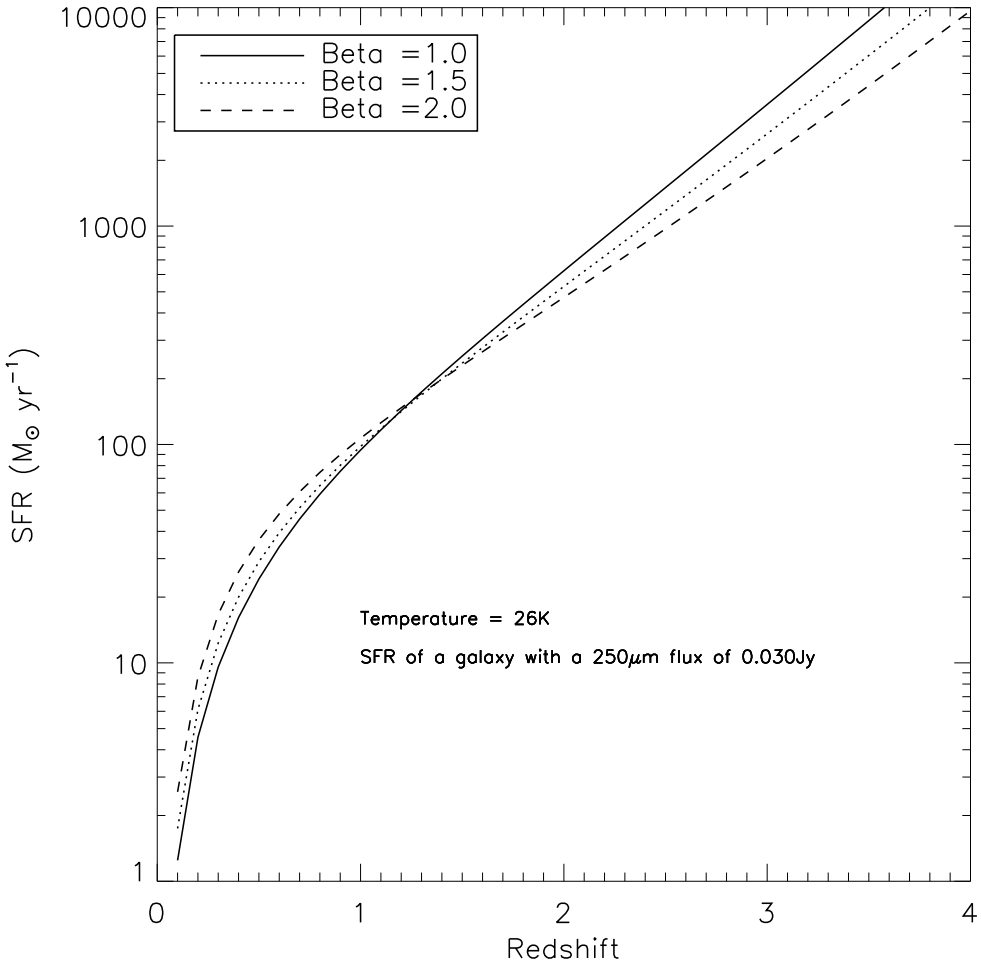

Figure 4.4: The SFR calculated using Kennicutt's relation (equation 4.1) for a modified black-body SED with a temperature of 26 K and three different values of $\beta = 1.0, 1.5$ and 2.0. The SED is normalised to have a 250 μm flux of 0.030 Jy.

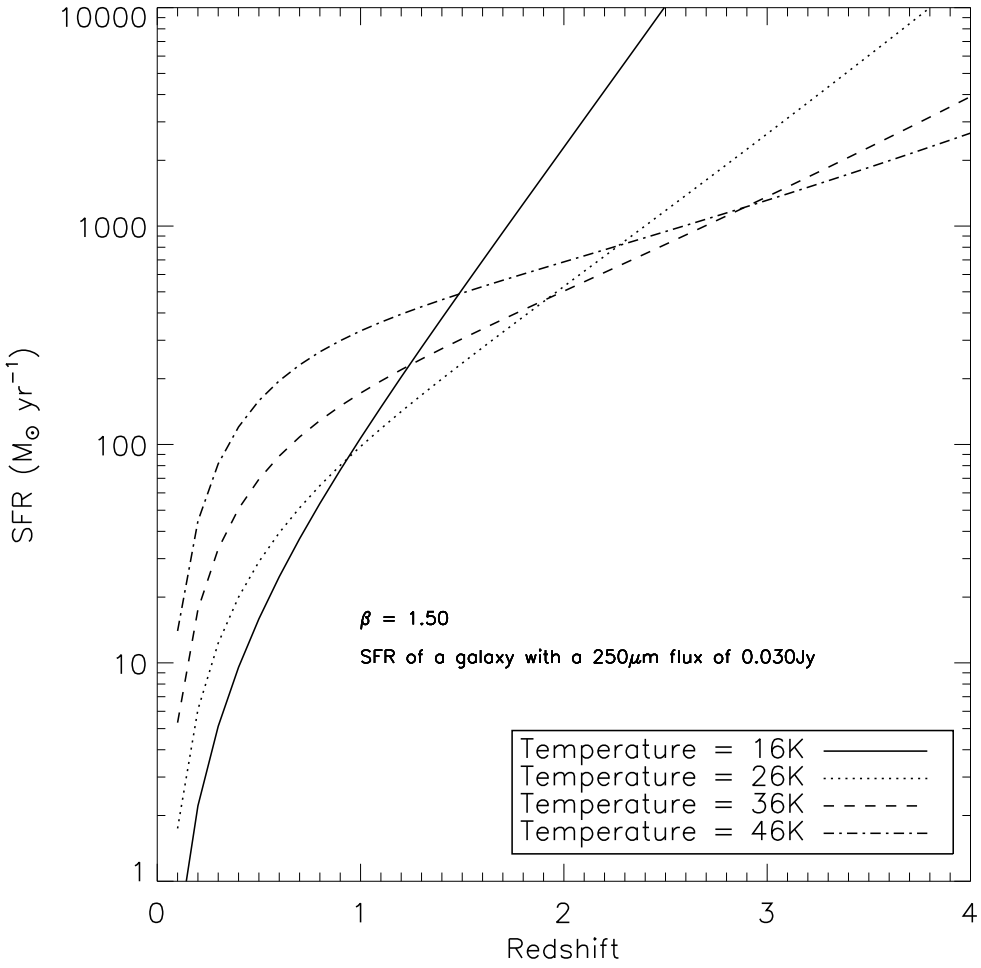

Figure 4.5: The SFR calculated using Kennicutt's relation (equation 4.1) for a modified black-body SED with a $\beta = 1.5$ and four different values of temperature $= 16, 26, 36$ and $46\ K$. The SED is normalised to have a 250 μm flux of 0.030 Jy.

the QSOs compared to those detected in the backgrounds (Fig. 4.3) it is possible to know the flux distribution of the over-densities. As the excess is associated with the QSOs' positions the implication is that these sources are at the QSOs' redshifts and so it is appropriate to use the accurately determined spectroscopic redshifts of the QSOs, from 2SLAQ or the SDSS, to redshift the SED and convert it from flux units to luminosity.

The excess galaxies SFRs were estimated therefore by taking every source detected around a QSO or in its background annulus and calculating the SFR it would have if it were assumed to be at the QSOs redshift. Obviously these SFRs will only be correct for galaxies that are actually at the assumed redshift, but those that are not correct should be removed statistically by subtracting the SFRs determined for sources in the backgrounds. This should work because the aim of the background annulus is to provide a set of sources which as closely as possible shares the same properties as the sources projected in the vicinity of the QSOs on the sky that are not actually in their environments. Therefore the distribution of redshifts of the background sources and hence non-correct SFRs will be the same in the background annulus as in the environment.

As for flux in Fig. 4.3, the SFRs were binned up in both the environments and backgrounds, normalised to the area surveyed and then the local background number counts were subtracted from the environment counts. The most obvious explanation for any excess that remains therefore seems to be that it is made up of those galaxies associated with the QSOs and that these are real SFR estimates for them. Only the 250 μm flux measurements were used to normalise the SEDs as not only are these the most sensitive they are

also the best constrained and $\sim$ 93 per cent of the H-ATLAS sources have fluxes detected with a S/N of > 5 σ and virtually all with a S/N of > 2 σ at 250 μm.

The results of applying this technique on the QSOs with $z < 2.5$ using the redshift bins from Fig. 4.3 is shown in Fig. 4.6. This shows the over-density detected in the number counts split into SFR bins of width 50 $M_{\odot}yr^{-1}$ for the QSOs with $z < 1.5$ and 200 $M_{\odot}yr^{-1}$ for the higher redshift QSOs. It appears that the estimated SFR of the excess galaxies found around these QSOs increases with redshift. In the lowest redshift bin $0.0 < z < 0.5$ there is a $\sim$ 2 σ excess of galaxies with SFRs of < 50 $M_{\odot}yr^{-1}$ and no excess of galaxies with higher SFRs. However in the bin with $0.5 < z < 1.0$ there is a slight excess (1 σ) of galaxies with SFRs of < 100 $M_{\odot}yr^{-1}$ but a $\sim$ 2 σ excess of galaxies with SFRs of 100-150 $M_{\odot}yr^{-1}$. In the redshift bin with $1.0 < z < 1.5$ there is a > 2 σ excess of galaxies with SFRs of 200-250 $M_{\odot}yr^{-1}$.

Tentatively this trend continues in the highest redshift bins with a > 2 σ excess of galaxies with SFRs of 400-600 $M_{\odot}yr^{-1}$ around QSOs with $1.5 < z < 2.0$ and a positive though insignificant bump for SFRs of 1000-1400 $M_{\odot}yr^{-1}$ around QSOs with $2.0 < z < 2.5$. The two vertical dotted lines in each panel show the SFRs that the 5 σ flux limit at 250 μm corresponds to at the redshift extremes of each bin. Hence it should definitely be possible to detect galaxies with SFRs greater than the higher of these values, therefore if galaxies with the SFRs seen in the higher redshift parts of the sample existed around the lower redshift parts they should easily be detected.

In all redshift ranges there are bins with higher SFRs than over-densities

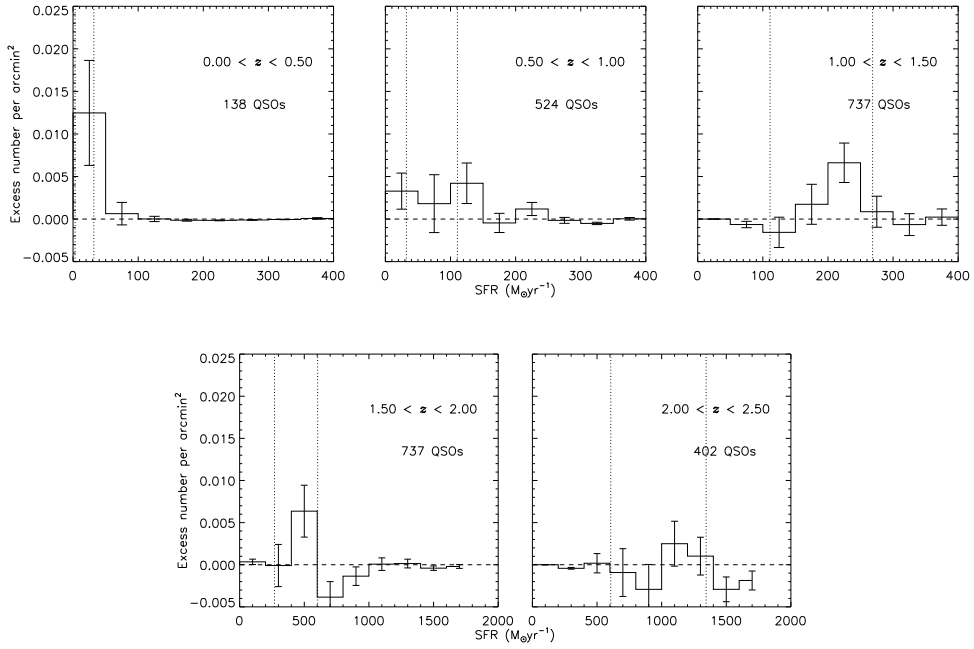

Figure 4.6: Over-density of galaxies around the QSOs in the sample with $z < 2.5$ split into five course redshift ranges of width 0.5 binned by their SFR in 50 $M_{\odot}yr^{-1}$ bins, except for the two highest z bins where the bins are of width 200 $M_{\odot}yr^{-1}$. These were created by subtracting the number counts for the local backgrounds from environments counts both corrected for flux boosting and incompleteness using the corrections from Rigby et al. (2011). Error bars are Poisson, generated by adding in quadrature the error bars on the environment and background number counts. The vertical dotted lines represents the SFR that the H-ATLAS catalogues flux limit is equivalent to at the redshift extremes of the bin, hence where incompleteness is an issue. Details of the conversion between flux and SFR are given in the text. Note that the SFR scale is different on the two highest z bins.

are found in which in the un-subtracted histograms have sources in but the background subtraction removes them. This suggests these objects are part of the background, hence their SFRs are not correct as they are found in equal numbers in both the QSOs vicinities and the background annuli. There are also no over-densities of sources with non-sensibly large SFRs. This is despite these again existing in the un-subtracted histograms as might be expected when foreground sources SFRs are calculated using the QSOs' redshifts, again evidence that the background removal is working.

At face value it therefore appears that the SFR of the excess galaxies is declining with decreasing redshift. However the plague of flux limited samples of QSOs is the degeneracy between QSO luminosity and redshift, which can be seen in Fig. 4.2. The increasing volume contained in the survey at higher redshift means that rarer more luminous QSOs and hence those with likely more massive black holes are sampled. Conversely at low redshift the shorter luminosity distance means less luminous QSOs are detectable than can be at higher z. Practically, QSO samples at different redshifts are made up of QSOs which may vary by orders of magnitude in their luminosity, hence black hole masses. It is not possible therefore, to be sure if the decline in SFR rate that is seen is due to looking around QSOs of different luminosities/black hole masses or an actual decrease in the SFR in the QSOs' environments with cosmic time.

4.4.6 SFR versus z for Luminosity Matched Sub-Sample

To address this degeneracy two sub-samples are created with a matched luminosity range but split into two redshift epochs; these are shown in Fig. 4.7. The sub-samples span a luminosity range of -23.5 to -25.5 (absolute magnitudes) in QSO luminosity and the two redshift epochs are $0.8 < z < 1.3$ and $1.3 < z < 1.8$. The reason for choosing the location of these two samples is that the choice is limited by two factors. At lower redshift sufficient numbers of QSOs are lacking to make a statistical detection of their low density environments and at higher redshift the flux limit of H-ATLAS means the survey is only sensitive to galaxies with very high SFRs (see Fig. 4.1). The width of the samples is therefore a trade off between needing to match the luminosity range and distribution but also needing a sufficient number of QSOs in each epoch. The distributions of QSO luminosities in both epochs are consistent with being drawn from the same parent distribution when analysed with a two sample Kolmogorov-Smirnov test. The means are -24.46 and -24.49 (absolute magnitudes) for the lower and higher redshift epochs respectively for which a Mann-Whitney test will not allow the null-hypothesis that they are the same to be rejected.

The result of searching for over-densities in these matched sub-samples are shown in Fig. 4.8 which shows the same result as in Fig. 4.6 of a decreasing SFR with decreasing redshift. The lower redshift epoch ($0.8 < z < 1.3$) has bins with 1.3 and a 0.7 σ level over-densities for galaxies with $100 <$ SFR < 300 $M_{\odot}yr^{-1}$. The higher redshift epoch ($1.3 < z < 1.8$) in contrast has an over-density at the 2.6 σ level for galaxies with $400 <$ SFR < 500 $M_{\odot}yr^{-1}$.

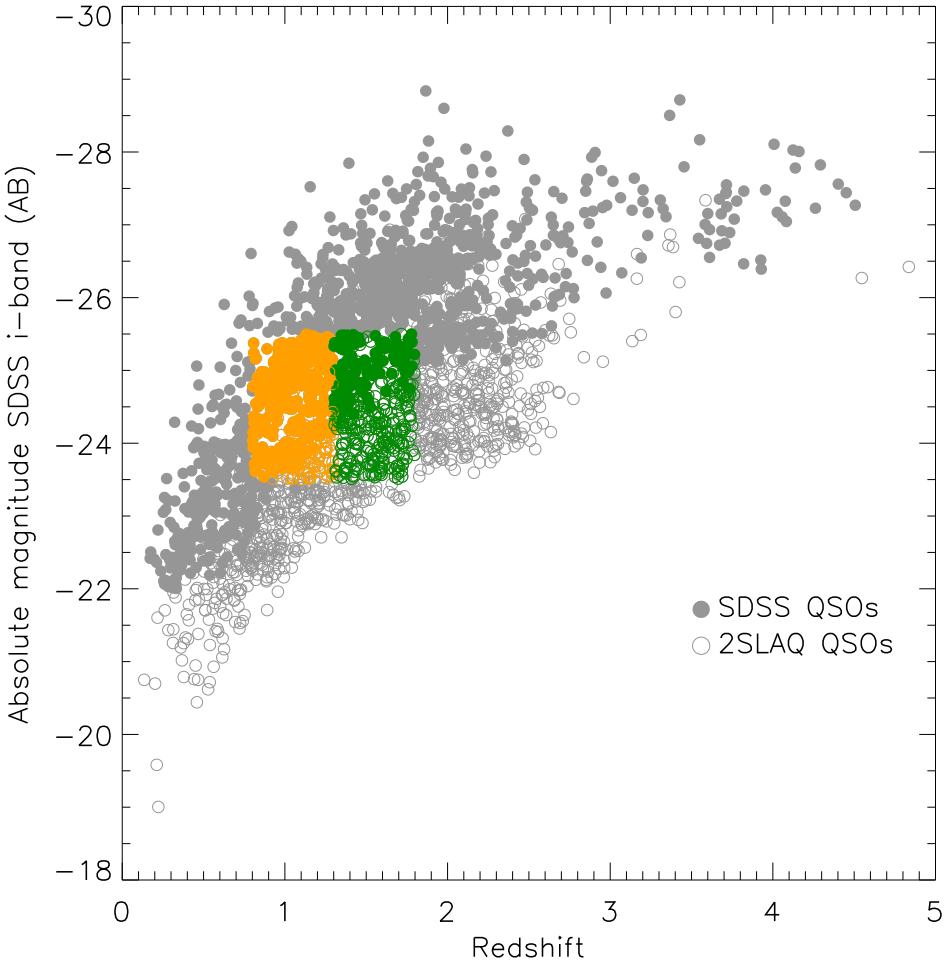

Figure 4.7: Redshift versus optical absolute magnitude (SDSS i-band) for the QSOs in the sample. SDSS QSOs are shown with filled symbols and 2SLAQ QSOs are shown with open symbols. Over-plotted in colour is the matched luminosity sub-sample split into two redshift epochs shown in orange and green ($0.8 < z < 1.3$ and $1.3 < z < 1.8$ respectively).

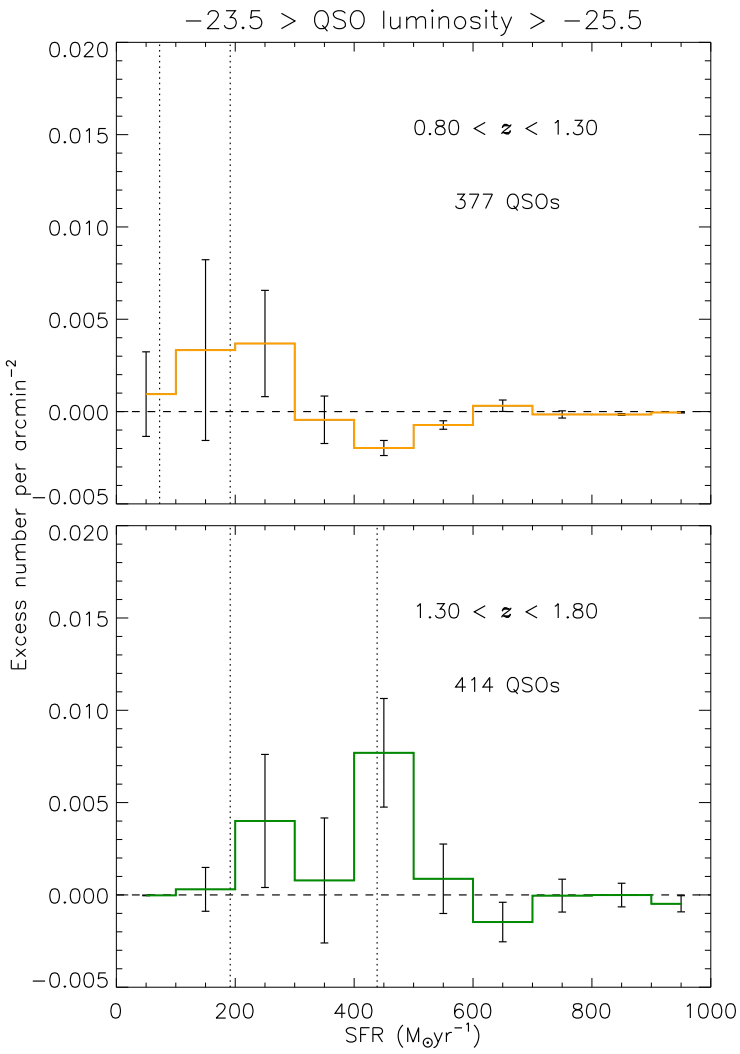

Figure 4.8: Over-density of galaxies around the QSOs in each epoch of the luminosity matched sub-sample. The detected galaxies are binned by their SFR in 100 $M_\odot yr^{-1}$ bins created by subtracting the number counts for the environments from the counts for the local backgrounds, both corrected for flux boosting and completeness using the correction from Rigby et al. (2011). Error bars are Poisson, generated by adding in quadrature the error bars on the environment and background histograms. The vertical dotted lines shows for each panel the maximum and minimum SFR that the H-ATLAS flux limit of the catalogue corresponds to (*i.e.* the SFR that the flux limit corresponds to at the redshift extremes of the bin). Colours of the samples are the same as in Fig. 4.7.

Table 4.2: Table showing the over-density of FIR galaxies around QSOs from the QSO property sub-samples. Columns show the name of the sub-sample, the number of QSOs, mean redshift of sub-sample, the excess number of galaxies per arcmin^2 as well as the excess number of galaxies per field and the Poisson significance of this excess. See text for definitions of each sub-sample. All numbers quoted have the corrections applied for flux boosting and incompleteness from Rigby et al. (2011).

Sub-sample	QSOs	$< z >$	Over-density (N/arcmin)	Over-density N	σ
All QSOs ($z < 1.5$)	1399	0.98	0.010 ± 0.003	0.17 ± 0.05	3.2
Radio-loud ($z < 1.5$)	78	1.01	0.014 ± 0.013	0.23 ± 0.22	1.0
FIR detected ($z < 1.5$)	75	0.93	0.006 ± 0.023	0.12 ± 0.13	0.5

Galaxies with the SFRs seen around QSOs in the higher redshift epoch are not seen at all around the QSOs in the lower redshift epoch and the difference between the $400 <$ SFR < 500 $M_{\odot}yr^{-1}$ bins is significant at the 3.2 σ level. As in Fig. 4.6 it is not possible to detect the over-density detected in the lower redshift epoch at higher redshift due to the flux limit affecting progressively higher SFRs as redshift increases (shown by the vertical dotted lines).

4.4.7 Excess versus QSOs' Properties

In this Section the H-ATLAS data are examined to determine whether any link can be found between those QSOs which have excess galaxies around them and the QSOs' properties. To do this, over-densities around sub-samples of QSOs with different properties were compared to the level of over-density around the sample as a whole.

Since many authors have found differences between radio-loud and radio-quiet QSO environments (e.g. Yee & Green 1984; Yee & Green 1987; Kauffmann et al. 2008; Falder et al. 2010) a radio-loud sample was created with

the QSOs that are detected by the FIRST radio survey at 1.4 GHz (Becker et al., 1995) with a signal to noise > 5. Additionally a sub-sample is created of QSOs that are detected by *Herschel* as many of the AGN environments studied with SCUBA were selected because they were already known to be submillemeter sources themselves (e.g Priddey et al. 2008; Stevens et al. 2010). This addresses the question of whether this requirement created a bias in their selection which preferentially meant over-densities of extreme star-forming galaxies were always found. In the phase 1 QSO sample only around 10 per cent of the QSOs are found to have likely counterparts in the H-ATLAS catalogue using the cross ID catalogue of Smith et al. (2011), this agrees with the numbers found in the H-ATLAS SDP data (Bonfield et al., 2011).

The results of looking for over-densities around each of these sub-samples is shown in Table 4.2. This analysis shows that the small numbers of radio-loud and FIR detected QSOs compared to the sample as a whole mean it is not possible to say anything other than they are fully consistent with being drawn from the sample as a whole. It is possible, however, to rule out most/all of the excess galaxies being found around either the radio-loud or FIR detected QSOs. Again the full H-ATLAS survey may allow something more to be said about the results of this analysis.

4.4.8 Flux from Maps Results

This Section describes the second approach that was used to try and include sources below the 5 σ limit that the catalogues are cut at. This involved

extracting the flux directly from the maps within the 1 Mpc region that the catalogue was searched in. The principle is that this will include flux from not only the catalogued sources but also any $< 5\ \sigma$ sources in the aperture and any excess caused by an unresolved blended population of sources. The background subtraction works in the same way as for the catalogue by subtracting the flux extracted in an aperture with an angular size of 2-4 Mpc at the QSOs' redshifts.

This approach is found to be greatly hampered by the presence of the large scale galactic cirrus emission that contaminates the H-ATLAS maps. The source extraction procedure used to make the H-ATLAS catalogue deals with the cirrus emission by first subtracting a background from the maps. This background consists of the peak of a histogram (mode) of pixel values in a 30×30 pixel box. The idea being that the cirrus is the dominant contribution to the flux in the maps on this scale. The background subtraction is then smoothed between each 30×30 pixel box so that each pixel in the map will have a slightly different value subtracted. This principle works fine for finding 5σ point sources because their flux by definition will be much higher than the background value and they are also very small compared to the 30×30 pixel box and so will not dominate the pixel histogram.

However as the maps start to become significantly confused below the $5\ \sigma$ flux levels the contribution to the pixel histogram of lower S/N sources will be more important. Indeed, for completely unresolved sources that would just add a large scale flux excess around the QSOs this will become indistinguishable from the cirrus emission as the scales involved are identical. At $z \sim 1$ for example, 30 H-ATLAS pixels corresponds to 150 $''$ which is

1.2 Mpc so any Mpc scale population of sources in the QSOs' environments that are unresolved is likely to be removed by the H-ATLAS background subtraction. Another issue is that the local background will have had a different background subtraction thus making it no longer appropriate, indeed no significant excess flux is found in the maps using this method.

An alternative approach would be to use the raw non-background subtracted H-ATLAS maps. However, then the problem becomes how is the cirrus separated from any large scale flux excess that is present due to sources in the QSOs environments? When conducting this method on a large number of random positions in the H-ATLAS maps it is found that it is not possible to get the results consistent with zero flux excess between the background and environment apertures; until this is possible the method cannot be attempted on the QSOs environments as it will be impossible to know if any excess is down to cirrus or the environments. It is for this reason that this approach is abandoned and the results already discussed of using the 5 σ sources in H-ATLAS catalogue are focused on.

4.5 Discussion

Overall it is found that in the environments of the QSOs in the phase 1 H-ATLAS regions there is not a large number of galaxies with high SFRs. This is in contrast to the work carried with instruments such as SCUBA at higher redshift where those QSOs studied were nearly all found to harbour galaxies with extreme star formation (SMGs) in their environments. This could be explained by the suggestion made in Stevens et al. (2003) that the

over-densities of SMGs were proto-clusters made up of galaxies that would go on to form massive elliptical galaxies by the present day. In this case then it might be expected that by $z = 1.5$ and certainly by $z = 0.5$ that the star formation in these galaxies would have finished leaving behind a passively evolving population.

This assumes the AGN remain active at the epochs studied in this work, alternatively it is possible that the AGN population surveyed in the SCUBA studies has itself evolved. AGN activity is thought to peak somewhere in the region of $2 < z < 3$ (e.g. Wolf 2005) and if AGN have lifetimes of the order 10^7 yrs then the AGN surveyed in this work are most likely a generation of AGN that switched on later than those targeted with SCUBA. Potentially the QSOs in the phase 1 H-ATLAS sample are hosted by less massive hosts or dark matter haloes which took longer to become active. Thus, these QSOs' environments may not be destined to become the rich clusters of galaxies that the environments of the AGN surveyed by SCUBA might form by the present day. This fits with the idea of downsizing of the AGN population as seen in X-ray surveys (Babić et al., 2007) where the more massive galaxies go through an active phase first.

At $z < 0.5$ on average one in every two QSOs is found to have a galaxy in its environment with a SFR of < 50 $M_{\odot}yr^{-1}$ (0.51 ± 0.24 galaxies per QSO). At higher z, galaxies with higher SFRs are detected but the excess number drops to one galaxy with a SFR between 50-150 $M_{\odot}yr^{-1}$ around five QSOs (0.18 ± 0.08 galaxies per QSO) between $0.5 < z < 1.0$ and one galaxy with a SFR of between 200-300 $M_{\odot}yr^{-1}$ around ten QSOs (0.09 ± 0.06 galaxies per QSO) between $1.0 < z < 1.5$. It is found by matching samples of QSOs in

terms of their optical luminosity that the same decline is seen of decreasing SFRs with decreased redshift of the excess galaxies suggesting this is not a bias due to looking at higher luminosity QSOs at higher redshift.

The flux limit of the H-ATLAS data means it is not possible to find the excess around the lower redshift QSOs that is seen around the higher redshift parts of the sample. It is not possible therefore to say whether the increase in the SFR of the excess galaxies with redshift is due to an additional population of star-forming galaxies around the higher redshift QSOs or whether it is the same number of galaxies just with reduced SFRs. This result was also reported in Stevens et al. (2010) where the SMGs found around typical QSOs with $1.7 < z < 2.8$ were found to be of lower 850 μm flux, hence SFR, than those reported around higher redshift AGN. It was suggested this could be due to the SFRs decreasing at lower redshift but this could equally have been due to more extreme AGN being studied at higher redshift.

In the same redshift range the H-ATLAS data are able to rule out the presence of the kind of over-densities reported by Stevens et al. (2010), around more typical QSOs than studied by other SCUBA work, only for galaxies with significantly warmer SEDs (~ 46 K).

Combining the results of this study with the work done with SCUBA does suggest that QSOs environments were more active in terms of star formation at higher redshift. This result is not surprising since it appears that the SFR history of the universe peaks in the range $1 \lesssim z \lesssim 3$ and declines since then (e.g. Madau et al. 1996; Lilly et al. 1996; Steidel et al. 1999; Hopkins & Beacom 2006). The decline in the SFR density of the universe between $z \sim 1.25$ and $z \sim 0.75$ is estimated to be at most a factor of three (Hopkins

& Beacom, 2006) which is sufficient to explain the decrease in SFRs that is observed around the QSOs in this chapter.

Ideally to address this question further a comparable sample of galaxies without QSOs would be studied. This requires knowledge of the types of galaxy the QSOs are hosted by which is not straight-forward due to the bright QSO dominating any observations. Several authors have looked at relatively low redshift QSOs host galaxies using high resolution images from the *Hubble* Space Telescope (e.g. Dunlop et al. 2003 and Letawe et al. 2010) but at best only a weak trend has been found between QSO luminosity and host galaxy luminosity and so defining this kind of sample is highly challenging.

4.6 Conclusions

In conclusion H-ATLAS data are used to study the environments of a large sample of QSOs and it is found that only a small number of QSOs are found to have galaxies with high SFRs in their environments. This is in contrast to the work done with SCUBA at higher redshift where almost all the AGN studied were found to have extreme star formation occurring in their vicinity.

The small excess of FIR bright galaxies on average corresponds to one excess galaxy around six/seven QSOs, although this is higher at lower redshift ($z < 0.5$) where we detect on average one excess galaxy around every two QSOs. The sample is examined to see if the excess is confined to those QSOs which are radio-loud or FIR detected themselves and this is found not to be the case as the over-densities found around these objects are consistent with being drawn from the population as a whole.

The excess galaxies' properties are studied statistically and in doing so it is found that the galaxies detected around the higher redshift QSOs have higher SFRs than those found around the lower redshift QSOs. The flux limit of the survey means it is not possible to say whether the increase in SFRs is due to additional star forming galaxies or a reduction in the SFRs of the same number of galaxies. Generally this is consistent with the reduction found in SFRs of SMGs in AGN environments with redshift reported in Stevens et al. (2010), but also the general decline in star formation in the universe since $z \sim$ 1-3.

The full H-ATLAS survey will provide approximately a factor of three more SDSS and 2SLAQ QSOs. This should allow the tentative results presented in this chapter to be made more robust as well as providing larger numbers of the rarer FIR bright and radio-loud QSOs with which to allow a better comparison with the QSOs environments in general.

Chapter 5

Summary & Conclusions

In this thesis I have presented the work that I have conducted over the last 3.5 years studying the environments of a large number of high redshift AGN, mostly type-1 QSOs but also some RGs in Chapter 2. I have looked specifically for evidence as to how the large scale environment influences AGN activity and vice versa by looking for relations between the observable properties of the AGN and their environmental density. I have aimed to extend the previous studies of AGN environments firstly to higher redshift than has been studied before, secondly to larger and more uniformly selected samples and thirdly to new wavelengths using previously unavailable data or facilities.

In Chapter 2 *Spitzer* space telescope data are utilised for one of the most uniformly selected samples of both RLQs and RQQs at high redshift. The sample was created to break the degeneracy that exists in almost all flux or volume limited AGN samples between luminosity and redshift. To do this the sample spans five magnitudes in optical QSO luminosity but at a

single cosmic epoch, $z \sim 1$. The RLQs and RQQs are selected in identical ways using their optical colours in the SDSS photometry and so are free of the biases associated with radio selection. The *Spitzer* data are deep enough not just to study the bright QSOs but also their fainter environments and thus comprise the most uniformly selected high redshift sample of these objects that it is possible to conduct an environmental study with to date. It specifically allowed me to address the question posed by the conflicting evidence in the literature about whether radio-loud AGN occupy on average denser environments than those which are radio-quiet. In addition to the type-1 AGN (QSOs) the *Spitzer* data also cover the fields of the 27 known radio-galaxies at the same cosmic epoch; this also allows unification schemes to be tested.

The $z \sim 1$ AGNs' environments were studied by counting the number of other sources found in their environments in the *Spitzer* images and subtracting a local background determined from the offset field in the *Spitzer* data. Using this method a significant (8 σ) excess was found in their environments projected as extending to at least $\sim$ 700 kpc and with a peak projected within $\sim$ 300 kpc. Interestingly, when the three component parts of the sample are split up and their environments studied separately the radio-loud AGN have more excess galaxies in their surroundings. The difference between the RLQs and the RQQs is found to be significant at the 2 σ level using a Mann-Whitney test.

The black hole mass estimates for the QSOs obtained using the SDSS spectroscopy of the MgII line (Jarvis et al. in prep) are used to show that the QSOs likely have the same underlying black hole mass distribution and so

the radio-loud objects are not systematically biased by being more massive. Taking this analysis a step further, correlation analysis is performed on the environmental densities looking for correlations with optical luminosity and black hole mass for the QSOs and with radio-luminosity for all the AGN. The black hole masses and optical luminosities of the QSOs are not found to be correlated with the environmental densities in this sample. However, a significant correlation (3 σ) is found for the radio-loud AGN with radio luminosities $\log_{10}(L_{325}/\mathrm{W\,Hz^{-1}\,sr^{-1}}) > 26$.

In addition to the number density analysis the spatial clustering amplitudes (B_{gq}) of the AGN are calculated using the K-band luminosity function of Cirasuolo et al. (2010). The mean B_{gq} values for each of the samples are calculated and these compare favourably with values in the literature. This allows the richness of the environments to be compared with measures such as Abell class. It is thus found that the RQQs in the sample occupy, on average, environments comparable to Abell class 0 whereas the Radio-loud AGN occupy on average environments comparable to Abell classes 0/1.

In conclusion, from this work it appears that there is a link between the radio-luminosity and the environments AGN are found in. In these data it appears this effect is seen most strongly at high radio luminosities ($\log_{10}(L_{325}$ $/\mathrm{W\,Hz^{-1}\ sr^{-1}}) > 26$) and when looking back over the literature this may be able to explain many of the conflicting results. As if RQQs are compared with high radio luminosity AGN then you may notice a difference in their environments (e.g. Yee & Green 1984, 1987; Kauffmann et al. 2008; Chapter 2) , whereas if they are compared to radio-loud AGN that have lower radio luminosity the environments may appear more consistent (e.g. Fisher

et al. 1996; McLure & Dunlop 2001b; Wold et al. 2001).

The possible physical interpretations of this link between the environment and radio luminosity that are discussed are as follows. Firstly, jet confinement (Barthel & Arnaud, 1996) which is a process where radio-jets in denser environments would produce more radiation for a given jet power; this may also explain why only the highest radio power AGN seem to exhibit the link as jet confinement may only kick in above a given jet power. Secondly the idea that it is possible that the environments are linked by a third parameter such as the spin of the central SMBH is discussed. There are several theoretical references in the literature to the spin being higher in denser environments due the black hole having more recently been spun up by a merger (e.g. Wilson & Colbert 1995; Moderski et al. 1998; Volonteri et al. 2007; Sikora et al. 2007).

In Chapter 3 deep *Spitzer* data from the SERVS survey are used to look at SDSS type-1 QSO environments at $1.3 < z < 4.0$ using a similar number density analysis to that used in Chapter 2. Working with data from a field survey means the number of QSOs, being rare, is small and so only 29 SDSS QSOs are studied with the SERVS data. Smaller numbers require a more sensitive technique to study their low density environments. Conveniently, however, the wavelengths of the SERVS survey (3.6 and 4.5 μm) provide a useful colour with which to select galaxies likely to be at $z > 1.3$. This technique used in combination with a cut of sources detected in shallower r-band data from the *Issac Newton* Telescope allow a significant (4 σ) excess to be found around the QSOs.

The results of this analysis are then compared with expectations from

the Durham semi-analytic model of galaxy formation (GALFORM) which is based on the *Millennium* dark matter simulation. The results are matched to the galaxies in the semi-analytic model by looking for black holes as massive as those required to power the QSOs in the sample and studying their environments at the appropriate epoch in the simulation. The results of this exercise are that the predictions from the model broadly agree with the numbers of excess galaxies found in the *Spitzer* data. Suggesting the models are producing the right kind of environments for black hole masses of the mass needed to host the QSOs in the sample. In addition the environments are also compared to the environments of the AGN studied in Chapter 2. The number of galaxies in the environments seems to be slightly higher around the higher redshift SERVS QSOs than around the AGN in Chapter 2 possibly suggesting some evolution in the environments hosting AGN. However, the small sample size in the SERVS analysis means it is difficult to conclude much from this data alone.

In Chapter 4, data from the recently launched *Herschel* Space Telescope are used to look at the environments of type-1 QSOs in the FIR. These QSOs are selected from both the SDSS and the lower luminosity 2SLAQ QSO surveys where they over lap the phase 1 data release of the *Herschel*-ATLAS survey. The environments are studied in two ways firstly using the 5 σ source catalogues to look for over-densities as in the previous two chapters and secondly to try and include fainter sources by looking for an excess of flux in the maps themselves.

It is found that the galactic cirrus dust that contaminates the H-ATLAS maps is very hard to distinguish from any large scale flux excesses on the

scales that the QSOs environments are likely to cover. Additionally in the background subtracted maps the H-ATLAS background removal is also likely to essentially remove any large scale flux excesses for the same reason. Concentrating, however, on the 5σ source catalogues, a small excess of galaxies is found surrounding the QSOs. This corresponds to approximately one galaxy around every two QSOs for the $z < 0.5$ and more like one galaxy around every seven to ten QSOs in the higher redshift parts of the sample.

The SFRs of the excess galaxies are examined at by using the statistical flux excess and modelling the FIR part of the spectrum with a modified black-body SED. This analysis provides the interesting result that the SFRs of the galaxies detected around the QSOs increase with redshift. This is shown not just to be the result of sampling higher luminosity QSOs at higher redshift and so appears to be a real decline in SFRs towards the present day. This effect is fully accounted for by the general decline in SFRs seen in the Universe since $z \sim 2$ (Hopkins & Beacom, 2006).

The main conclusions of this chapter are that the number of extreme star-forming galaxies that were detected by SCUBA at higher redshift are not observed around these QSOs in the H-ATLAS data. Also an excess similar to that found by Stevens et al. (2010) is also ruled out as being typical for QSOs at $1.8 < z < 2.8$ if the SEDs of these galaxies are ~ 46 K or warmer.

5.1 Future Work

The obvious future work for Chapter 2 is to firstly increase the sample sizes to make the result more robust. Secondly this work could be extended to

higher or lower redshift to see if the link between environment and radio luminosity evolves over cosmic time, as discussed below this might be possible with the full SERVS survey. This analysis could also be extended to other wavelengths such as the FIR using instruments such as SCUBA-2 and SPIRE on *Herschel*. In fact the $z \sim 1$ AGN sample has already been observed by *Herschel* and these data are currently being reduced and so a study of the FIR environments to see if the RLQs and RQQs also have differing amounts of star-formation in their surroundings is a natural extension of this chapter.

The ideal next step for the work carried out in Chapter 3 would be to extend this study to the now completed full SERVS data set. This would require using the multiwavelength data to identify additional QSOs in the data as the SDSS only overlaps with the early science data from SERVS which are the data used in Chapter 3. This would allow firmer constraints to be placed on the comparison with the predictions of the semi-analytic models. It may also be possible, if a sufficient number of RLQs could be identified, to use the SERVS data to extend the work in Chapter 2 to higher redshift. This may be possible as the early science region only contained 2 RLQs but the full survey is ~ 3 times bigger. A sample of ~ 10 RLQs may be sufficient to compare their environment to the RQQs.

Chapter 4 would benefit firstly from using the full H-ATLAS survey which should soon be available. This would give at least a factor of three increase in the numbers of QSOs in the samples including a larger number of RLQs with which to compare to RQQs. As mentioned above the *Herschel* data of the $z \sim 1$ AGN Sample will also be available soon and allow this work to be extended to a more uniformly selected QSO sample. The long awaited

commissioning of SCUBA-2 on the JCMT also provides an opportunity to extend the studies of QSO FIR environments conducted with SCUBA to more typical lower redshift QSOs and look for firmer evidence as to whether the significant over-densities found around extreme high redshift QSOs are indeed common around all QSOs and at which epochs. Data for this project have recently been taken (PI Stevens).

Bibliography

Abell, G. O. 1958, ApJS, 3, 211

Adams, M. T., Jensen, E. B., & Stocke, J. T. 1980, AJ, 85, 1010

Adelman-McCarthy, J. K., Agüeros, M. A., Allam, S. S., et al. 2006, ApJS, 162, 38

Angel, J. R. P. & Stockman, H. S. 1980, ARA&A, 18, 321

Antonucci, R. 1993, ARA&A, 31, 473

Baade, W. & Minkowski, R. 1954, ApJ, 119, 206

Babić, A., Miller, L., Jarvis, M. J., et al. 2007, A&A, 474, 755

Bahcall, J. N., Kirhakos, S., Saxe, D. H., & Schneider, D. P. 1997, ApJ, 479, 642

Bahcall, N. A., Dong, F., Hao, L., et al. 2003, ApJ, 599, 814

Balbus, S. A. & Hawley, J. F. 1991, ApJ, 376, 214

Balick, B. & Heckman, T. M. 1982, ARA&A, 20, 431

Barthel, P. D. 1989, ApJ, 336, 606

Barthel, P. D. & Arnaud, K. A. 1996, MNRAS, 283, L45

Becker, R. H., White, R. L., & Helfand, D. J. 1995, ApJ, 450, 559

Bertin, E. & Arnouts, S. 1996, A&AS, 117, 393

Best, P. N., Kauffmann, G., Heckman, T. M., & Ivezić, Ž. 2005, MNRAS, 362, 9

Best, P. N., Lehnert, M. D., Miley, G. K., & Röttgering, H. J. A. 2003, MNRAS, 343, 1

Best, P. N., Longair, M. S., & Rottgering, H. J. A. 1996, MNRAS, 280, L9

Blain, A. W., Smail, I., Ivison, R. J., Kneib, J.-P., & Frayer, D. T. 2002, Phys. Rep., 369, 111

Blandford, R. D. & Rees, M. J. 1978, Phys. Scr, 17, 265

Bolton, J. G., Gardner, F. F., & Mackey, M. B. 1963, Nature, 199, 682

Bolzonella, M., Miralles, J., & Pelló, R. 2000, A&A, 363, 476

Bonfield, D. G., Jarvis, M. J., Hardcastle, M. J., et al. 2011, MNRAS, 416, 13

Bower, R. G., Benson, A. J., Malbon, R., et al. 2006, MNRAS, 370, 645

Boyce, P. J., Disney, M. J., Blades, J. C., et al. 1998, MNRAS, 298, 121

Bruzual, G. & Charlot, S. 2003, MNRAS, 344, 1000

Calzetti, D., Armus, L., Bohlin, R. C., et al. 2000, ApJ, 533, 682

Cirasuolo, M., McLure, R. J., Dunlop, J. S., et al. 2010, MNRAS, 401, 1166

Clements, D. L. & Baker, A. C. 1996, A&A, 314, L5

Condon, J. J., Cotton, W. D., Greisen, E. W., et al. 1998, AJ, 115, 1693

Coppin, K., Chapin, E. L., Mortier, A. M. J., et al. 2006, MNRAS, 372, 1621

Cowie, L. L., Songaila, A., Hu, E. M., & Cohen, J. G. 1996, AJ, 112, 839

Croom, S. M., Richards, G. T., Shanks, T., et al. 2009, MNRAS, 392, 19

Croton, D. J., Springel, V., White, S. D. M., et al. 2006, MNRAS, 365, 11

Dasyra, K. M., Tacconi, L. J., Davies, R. I., et al. 2006, New A Rev., 50, 720

De Breuck, C., Bertoldi, F., Carilli, C., et al. 2004, A&A, 424, 1

De Robertis, M. M., Yee, H. K. C., & Hayhoe, K. 1998, ApJ, 496, 93

Doherty, M., Tanaka, M., De Breuck, C., et al. 2010, A&A, 509, A83+

Donoso, E., Li, C., Kauffmann, G., Best, P. N., & Heckman, T. M. 2010, MNRAS, 407, 1078

Dressel, L. L. 1981, ApJ, 245, 25

Dressler, A. & Richstone, D. O. 1988, ApJ, 324, 701

Driver, S. P., Popescu, C. C., Tuffs, R. J., et al. 2008, ApJ, 678, L101

Dunlop, J. S., McLure, R. J., Kukula, M. J., et al. 2003, MNRAS, 340, 1095

Dwek, E., Arendt, R. G., Hauser, M. G., et al. 1998, ApJ, 508, 106

Dye, S., Dunne, L., Eales, S., et al. 2010, A&A, 518, L10

Eales, S., Dunne, L., Clements, D., et al. 2010, PASP, 122, 499

Eales, S. A. 1985, MNRAS, 217, 149

Edge, D. O., Shakeshaft, J. R., McAdam, W. B., Baldwin, J. E., & Archer, S. 1959, MmRAS, 68, 37

Eisenhardt, P. R. M., Brodwin, M., Gonzalez, A. H., et al. 2008, ApJ, 684, 905

Elbaz, D., Jahnke, K., Pantin, E., Le Borgne, D., & Letawe, G. 2009, A&A, 507, 1359

Ellingson, E., Green, R. F., & Yee, H. K. C. 1991, ApJ, 378, 476

Elvis, M., Maccacaro, T., Wilson, A. S., et al. 1978, MNRAS, 183, 129

Falder, J. T., Stevens, J. A., Jarvis, M. J., et al. 2011, ApJ, 735, 123

Falder, J. T., Stevens, J. A., Jarvis, M. J., et al. 2010, MNRAS, 405, 347

Fan, X., Strauss, M. A., Schneider, D. P., et al. 2003, AJ, 125, 1649

Fanaroff, B. L. & Riley, J. M. 1974, MNRAS, 167, 31P

Fath, E. A. 1909, Lick Observatory Bulletin, 5, 71

Fazio, G. G., Hora, J. L., Allen, L. E., et al. 2004, ApJS, 154, 10

Fernandes, C. A. C., Jarvis, M. J., Rawlings, S., et al. 2011, MNRAS, 411, 1909

Ferrarese, L. & Merritt, D. 2000, ApJ, 539, L9

Fisher, K. B., Bahcall, J. N., Kirhakos, S., & Schneider, D. P. 1996, ApJ, 468, 469

Fixsen, D. J., Dwek, E., Mather, J. C., Bennett, C. L., & Shafer, R. A. 1998, ApJ, 508, 123

Galametz, A., Stern, D., Stanford, S. A., et al. 2010, A&A, 516, A101

Gebhardt, K., Bender, R., Bower, G., et al. 2000, ApJ, 539, L13

Gisler, G. R. 1978, MNRAS, 183, 633

Greenstein, J. L. & Matthews, T. A. 1963, AJ, 68, 279

Greve, T. R., Stern, D., Ivison, R. J., et al. 2007, MNRAS, 382, 48

Griffin, M. J., Abergel, A., Abreu, A., et al. 2010, A&A, 518, L3

Groth, E. J. & Peebles, P. J. E. 1977, ApJ, 217, 385

Hansen, S. M., McKay, T. A., Wechsler, R. H., et al. 2005, ApJ, 633, 122

Hardcastle, M. J., Evans, D. A., & Croston, J. H. 2007, MNRAS, 376, 1849

Hatch, N. A., De Breuck, C., Galametz, A., et al. 2011, MNRAS, 410, 1537

Hazard, C., Mackey, M. B., & Shimmins, A. J. 1963, Nature, 197, 1037

Heavens, A., Panter, B., Jimenez, R., & Dunlop, J. 2004, Nature, 428, 625

Henriques, B., Maraston, C., Monaco, P., et al. 2011, MNRAS, 415, 3571

Hill, G. J. & Rawlings, S. 2003, New Astronomy Review, 47, 373

Holland, W., MacIntosh, M., Fairley, A., et al. 2006, in Society of Photo-Optical Instrumentation Engineers (SPIE) Conference Series, Vol. 6275, Society of Photo-Optical Instrumentation Engineers (SPIE) Conference Series

Holland, W. S., Robson, E. I., Gear, W. K., et al. 1999, MNRAS, 303, 659

Hooper, E. J., Impey, C. D., & Foltz, C. B. 1997, ApJ, 480, L95

Hopkins, A. M. & Beacom, J. F. 2006, ApJ, 651, 142

Hopkins, P. F., Somerville, R. S., Hernquist, L., et al. 2006, ApJ, 652, 864

Hoyle, F. & Fowler, W. A. 1963, Nature, 197, 533

Hummel, E. 1980, A&A, 89, L1

Hutchings, J. B., Crampton, D., Morris, S. L., Durand, D., & Steinbring, E. 1999, AJ, 117, 1109

Inskip, K. J., Best, P. N., Longair, M. S., & Röttgering, H. J. A. 2005, MNRAS, 359, 1393

Ishida, C. M. 2004, PhD thesis, University of Hawai'i

Ivezić, Ž., Menou, K., Knapp, G. R., et al. 2002, AJ, 124, 2364

Ivison, R. J., Dunlop, J. S., Smail, I., et al. 2000, ApJ, 542, 27

Ivison, R. J., Greve, T. R., Dunlop, J. S., et al. 2007, MNRAS, 380, 199

Jarvis, M. J. & McLure, R. J. 2002, MNRAS, 336, L38

Jarvis, M. J. & McLure, R. J. 2006, MNRAS, 369, 182

Jarvis, M. J., Rawlings, S., Lacy, M., et al. 2001, MNRAS, 326, 1563

Kartaltepe, J. S., Sanders, D. B., Le Floc'h, E., et al. 2010, ApJ, 721, 98

Kaspi, S., Smith, P. S., Netzer, H., et al. 2000, ApJ, 533, 631

Kauffmann, G., Heckman, T. M., & Best, P. N. 2008, MNRAS, 384, 953

Kawakatu, N., Anabuki, N., Nagao, T., Umemura, M., & Nakagawa, T. 2006, ApJ, 637, 104

Kembhavi, A. K. & Narlikar, J. V. 1999, Quasars and active galactic nuclei : an introduction, ed. Kembhavi, A. K. & Narlikar, J. V.

Kennicutt, Jr., R. C. 1998, ARA&A, 36, 189

Kim, S., Stiavelli, M., Trenti, M., et al. 2009, ApJ, 695, 809

Kormendy, J. 1988, ApJ, 325, 128

Kukula, M. J., Dunlop, J. S., Hughes, D. H., & Rawlings, S. 1998, MNRAS, 297, 366

Kurk, J. D., Röttgering, H. J. A., Pentericci, L., et al. 2000, A&A, 358, L1

Lacy, M., Laurent-Muehleisen, S. A., Ridgway, S. E., Becker, R. H., & White, R. L. 2001, ApJ, 551, L17

Lacy, M., Wilson, G., Masci, F., et al. 2005, ApJS, 161, 41

Lagache, G., Puget, J.-L., & Dole, H. 2005, ARA&A, 43, 727

Laing, R. A., Riley, J. M., & Longair, M. S. 1983, MNRAS, 204, 151

Laor, A. 2001, ApJ, 553, 677

Letawe, Y., Letawe, G., & Magain, P. 2010, MNRAS, 403, 2088

Lilly, S. J., Le Fevre, O., Hammer, F., & Crampton, D. 1996, ApJ, 460, L1

Longair, M. S. & Seldner, M. 1979, MNRAS, 189, 433

Lonsdale, C. J., Smith, H. E., Rowan-Robinson, M., et al. 2003, PASP, 115, 897

Lynden-Bell, D. 1978, Phys. Scr, 17, 185

Madau, P., Ferguson, H. C., Dickinson, M. E., et al. 1996, MNRAS, 283, 1388

Magorrian, J., Tremaine, S., Richstone, D., et al. 1998, AJ, 115, 2285

Markowitz, A. & Uttley, P. 2005, ApJ, 625, L39

Matthews, T. A. & Sandage, A. R. 1963, ApJ, 138, 30

Mattson, B. J. 2008, PhD thesis, University of Maryland, College Park

McLure, R. J. & Dunlop, J. S. 2001a, MNRAS, 327, 199

McLure, R. J. & Dunlop, J. S. 2001b, MNRAS, 321, 515

McLure, R. J. & Dunlop, J. S. 2002, MNRAS, 331, 795

McLure, R. J. & Jarvis, M. J. 2002, MNRAS, 337, 109

McLure, R. J. & Jarvis, M. J. 2004, MNRAS, 353, L45

McLure, R. J., Kukula, M. J., Dunlop, J. S., et al. 1999, MNRAS, 308, 377

McMahon, R. G., Walton, N. A., Irwin, M. J., et al. 2001, New A Rev., 45, 97

Mihos, J. C. 2004, Clusters of Galaxies: Probes of Cosmological Structure and Galaxy Evolution, 277

Moderski, R., Sikora, M., & Lasota, J. 1998, MNRAS, 301, 142

Moffet, A. T. 1966, ARA&A, 4, 145

Nandra, K. & Pounds, K. A. 1994, MNRAS, 268, 405

Netzer, H. & Peterson, B. M. 1997, 218, 85

Neugebauer, G., Habing, H. J., van Duinen, R., et al. 1984, ApJ, 278, L1

Osterbrock, D. E. 1991, Reports on Progress in Physics, 54, 579

Ostriker, J. P. 1980, Comments on Astrophysics, 8, 177

Overzier, R. A., Bouwens, R. J., Cross, N. J. G., et al. 2008, ApJ, 673, 143

Overzier, R. A., Miley, G. K., Bouwens, R. J., et al. 2006, ApJ, 637, 58

Page, M. J., Stevens, J. A., Ivison, R. J., & Carrera, F. J. 2004, ApJ, 611, L85

Page, M. J., Stevens, J. A., Mittaz, J. P. D., & Carrera, F. J. 2001, Science, 294, 2516

Papovich, C. 2008, ApJ, 676, 206

Papovich, C., Momcheva, I., Willmer, C. N. A., et al. 2010, ApJ, 716, 1503

Pascale, E., Auld, R., Dariush, A., et al. 2011, MNRAS, 415, 911

Pentericci, L., Kurk, J. D., Röttgering, H. J. A., et al. 2000, A&A, 361, L25

Peterson, B. M. 1993, PASP, 105, 247

Pilbratt, G. L., Riedinger, J. R., Passvogel, T., et al. 2010, A&A, 518, L1

Poglitsch, A., Waelkens, C., Geis, N., et al. 2010, A&A, 518, L2

Polletta, M., Tajer, M., Maraschi, L., et al. 2007, ApJ, 663, 81

Priddey, R. S., Ivison, R. J., & Isaak, K. G. 2008, MNRAS, 383, 289

Rawlings, S., Eales, S., & Lacy, M. 2001, MNRAS, 322, 523

Rawlings, S. & Jarvis, M. J. 2004, MNRAS, 355, L9

Rees, M. J. 1984, ARA&A, 22, 471

Rengelink, R. B., Tang, Y., de Bruyn, A. G., et al. 1997, A&AS, 124, 259

Richards, G. T., Lacy, M., Storrie-Lombardi, L. J., et al. 2006a, ApJS, 166, 470

Richards, G. T., Strauss, M. A., Fan, X., et al. 2006b, AJ, 131, 2766

Richstone, D., Ajhar, E. A., Bender, R., et al. 1998, Nature, 395, A14

Rigby, E. E., Maddox, S. J., Dunne, L., et al. 2011, MNRAS, 415, 2336

Roberts, D. H., Odell, S. L., & Burbidge, G. R. 1977, ApJ, 216, 227

Romano-Diaz, E., Shlosman, I., Trenti, M., & Hoffman, Y. 2011, ApJ, 736, 66

Salpeter, E. E. 1964, ApJ, 140, 796

Sanders, D. B. & Mirabel, I. F. 1996, ARA&A, 34, 749

Sanders, D. B., Soifer, B. T., Elias, J. H., et al. 1988, ApJ, 325, 74

Sargent, W. L. W., Young, P. J., Lynds, C. R., et al. 1978, ApJ, 221, 731

Schade, D. J., Boyle, B. J., & Letawsky, M. 2000, MNRAS, 315, 498

Schmidt, M. 1963, Nature, 197, 1040

Schmidt, T. 1964, Zeitschrift fur Astrophysik, 60, 106

Schneider, D. P., Hall, P. B., Richards, G. T., et al. 2005, AJ, 130, 367

Schneider, D. P., Richards, G. T., Hall, P. B., et al. 2010, AJ, 139, 2360

Schweizer, F. 1980, ApJ, 237, 303

Seldner, M. & Peebles, P. J. E. 1978, ApJ, 225, 7

Serber, W., Bahcall, N., Ménard, B., & Richards, G. 2006, ApJ, 643, 68

Seyfert, C. K. 1943, ApJ, 97, 28

Sikora, M., Stawarz, Ł., & Lasota, J. 2007, ApJ, 658, 815

Smail, I., Ivison, R. J., Gilbank, D. G., et al. 2003, ApJ, 583, 551

Smith, D. J. B., Dunne, L., Maddox, S. J., et al. 2011, MNRAS, 416, 857

Smith, E. P. & Heckman, T. M. 1990, ApJ, 348, 38

Smith, H. J. & Hoffeit, D. 1965, in Quasi-Stellar Sources and Gravitational Collapse, ed. I. Robinson, A. Schild, & E. L. Schucking, 461

Smith, R. J., Boyle, B. J., & Maddox, S. J. 1995, MNRAS, 277, 270

Smith, R. J., Boyle, B. J., & Maddox, S. J. 2000, MNRAS, 313, 252

Soifer, B. T., Sanders, D. B., Madore, B. F., et al. 1987, ApJ, 320, 238

Springel, V., White, S. D. M., Jenkins, A., et al. 2005, Nature, 435, 629

Sramek, R. A. & Weedman, D. W. 1980, ApJ, 238, 435

Steidel, C. C., Adelberger, K. L., Giavalisco, M., Dickinson, M., & Pettini, M. 1999, ApJ, 519, 1

Stern, D., Holden, B., Stanford, S. A., & Spinrad, H. 2003, AJ, 125, 2759

Stevens, J. A., Ivison, R. J., Dunlop, J. S., et al. 2003, Nature, 425, 264

Stevens, J. A., Jarvis, M. J., Coppin, K. E. K., et al. 2010, MNRAS, 405, 2623

Stevens, J. A., Page, M. J., Ivison, R. J., et al. 2005, MNRAS, 360, 610

Tanaka, M., Finoguenov, A., & Ueda, Y. 2010, ApJ, 716, L152

Taylor, M. B. 2005, in Astronomical Society of the Pacific Conference Series, Vol. 347, Astronomical Data Analysis Software and Systems XIV, ed. P. Shopbell, M. Britton, & R. Ebert, 29–+

Tubbs, A. D. 1980, ApJ, 241, 969

Turner, T. J. & Pounds, K. A. 1988, MNRAS, 232, 463

Vardoulaki, E., Rawlings, S., Hill, G. J., et al. 2010, MNRAS, 401, 1709

Venemans, B. P., Röttgering, H. J. A., Miley, G. K., et al. 2007, A&A, 461, 823

Volonteri, M., Sikora, M., & Lasota, J. 2007, ApJ, 667, 704

Werner, M. W., Roellig, T. L., Low, F. J., et al. 2004, ApJS, 154, 1

White, R. L., Helfand, D. J., Becker, R. H., Glikman, E., & de Vries, W. 2007, ApJ, 654, 99

Wiita, P. J. 2004, Ap&SS, 293, 235

Willott, C. J. & et al. 1998, 226, 209

Wilson, A. S. & Colbert, E. J. M. 1995, ApJ, 438, 62

Wilson, G., Muzzin, A., Yee, H. K. C., et al. 2009, ApJ, 698, 1943

Wisotzki, L. 2000, A&A, 353, 861

Wold, M., Lacy, M., Lilje, P. B., & Serjeant, S. 2001, MNRAS, 323, 231

Wolf, C. 2005, Mem. Soc. Astron. Italiana, 76, 21

Yee, H. K. C. & Ellingson, E. 1995, ApJ, 445, 37

Yee, H. K. C. & Green, R. F. 1984, ApJ, 280, 79

Yee, H. K. C. & Green, R. F. 1987, ApJ, 319, 28

Zakamska, N. L. 2005

Zamfir, S., Sulentic, J. W., & Marziani, P. 2008, MNRAS, 387, 856

Zel'Dovich, Y. B. & Novikov, I. D. 1965, Soviet Physics Doklady, 9, 834

Appendix A

The $z \sim 1$ AGN Sample

The following tables give the main details of the $z \sim 1$ AGN sample used in Chapter 2, the AGN have *Spitzer* observations with all four IRAC channels and with MIPS at 24 μm. The tables are split into the three sub-samples radio galaxies, radio-loud QSOs and radio-quiet QSOs.

The sample was designed to address the degeneracy between luminosity and redshift that is an inherent problem in AGN samples selected from flux or volume limited surveys. The idea was to construct an AGN sample at a single cosmic epoch; $z \sim 1$ was chosen for this as it allows QSOs spanning five magnitudes of optical luminosity to be sampled. It is the lowest epoch where a large enough number of the highest luminosity QSOs can be sampled to compare with the QSOs found at the highest redshifts. In addition to the QSOs to allow unification models to be tested, type-2 AGN in the form of radio-galaxies were added.

The sample selection and new *Spitzer* observations will be described by Jarvis et al. (in prep) which will also present analysis of the QSO *Spitzer* data. Analysis of the radio galaxy data is presented by Fernandes et al. (2011).

Radio Galaxies

Table showing the main properties of the radio galaxies in the $z \sim 1$ AGN sample with observations by *Spitzer*. The majority were observed under program ID30344 PI Jarvis with the exception of 3C356 & 3C184 which were observed in programs ID3329 & ID17 under PIs Stern & Fazio respectively. The 325 MHz flux densities, which are given in the rest-frame, and spectral indices ($S_\nu \propto \nu^{-\alpha}$) are calculated by fitting a power-law through available flux density measurements. These and the redshifts come from NASA Extragalactic Database (NED) except the 6C objects which are taken from Best et al. (1996), Rawlings et al. (2001) and Inskip et al. (2005) and for the 6C* and TOOT objects which come from Jarvis et al. (2001) and Vardoulaki et al. (2010) respectively.

Name	RA Degrees	Dec Degrees	z	F_{radio} 325 MHz Jy	Spectral index
PI Jarvis					
3C175.1	108.51962	14.60628	0.92	6.938966	0.8502
3C22	12.73426	51.20096	0.936	8.348079	0.90307
3C268.1	180.09959	73.01242	0.97	15.614554	0.57748
3C280	194.24083	47.33889	0.996	16.025129	0.81323
3C289	206.36314	49.7754	0.9674	8.277617	0.84278
3C343	248.64118	62.76007	0.988	13.412746	0.67807
5C6.24	32.56994	32.82611	1.073	0.838537	0.76874
5C7.17	123.24743	26.86264	0.936	0.468831	0.93455
5C7.23	123.41103	29.27489	1.098	0.545624	0.77706

Continued on next page...

...continued from previous page.

Name	RA Degrees	Dec Degrees	z	F_{radio} 325 MHz Jy	Spectral index
5C7.242	126.42809	24.67246	0.992	0.304469	0.93992
5C7.82	124.44538	29.36398	0.918	0.37068	0.93016
6CE0943+3958	146.57792	39.73844	1.035	1.182158	0.84753
6CE1011+3632	153.55363	36.28823	1.042	1.189592	0.79145
6CE1017+3712	155.16685	36.95073	1.053	1.540403	1.00011
6CE1019+3924	155.73016	39.14704	0.9226	1.690154	0.94441
6CE1129+3710	173.14779	36.90471	1.06	1.542944	0.89198
6CE1212+3805	183.73617	37.81412	0.95	1.408779	1.06049
6CE1217+3645	185.04104	36.48533	1.088	1.402396	0.94479
6CE1256+3648	194.77495	36.53259	1.07	1.760399	0.81331
6CE1257+3633	194.87529	36.2842	1.004	1.036212	1.08333
6C*0128+394	22.87314	39.71589	0.929	1.3222	0.5
6C*0133+486	24.16927	48.87343	1.029	0.7418	1.22
TOOT1066	3.45095	34.94931	0.111	0.097527	0.87
TOOT1140	2.12841	36.36357	0.339	0.298261	0.75
TOOT1267	3.87908	36.20465	0.345	0.28163	0.8
PI Stern					

Continued on next page...

...continued from previous page.

Name	RA Degrees	Dec Degrees	z	F_{radio} 325 MHz Jy	Spectral index
3C356	261.079	50.9612	1.079	6.819501	1.04217
PI Fazio					
3C184	114.8511	70.38639	0.994	9.096968	0.86903

Radio-Loud QSOs

Table showing the main properties of the radio-loud QSOs in the $z \sim 1$ AGN sample with observations by *Spitzer*. All the QSOs were selected from the fifth data release of the SDSS quasar survey (Schneider et al. 2005); they were matched in optical colours and luminosities with the radio-quiet QSOs in the sample (shown in next table). The majority were observed under program ID30344 PI Jarvis except those for which the names are preceded by the letter 'R' these were observed as part of the SWIRE survey (Richards et al., 2006b). Mi is the extinction and k corrected absolute magnitude in the SDSS i-band, essentially the QSO optical luminosity. The black hole masses (Mbh) were estimated using the FWHM of the MgII emission line in the SDSS spectroscopy; see Jarvis et al. (in prep) for full details. The spectral indices ($S_\nu \propto \nu^{-\alpha}$) were calculated using the flux density measurements from the FIRST/NVSS and WENSS surveys at 1400 and 325 MHz; where only one flux density measurement was available the spectral index is left blank and a value of 0.7 assumed to calculate the 325 MHz flux measurement if needed.

Name	RA Degrees	Dec Degrees	z	Mi	Mbh $\log_{10} M_\odot$	F_{radio} (Jy) 325 MHz	Spectral index
PI Jarvis							
SDSS074417.47+375317.2	116.0728	37.88813	1.067	-26.078	9.57073	7.461	1.2601
SDSS074815.44+220059.5	117.0643	22.01655	1.0595	-27.851	9.40587	0.019008	
SDSS075928.29+301028.3	119.8679	30.17459	1.0021	-26.175	8.9728	0.315	0.3512
SDSS080915.88+321041.6	122.3161	32.17821	0.915	-23.671	8.14968	0.023	-0.34157
SDSS081520.66+273617.0	123.836	27.60474	0.9081	-27.13	9.19977	0.013412	
SDSS082012.62+431358.5	125.0526	43.23288	1.0732	-26.086	8.97925	0.033	0.0923

Continued on next page...

...continued from previous page.

Name	RA Degrees	Dec Degrees	z	Mi	Mbh $\log_{10} M_\odot$	F_{radio} (Jy) 325 MHz	Spectral index
SDSS082836.39+504826.5	127.1515	50.80738	0.9289	-24.559	8.68069	0.148	-0.12195
SDSS082901.27+371806.1	127.2553	37.30167	0.9342	-24.183	7.52205	0.067	0.70205
SDSS083110.01+374209.6	127.7917	37.70261	0.9187	-24.837	8.89561	6.199	0.72093
SDSS083226.07+343414.3	128.1087	34.57078	1.005	-24.428	8.74705	0.131	0.71894
SDSS083248.44+422459.5	128.2018	42.41651	1.0513	-25.344	8.5594	1.033	0.5851
SDSS083315.07+350647.3	128.3128	35.11306	1.0982	-24.86	9.00716	0.058	0.96009
SDSS083407.56+354712.0	128.5315	35.78666	1.0875	-24.057	8.09212	0.067	0.77893
SDSS084028.34+323229.4	130.118	32.54148	1.0992	-25.296	9.03254	0.065	0.75784
SDSS090037.89+550318.0	135.1578	55.05504	0.947	-24.805	8.51502	0.018	0.53137
SDSS090142.41+425631.0	135.4266	42.94193	1.0144	-24.879	9.0881	0.034	0.31037
SDSS090812.18+514700.8	137.0506	51.78359	1.0021	-25.578	9.05389	0.198	0.87465
SDSS090910.09+012135.7	137.2919	1.359871	1.0244	-26.918	9.15065	2.050339	
SDSS091011.01+463617.8	137.5459	46.60494	1.0199	-26.898	8.83508	0.273	0.38622
SDSS091921.56+504855.4	139.8397	50.81541	0.9212	-25.499	9.32222	0.142	1.09581
SDSS093332.71+414945.0	143.3862	41.82916	0.9325	-24.192	7.97558	0.079	0.71526
SDSS094644.72+414304.5	146.6864	41.71787	1.0179	-25.412	8.11096	0.117	0.56917
SDSS094740.01+515456.8	146.9162	51.91576	1.0631	-24.594	9.13829	0.498	1.43998
SDSS095227.30+504850.7	148.1135	50.81398	1.0909	-26.214	9.09116	0.107	0.24984

Continued on next page...

...continued from previous page.

Name	RA Degrees	Dec Degrees	z	Mi	Mbh $\log_{10} M_\odot$	F_{radio} (Jy) 325 MHz	Spectral index
SDSS100940.46+465525.0	152.4185	46.92358	1.0128	-24.22	8.55028	0.24	0.79345
SDSS100943.56+052953.9	152.4314	5.498342	0.9421	-26.737	9.61884	0.230495	
SDSS104542.18+525112.6	161.4257	52.85343	1.0583	-25.827	9.15144	0.884	1.12757
SDSS112023.23+540427.1	170.0966	54.07422	0.9234	-24.385	8.88268	0.66	0.63609
SDSS115120.46+543733.1	177.8352	54.62587	0.9754	-28.059	9.47883	0.010256	
SDSS120127.43+090040.6	180.3642	9.011299	1.0161	-27.228	9.76538	0.045508	
SDSS120556.09+104253.9	181.4837	10.71498	1.0884	-27.131	9.59116	1.133065	
SDSS121529.56+533555.9	183.8731	53.59887	1.0692	-25.966	9.27582	7.827	0.96331
SDSS122339.34+461118.7	185.9138	46.18862	1.0129	-26.063	8.53509	0.408	0.10021
SDSS122409.91+500155.5	186.041	50.03209	1.0658	-26.664	8.86694	0.057	0.14752
SDSS123259.81+513404.5	188.249	51.5679	0.9858	-24.402	8.67137	0.027	0.66697
SDSS125139.05+542758.1	192.9126	54.46623	1.0663	-25.361	9.13986	0.211	1.10189
SDSS131103.20+551354.4	197.7632	55.23172	0.9245	-24.655	9.32692	0.448	0.05011
SDSS132909.25+480109.7	202.2885	48.01937	0.9282	-27.102	9.70782	0.154	0.91128
SDSS133749.64+550102.2	204.4568	55.01739	1.0987	-25.995	8.81121	0.668	-0.02208
SDSS134213.27+602142.8	205.5552	60.36192	0.9645	-26.04	8.99737	5.714	0.93743
SDSS134357.62+575442.5	205.9898	57.91177	0.9328	-24.505	8.81624	0.208	0.40902
SDSS134934.65+534117.0	207.3944	53.68811	0.979	-26.18	9.29132	2.186	0.51936

Continued on next page...

...continued from previous page.

Name	RA Degrees	Dec Degrees	z	Mi	Mbh $\log_{10} M_{\odot}$	F_{radio} (Jy) 325 MHz	Spectral index
SDSS141028.21+460821.0	212.6174	46.13912	1.0161	-24.54	9.04736	0.726	0.81314
SDSS141802.79+414935.3	214.5116	41.82649	1.0423	-24.758	9.04646	0.035	0.66659
SDSS142829.93+443949.8	217.1247	44.66377	1.0498	-24.932	9.10207	0.073	0.80336
SDSS143253.73+460343.8	218.2239	46.06221	1.0766	-26.96	9.37709	0.013854	
SDSS143746.64+443258.6	219.4442	44.54964	0.9437	-25.469	8.85999	0.031	1.15546
SDSS143844.80+621154.5	219.6864	62.19846	1.0935	-25.231	9.27746	2.837	0.13246
SDSS144527.40+392117.0	221.3642	39.35471	0.9651	-23.583	8.19904	0.056	0.57179
SDSS144837.54+501448.9	222.1564	50.24688	1.0735	-24.81	7.86318	2.029	0.72774
SDSS150031.81+483646.8	225.1323	48.61306	1.0283	-27.464	9.46231	0.05	0.84893
SDSS150133.92+613733.8	225.3912	61.62598	0.9097	-23.555	7.91614	0.094	0.77674
SDSS150759.06+020053.8	226.996	2.014982	1.0828	-27.68	9.35748	0.015741	
SDSS152556.23+591659.5	231.4844	59.28323	0.9551	-25.406	9.54364	0.528	3.76223
SDSS152949.77+394509.6	232.4573	39.75269	1.0812	-24.863	8.2447	0.47	0.81653
SDSS154515.89+432953.1	236.3162	43.49811	0.9034	-25.762	9.32433	0.022	0.22395
SDSS155404.96+461107.5	238.5209	46.18548	1.0039	-23.589	8.57772	0.097	0.86341
SDSS155416.50+513218.9	238.5689	51.53855	0.9068	-25.54	9.02305	0.038	0.54786
SDSS155729.94+330446.9	239.3747	33.0797	0.9535	-25.321	8.61855	0.339	0.59499
SDSS160516.07+313620.8	241.3169	31.6058	1.0282	-24.907	8.73714	0.195	0.86587

Continued on next page...

...continued from previous page.

Name	RA Degrees	Dec Degrees	z	Mi	Mbh $\log_{10} M_\odot$	F_{radio} (Jy) 325 MHz	Spectral index
SDSS161603.76+463225.3	244.0157	46.54036	0.9501	-24.229	8.41117	0.069	-0.07492
SDSS161806.32+422532.1	244.5264	42.4256	0.9342	-25.608	8.15642	0.044	0.08652
SDSS162553.31+434713.8	246.4721	43.78719	1.0481	-25.462	8.17861	0.059	-0.51088
SDSS162917.79+443452.4	247.3241	44.58123	1.0331	-25.102	8.85301	0.123	1.08634
SDSS163302.10+392427.4	248.2587	39.4076	1.0238	-27.139	9.25399	0.193	0.65069
SDSS163402.95+390000.6	248.5125	39.00018	1.085	-25.686	8.39107	2.027	0.61139
SDSS163624.98+361458.0	249.1042	36.2494	0.9086	-24.569	8.45272	0.02	-0.05051
SDSS164054.17+314329.9	250.2257	31.72496	0.958	-23.688	8.95252	0.125	0.77219
SDSS165919.97+374332.7	254.8333	37.72575	1.0249	-24.649	8.47918	0.106	0.95397
SDSS165943.08+375422.7	254.9295	37.90631	1.0383	-24.688	8.94432	0.11	1.15003
SDSS170648.07+321422.9	256.7002	32.23971	1.0701	-27.682	9.58896	0.434	1.05461
SDSS170949.24+303259.2	257.4552	30.54981	1.0433	-24.811	8.41839	0.072	0.82633
SDSS172955.84+530955.9	262.4826	53.16554	1.0522	-23.91	8.32864	0.476	0.99416
SWIRE							
RSDSS104156.51+593611.2	160.4855	59.60312	1.1004	-24.275	8.26455	0.005998	
RSDSS160913.18+535429.6	242.3049	53.90822	0.9923	-25.735	9.29938	0.122432	

Radio-Quiet QSOs

Table showing the main properties of the radio-quiet QSOs in the $z \sim 1$ AGN sample with observations by *Spitzer*. All the QSOs were selected from the fifth data release of the SDSS quasar survey (Schneider et al. 2005); they were matched in optical colours and luminosities with the radio-loud QSOs in the sample (shown in previous table). The majority were observed under program ID30344 PI Jarvis except those for which the names are preceded by the letter 'R' these were observed as part of the *Spitzer* XFLS or SWIRE surveys (Richards et al., 2006b). Mi is the extinction and k corrected absolute magnitude in the SDSS i-band, essentially the QSO optical luminosity. The black hole masses (Mbh) were estimated using the FWHM of the MgII emission line in the SDSS spectroscopy; see Jarvis et al. (in prep) for full details. The upper limits on the radio flux of these QSOs where shown comes from the FIRST survey at 1400 MHz and this is described in Chapter 2; the limits are then adjusted using a spectral index of 0.7 to covert to rest-frame 325 MHz flux.

Name	RA Degrees	Dec Degrees	z	Mi	Mbh $\log_{10} M_{\odot}$	F_{radio} (Jy) 325 MHz
PI Jarvis						
SDSS003146.07+134629.6	7.941963	13.775	1.0072	-24.223	8.38223	
SDSS023540.90+001038.9	38.92043	0.1775476	0.9484	-23.655	8.2689	<0.00141
SDSS073802.37+383116.3	114.5098	38.52125	1.0225	-26.918	8.92447	<0.00179
SDSS074729.24+434607.5	116.8715	43.76884	1.086	-24.226	7.9067	<0.00140
SDSS075058.21+421617.0	117.7425	42.27137	0.9377	-23.782	8.39321	<0.00169
SDSS075222.91+273823.2	118.0954	27.63973	1.057	-27.07	9.34038	<0.00145

Continued on next page...

...continued from previous page.

Name	RA Degrees	Dec Degrees	z	Mi	Mbh $\log_{10} M_{\odot}$	F_{radio} (Jy) 325 MHz
SDSS075339.84+250137.9	118.4159	25.02716	0.943	-24.334	9.5567	<0.00219
SDSS082229.78+442705.2	125.624	44.45146	1.0566	-26.701	9.24945	<0.00183
SDSS083115.89+423316.6	127.8161	42.55459	0.9309	-25.584	9.04253	<0.00161
SDSS084723.67+011010.4	131.8485	1.16952	1.0813	-25.565	9.31234	<0.00213
SDSS090153.42+065915.6	135.4726	6.987588	1.0816	-27.029	9.37841	<0.00197
SDSS091216.88+420314.2	138.0703	42.05397	1.0771	-23.898	8.16692	<0.00202
SDSS092257.86+444651.8	140.7411	44.78113	1.0768	-25.939	8.35085	<0.00223
SDSS092753.52+053637.0	141.973	5.610232	1.062	-25.975	9.31442	<0.00212
SDSS092829.86+504836.6	142.1241	50.81009	1.0343	-25.249	9.0405	<0.00223
SDSS093023.28+403111.0	142.597	40.51974	1.0968	-25.511	8.91971	<0.00237
SDSS093303.50+460440.2	143.2645	46.07771	1.0898	-25.987	9.07278	<0.00178
SDSS093759.44+542427.3	144.4973	54.40756	1.0667	-24.041	8.18113	<0.00239
SDSS094811.89+551726.5	147.0494	55.29068	1.0338	-23.941	8.58182	<0.00206
SDSS100730.47+050942.3	151.877	5.161672	0.9204	-23.735	7.23002	<0.00211
SDSS100835.81+513927.8	152.1493	51.65774	1.0848	-25.575	8.77481	<0.00166
SDSS100906.35+023555.3	152.2764	2.598715	1.0999	-27.101	9.08246	<0.00174
SDSS102005.99+033308.5	155.0249	3.552328	0.9358	-27.004	9.43118	<0.00197
SDSS102111.57+611415.0	155.2982	61.23755	0.9314	-23.481	8.13558	<0.00223

Continued on next page...

...continued from previous page.

Name	RA Degrees	Dec Degrees	z	Mi	Mbh $\log_{10} M_{\odot}$	F_{radio} (Jy) 325 MHz
SDSS102349.40+522151.2	155.9558	52.36423	0.9553	-26.695	9.06985	<0.00145
SDSS103347.32+094039.0	158.4471	9.67751	1.0283	-26.926	9.4037	<0.00210
SDSS104537.69+484914.6	161.407	48.82071	0.9425	-23.678	8.53993	<0.00177
SDSS104935.76+554950.6	162.399	55.83069	1.0558	-25.796	9.38506	<0.00194
SDSS105408.88+042650.4	163.537	4.44733	1.0849	-26.728	9.14748	<0.00164
SDSS112317.52+051804.0	170.8229	5.301087	1.0004	-26.928	9.2501	<0.00241
SDSS114700.39+620008.1	176.7515	62.00226	1.0409	-26.839	8.97284	<0.00288
SDSS115027.25+665848.0	177.6134	66.98003	1.0352	-27.1	9.39524	
SDSS122832.94+603735.1	187.1372	60.62642	1.0397	-23.614	8.62927	<0.00216
SDSS123059.71+101624.8	187.7488	10.27347	1.0562	-25.17	9.32481	<0.00190
SDSS125659.93+042734.4	194.2496	4.459618	1.0253	-27.786	9.54244	<0.00236
SDSS132957.15+540505.9	202.4881	54.085	0.9489	-26.938	9.39026	<0.00241
SDSS133713.06+610749.0	204.3042	61.13029	0.9261	-23.667	8.79223	<0.00200
SDSS133733.30+590622.6	204.3887	59.10634	1.0872	-27.027	9.35627	<0.00192
SDSS134635.02+415630.9	206.6459	41.94194	0.9023	-24.603	8.87356	<0.00769
SDSS135823.99+021343.8	209.5999	2.228885	0.9568	-27.918	9.456	<0.00203
SDSS142124.65+423003.2	215.3528	42.50087	1.0005	-25.863	8.20377	<0.00190
SDSS142817.30+502712.6	217.0721	50.45354	1.0127	-26.67	9.223	<0.00251

Continued on next page...

...continued from previous page.

Name	RA Degrees	Dec Degrees	z	Mi	Mbh $\log_{10} M_{\odot}$	F_{radio} (Jy) 325 MHz
SDSS145503.47+014209.0	223.7644	1.702548	1.0526	-24.11	7.74723	<0.00160
SDSS145506.12+562935.6	223.7754	56.49323	1.0385	-26.643	9.2197	<0.00193
SDSS151520.56+004739.3	228.8356	0.7942888	0.951	-25.179	8.67616	<0.00190
SDSS151921.85+535842.3	229.841	53.97838	1.0265	-23.588	8.03651	<0.00190
SDSS155436.25+320408.4	238.651	32.06903	1.0576	-26.75	9.14317	<0.00195
SDSS155650.41+394542.8	239.21	39.76189	0.9415	-25.721	9.15321	<0.00237
SDSS163408.64+331242.1	248.536	33.2117	1.007	-25.268	9.13377	<0.00194
SDSS164617.17+364509.4	251.5715	36.75267	0.9577	-23.432	8.11361	<0.00184
SDSS165231.30+353615.9	253.1304	35.60441	0.9282	-24.404	8.46524	<0.00222
SDSS171005.53+644843.0	257.523	64.81193	1.0079	-25.932	9.13416	
SDSS171330.21+644253.0	258.376	64.71472	1.0506	-26.132	9.00429	
SDSS171704.69+281400.6	259.2695	28.23352	1.0781	-27.819	9.38997	<0.00179
SDSS215541.74+122818.8	328.9239	12.47193	1.0642	-26.829	9.1212	
SDSS224159.43+142055.2	340.4976	14.34861	0.9539	-25.51	8.57035	
SWIRE						
RSDSS103525.05+580335.6	158.8544	58.05989	0.9643	-24.588	8.43276	<0.00433
RSDSS103829.74+585204.1	159.6239	58.8678	0.9348	-23.955	8.40237	<0.00216
RSDSS103855.33+575814.7	159.7305	57.97075	0.9562	-25.067	8.90161	<0.00241

Continued on next page...

...continued from previous page.

Name	RA Degrees	Dec Degrees	z	Mi	Mbh $\log_{10} M_{\odot}$	F_{radio} (Jy) 325 MHz
RSDSS104114.18+590219.4	160.3091	59.03874	1.0935	-24.784	8.49269	<0.00197
RSDSS104239.66+583231.0	160.6652	58.54195	0.9983	-24.655	8.22815	<0.00187
RSDSS104355.47+593054.0	160.9811	59.51501	0.9087	-23.095	8.11513	<0.00169
RSDSS104659.37+573055.6	161.7474	57.51551	1.0264	-24.902	8.938	<0.00202
RSDSS104859.67+565648.6	162.2486	56.94684	1.0139	-25.292	8.60519	<0.00197
RSDSS104930.46+592032.6	162.3769	59.34241	1.0113	-24.95	8.34042	<0.00240
RSDSS163225.56+411852.0	248.1065	41.31455	0.9088	-25.08	8.7062	<0.00191
RSDSS163306.12+401747.0	248.2755	40.29652	0.9744	-23.812	8.45597	<0.00171
RSDSS163930.82+410013.2	249.8784	41.00379	1.0516	-25.573	9.02633	<0.00207
Spitzer XFLS						
RSDSS171732.94+594747.7	259.3872	59.79653	1.0596	-25.252	8.83855	<0.00185
RSDSS172130.96+584404.1	260.379	58.73465	1.0001	-25.475	9.02995	<0.00157
RSDSS172310.35+595105.6	260.7931	59.85157	0.9899	-24.812	8.39763	<0.00178
RSDSS171145.53+601318.4	257.9397	60.22182	0.9804	-25.289	8.81978	